APPLICATION OF SURROGATE MODELING METHODS IN SIMULATION-BASED RELIABILITY AND PERFORMANCE ASSESSMENT OF CIVIL STRUCTURES

By

Omid Khandel

Bachelor of Science in Civil Engineering
Razi University
Kermanshah, Iran
2014

Master of Science in Civil Engineering
The University of Toledo
Toledo, OH
2016

Submitted to the Faculty of the
Graduate College of the
Oklahoma State University
in partial fulfillment of
the requirements for
the Degree of
DOCTOR OF PHILOSOPHY
December, 2020

APPLICATION OF SURROGATE MODELING METHODS IN SIMULATION-BASED RELIABILITY AND PERFORMANCE ASSESSMENT OF CIVIL STRUCTURES

Dissertation Approved:

Dr. Mohamed Soliman

Dissertation Adviser

Dr. Bruce W. Russell

Dr. Samir A. Ahmed

Dr. Sabit Ekin

ACKNOWLEDGEMENTS

First of all, I would like to express my sincere appreciation to my advisor Dr. Mohamed Soliman for his wonderful guidance, endless patience and continuous support throughout my Ph.D. pursuit. I am grateful to his frequent and critical, yet friendly, guidance that always kept me on track. I also greatly appreciate him for providing me with the opportunity to co-author several scientific journal publications, project final reports, and conference papers. As a result, three journal papers, two project final reports, and eight conference papers have already been published. Two journal articles are currently under review, and two are in preparation for submission. Additionally, under Dr. Soliman's fabulous mentorship and support, I was honored to receive several department-wide and campus-wide scholarships and awards.

My special gratitude is extended to Dr. Bruce Russell, Dr. Samir Ahmed, and Dr. Sabit Ekin who agreed to serve on my Ph.D. advisory committee. Their invaluable feedback, support, and kindness is greatly appreciated.

I gratefully acknowledge the support by grants from (a) the National Science Foundation (NSF) Award OAC-1835371, (b) the Office of Naval Research (ONR) Award N00014-18-1-2443 (c) the Southern Plains Transportation Center (SPTC) Awards 15.1-12 and 17.1-01A, and (d) the Transportation Consortium of South-Central States (Tran-Set) Award 17STOKS01.

I would also like to thank my former and current colleagues Christopher Waite, Leon Shen, Haider Ali, Mohammad Tamimi, Imran Sheikh, and Ethan Stringer for their assistance, encouragement and warm friendship.

I would like to thank my family and friends for their help and continues support. I thank my loving parents whose unconditional love, support and constant reassurance has made me the person that I am today. I am unable to express in words my respect and love for them. I would like to also thank my sister Neda, my brother-in-law Moussa, and my lovely nieces Ava and Nava for always being there and providing their help and supports. My gratitude is also extended to my brothers Arash and Saeed and their wonderful families. Last but not least, I want to sincerely thank my beautiful and loving wife Mahrokh, for her love, support, patience, and understanding. She always believed in me and inspired me to aim higher.

Name: OMID KHANDEL

Date of Degree: DECEMBER, 2020

Title of Study: APPLICATION OF SURROGATE MODELING METHODS IN SIMULATION-BASED RELIABILITY AND PERFORMANCE ASSESSMENT OF CIVIL STRUCTURES

Major Field: CIVIL ENGINEERING

Abstract: Structures and infrastructure systems are subjected to various deterioration processes due to environmental or mechanical stressors. Proper performance assessment approaches capable of detecting potential structural damage and quantifying the probability associated with structural failure are required to formulate optimal maintenance and retrofit plans that minimize the risk of failure and maximize the safety of structures. However, due to the presence of several sources of uncertainty that can affect the performance assessment and decision-making processes (e.g., uncertainties associated with loading conditions and performance prediction models), applying probabilistic methods, such as Monte Carlo simulation, is essential. In this context, a large number of simulations is generally required to quantify the low failure probability associated with civil structures. Executing the required number of simulations may be computationally expensive, especially if complex and/or nonlinear structural models (e.g., finite element models) are involved. The use of surrogate modeling tools such as artificial neural networks, polynomial chaos expansion, and kriging can help in reducing the computational costs associated with simulation-based probabilistic analysis. The research proposed herein aims to develop probabilistic approaches for performance assessment and damage detection of structures using advanced simulation-based techniques coupled with surrogate modeling. The proposed methodology is applied to quantify the risk of bridge failure due to flood events considering the impact of climate change. The approach was extended to establish the time-variant flood fragility surfaces for bridges under flood conditions. This approach (a) integrates deep learning neural networks into a simulation-based probabilistic approach to predict the future river streamflow necessary for assessing the flood hazard at the bridge location and (b) simulates the structural behavior of the bridge foundation under sour conditions. In addition, the proposed methodology is used to quantify the reliability of bolted and welded steel connections by integrating finite element analysis and surrogate models. Low-rank tensor approximation and polynomial chaos kriging surrogate models are adopted to perform Monte Carlo simulation and quantify the reliability of the investigated combination connection. Finally, artificial neural networks were used to develop a statistical damage detection and localization approach capable of evaluating the performance of prestressed concrete bridge girders using fiber optic sensors.

TABLE OF CONTENTS

Chapter Page

Chapter Page

LIST OF TABLES

Table Page

LIST OF FIGURES

Figure Page

Figure Page

Figure Page

CHAPTER I

INTRODUCTION, RESEARCH NOVELTY, AND OBJECTIVES

1.1. INTORDUCTION

Structures and infrastructure systems are subjected to various deterioration processes due to natural hazards (e.g., seismic events, hurricanes, and floods), aging effects (e.g., fatigue and corrosion), and manmade hazards (e.g., blast events and collisions). Failure or loss of functionality of vital infrastructure components such as highway bridges may result in severe economic, social, and environmental impacts. Therefore, it is crucial to accurately quantify the performance of these structures. This can be achieved by employing structural health monitoring (SHM) in combination with damage identification methods to evaluate the current state of the structure and quantifying the time-variant reliability of the structure under various loading conditions that may be encountered throughout the service life. Proper performance assessment often requires integrated simulation-based probabilistic methods that are capable of considering complex structural interactions. Simulation-based methods can enable comprehensive consideration of randomness and uncertainties associated with loading conditions (e.g., extreme natural hazards due to climate change), current condition state of the structure (e.g., bias due to visual inspections), and performance prediction (e.g., underestimation or overestimation due to simplified mechanical models), among others.

In this context, a review of available literature indicates that there is a knowledge gap in quantifying bridge performance under extreme loading conditions; especially those encountered during floods. Moreover, current literature lacks methodologies that can consider the effect of climate change on bridge failure risk under flood conditions. Most of the current flood fragility models are based on analytical formulations that can carry significant uncertainties. Available simulation-based approaches can be computationally expensive and may be ineffective in solving complex problems. In addition, an approach for identifying the damage in bridge girders under variable loading is needed. Finally, the lack of a comprehensive approach suitable for assessing the reliability of steel connections is apparent in the literature. the main aim of the proposed research is to address these gaps through the application of efficient simulation-based probabilistic methods. The first section of this dissertation focuses on developing a probabilistic framework for risk and fragility assessment of bridges under the effect og climate change, the second section provides a framework for performance assessment of bridge girders using fiber optic sensors, artificial neural networks, and statistical damage detection techniques, while the third section focuses on sensitivity and reliability quantification of combination bolted-welded steel connection. This dissertation discusses available literature, provides solutions, and presents results related to the identified knowledge gaps under the following chapters:

Chapter 2. Quantifying the Effect of Climate Change on the Risk of Bridge Failure Due to Floods and Flood-Induced Scour

Chapter 3. Assessment of Time-Variant Flood Fragility of Bridges Using Deep Learning Neural Networks

Chapter 4. Performance Assessment of Prestressed Concrete Bridge Girders using Fiber Optic Sensors and Artificial Neural Networks

Chapter 5. Sensitivity and Reliability Assessment of Concentric Combination Steel Connections Using Meta-Modeling Approach

Chapter 6. Conclusions and Recommendations for Future Work

1.2. RESEARCH OBJECTIVES

The main objective of this dissertation is establishing an integrated simulation-based framework for assessing the performance and reliability of structures under gradual and sudden deteriorative effects. In particular, the research aims at solving the following research problems:

- Incorporating climate change effects in risk quantification and performance assessment of bridges under flood and flood-induced scour.
- Developing an efficient approach for establishing the time-variant flood fragility surfaces using deep learning neural networks.
- Developing a non-destructive damage detection and localization framework for bridge girders using artificial neural networks and statistical damage detection.
- Quantifying the reliability of concentric combination steel connections using a computationally efficient framework that integrates experimental test results, finite element modeling, and meta-modeling simulation.

Chapter II to Chapter V of this dissertations aim to provide solutions for these objectives.

1.3. TECHNICAL CONTRIBUTIONS OF THE RESEARCH

- Developing the first probabilistic approach in literature for the assessment of time-variant risk of bridge failure due to floods and flood-induced scour considering (a) the results of downscaled global climate models to predict the future flood hazard and (b) the associated scour vulnerability under climate change. This framework considers various sources of

uncertainty associated with climate prediction, structural performance assessment, and consequences of bridge failure.

- Employing deep leaning neural networks for establishing the time-variant fragility surfaces of bridges under floods, flood-induced scour, and corrosion effects considering the future variability in climate. Due to the computational expenses related to probabilistic analysis involving finite element modelling and Monte Carlo simulation, the available flood fragility models in the literature establish fragility curves based on qualitative measures, simplified reliability formulations, or approximate methods. In contrary, the proposed fragility approach enables the use of finite element analysis in probabilistic simulations while maintaining a reasonable computational cost.
- Formulating a damage detection and localization approach for newly constructed prestressed concrete bridge girders using fiber optic sensing and artificial neural networks (ANNs). The presented approach employs ANNs to establish a relationship between the strain profiles recorded at different sensor locations across the investigated girder. The approach adds to existing literature by being capable of detecting the presence of damage at the sensor location without requiring detailed loading information; accordingly, it is suitable for long-term monitoring activities under normal traffic loads.
- Evaluating the reliability of concentric combination connections through an integrated framework. Currently, the limited existing research in this area is mainly based on empirical reliability formulations. The presented framework combines finite element and meta-modeling approaches to perform sensitivity analysis and quantify the reliability of bolted and welded connections. The framework uses the experimental data to evaluate the uncertainties associated with different parameters that may affect the load carrying capacity of the connections.

CHAPTER II

QUANTIFYING THE EFFECT OF CLIMATE CHANGE ON THE RISK OF BRIDGE FAILURE DUE TO FLOODS AND FLOOD-INDUCED SCOUR

2.1. OVERVIEW

Climate change has been recognized as a significant threat for transportation infrastructure. The change in temperature profiles and precipitation patterns, and the increase in the intensity of weather related extreme events, are among the effects attributed to climate change. Additionally, it may also alter the frequency and intensity of flood events; which increases the complexity of assessing the risk of bridge failure due to flood-related failure modes. Flood occurrence generally increases the rate of river bed erosion and may cause the formation of scour holes around bridge piers leading to an increased risk of bridge failure. Several factors, such as future precipitation, basin parameters, flow direction, and drainage area affect the streamflow of a river; accordingly, the proper prediction of the long-term future flood hazard requires detailed and computationally expensive climate and hydrologic modeling, which can be prohibitive in assessing the life-cycle risk of bridges and other transportation structures. This chapter addresses these issues by proposing a comprehensive, yet computationally efficient, probabilistic framework for quantifying the risk of bridge failure due to flood events considering climate change. Statistical modeling is employed to draw a relationship between the downscaled climate data adopted from global climate models and the streamflow at a given location. The effects of different global climate models and carbon dioxide emission scenarios on failure risk due to flood hazard are

taken into account. The results show that using traditional assessment approaches that does not properly consider climate change effects can lead to a considerable underestimation or over prediction in the predicted future risk. The approach is applied to an existing bridge in Oklahoma; however, it is equally applicable to bridges and other transportation structures located in other regions in the US. The work in this chapter is based on the published papers Khandel and Soliman (2018; 2019a; and 2019b).

2.2. BACKGROUND

Bridges are under continuous deterioration due to various mechanical and environmental stressors. Among the various extreme events which may affect the safety of bridges, hydraulic-related ones have been identified as the leading cause of bridge failure (AASHTO 2010; Briaud et al. 2013). In the United States, statistical analysis estimates that 52% of bridge failures are attributed to hydraulic causes (e.g., flood and scour) (Cook et al. 2015). Hydraulic bridge failures are related to precipitation patterns and flood events at the bridge location. In this context, the National Oceanic and Atmospheric Administration (NOAA) reports an average increase of 612% in the number of floods in the United States since the 1960s and it is expecting a future increase in this percentage (NOAA 2015).

The increase in flood frequency and intensity, which may be attributed to climate change, is expected to adversely affect the safety of our nation's bridges, along with devastating consequences to our transportation systems and the communities which they serve. As an indication on the severity of this problem, the 2015 flooding in Texas and Oklahoma led to at least five reported complete or partial bridge failures (Fechter 2015; Danner and Fuller 2015). These 2015 flood events resulted in 31 deaths and more than 2.5 billion dollars in economic losses to the region (Smith et al. 2017). Accordingly, bridge design and management approaches should be constructed with the ability to account for climate change in the quantification of future flood hazard. In this regards, several studies (e.g., Camp et al. 2013; Schweikert et al. 2015; Ha et

al. 2017; Douglas et al. 2017) highlighted the significance of climate change adaptation strategies and their economic benefits on transportation infrastructure.

Flooding can damage the bridge in several ways including overtopping, accelerated scour, debris impact, erosion of bridge approaches, and failure due to horizontal direct water pressure. Among those, scour is the most difficult deterioration mode from the management view point (Ettouney and Alampalli 2012). It can occur in any type of soil and undermines the stability of bridge foundation. Accordingly, its effects are generally global, where the failure of one footing may lead to the progressive collapse of the whole structure. Moreover, it is very difficult to detect and manage since most of its effects are hidden under water. Scour exposes the bridge foundations and reduces the buckling resistance of piles, as well as the lateral capacity of the foundations. Additionally, bridges subjected to scour become more vulnerable during floods (Hung and Yau 2014) and may also be vulnerable under other extreme events such as seismic excitations and traffic overload (Banerjee and Ganesh Prasad 2013; Ganesh Prasad and Banerjee 2013).

Over the past decades, researchers have formulated methodologies to evaluate the scour at bridges either deterministically (e.g., Govindasamy et al. 2008; Arneson et al. 2012) or probabilistically (e.g., Briaud et al. 2007; Bolduc et al. 2008), with detailed methodologies which can predict the performance of bridges deteriorated by scour under flood-induced loads (Hung and Yau 2014). Other studies focused on evaluating the effect of scour on the response of bridges under other hazards such as seismic events or traffic overload (e.g., Decò and Frangopol 2011; Wang et al. 2014b; Alipour and Shafei 2012; Yilmaz et al. 2016; Gehl and D'Ayala 2016; Zhu and Frangopol 2016a,b). Yilmaz et al. (2018) conducted a sensitivity study to identify the important parameters that govern the behavior of bridges under seismic and flood hazards. However, these studies did not focus on examining the potential influence of climate change on scour- or flood-vulnerable bridges. In an attempt to address this issue, Khelifa et al. (2013) quantified the regional failure risk of bridges under scour by considering the percentage of

increase in the 100-year floods. Given the goal of establishing regional risk levels, the failure probability of bridges was estimated based on an assumed overtopping probability that is related to the bridge condition with no detailed performance assessment. Kallias and Imam (2015) performed a parametric investigation to quantify the change in the failure probability of bridges with the change in the mean and standard deviation of the river flow.

In another effort, Dong and Frangopol (2016) presented an approach to quantify the risk of bridge failure and bridge resilience under multi-hazard exposure. Their study quantified the bridge risk under 100, 200, and 500 years flood hazard, however no future climate prediction was included. More recently, Mondoro et al. (2018) presented a multi-criteria optimization framework for bridges considering climate change. Although they have considered the effects of climate change on the floods with 100-year return period, no regional climate modeling, streamflow modeling, or scour analysis has been performed in their chapter. Dikanski et al. (2018) also considered the effects of climate change on scour depth prediction through the possible changes in the floods with 20- and 50-years return periods. However, no structural analysis, or risk quantification has been performed in their study.

Due to climate change, the uncertainties in the future projections of precipitation, regional moisture, rainfall, and river streamflow significantly increase, causing the traditional methods of design and assessment of bridges based on the 50, 100, or 200 year floods to be highly unreliable (Anderson et al. 2015). This unreliability promotes using a more dependable method for future climate prediction in order to assess the flood hazard. Using the results of global climate modeling and downscaling techniques to derive the regional-scale data can help quantifying the flood hazard considering various climate related parameters (e.g., carbon dioxide emission).

Global climate models (GCMs) are constructed using a general circulation model to simulate the atmosphere considering chemical, physical, and biological aspects of global climate system

(Sheffield et al. 2013a,b). Several GCMs exist such as FIO-ESM, MPI_ESM_LR, CCSM4, MIROC5 and BNU-ESM (Taylor et al. 2012). The global climate modeling data are in global scale and they should be converted to regional scale data in order to study climate patterns associated with a given river basin. This can be achieved through running a higher resolution GCM, using boundary conditions of surrounding global climate model, or using statistical downscaling methods. The first two methods are generally recognized as more complicated and computationally expensive in comparison to statistical downscaling methods, which can still achieve results with sufficient accuracy (Laprise 2008; Coiffier 2011). GCMs can also be constructed for different scenarios of future greenhouse gas (GHG) emission. Due to the presence of several GHG emission scenarios, different global climate modeling techniques, and downscaling methods, climate researchers recommend using several scenarios, each of which is characterized by its own future GHG emission level, global climate model, initial condition, and downscaling technique to quantify the highest and lowest critical bounds for future climate trends (Xue et al. 2014).

After obtaining the prediction of future climate trends and precipitation data, different hydrological models such as Variable Infiltration Capacity (VIC) (Liang et al. 1994), RAPID (David et al. 2016), and Riverware (Zagona et al. 2001) can be used to estimate the time-dependent river discharge and quantify the future flood hazard. This approach was implemented in McPherson (2016) to quantify the impact of climate change on the Red River basin in Oklahoma. In McPherson (2016), three GCMS, GHG emission scenarios, and downscaling techniques have been implemented leading to 27 different climate scenarios.

However, the hydrologic modeling using these tools often requires significant effort in calibration and executing the analysis, significant experience in hydrologic modelling, and specialized software that may not be available to all engineers. Accordingly, applying such approaches for bridge risk assessment considerably increases the complexity of the analysis. Accordingly, an

efficient, yet accurate approach is still needed for bridge risk assessment considering climate change, which is the main focus of this chapter.

This chapter presents a probabilistic framework for assessment of time-variant risk of bridge failure due to floods and flood-induced scour considering the future change in climate conditions. Risk assessment methodologies available in literature mainly rely on the return period assumption or assumed variations in the parameters of the streamflow distributions in an attempt to consider the effect of climate change. This chapter contributes to the state of art in bridge risk assessment by developing a performance-based risk assessment framework capable of employing the results of downscaled global climate models to predict the future flood hazard and the associated scour vulnerability. This framework considers various sources of uncertainty associated with climate prediction, structural performance assessment, and consequences of bridge failure. The framework uses downscaled GCM data to obtain future climate trends (e.g., precipitation and temperature profiles) under different climate scenarios. Statistical modeling is employed to draw a dynamic relationship between basin rainfall and the predicted future streamflow of the river, leading to the quantification of future flood hazard. The failure probability of the bridge due to flood and flood-induced scour is quantified using Monte Carlo simulation. Risk is computed by combining consequences of bridge failure including direct rebuilding cost and indirect losses arising from traffic delays due to road closure. The proposed approach is applied to a bridge located in Oklahoma; however, the proposed framework can be easily applied to bridges in other locations across the nation.

2.3. CLIMATE MODELING

The greenhouse gas emission has seen a considerable increase through the 20th century. The ozone layer depletion attributed to this increase causes noticeable change in climatic conditions including global temperature increase, sea level rise, and imbalance in precipitation patterns (Solomon 2007; Stocker et al. 2013). Over the past decade, significant research has been

conducted with a main goal of predicting future climate conditions in North and Central America (Sheffield et al. 2013a,b; Maloney et al. 2014; Hidalgo and Alfaro 2015). These studies mainly focused on constructing more precise methods for climate prediction; in particular, using the Coupled Model Intercomparison Project Phase 5 (CMIP5). CMIP5 provides a framework for coordinated climate change experiments. A main goal of the project was to provide projections of future climate change on a near timescale (up to 2035) and long term timescale (up to 2100 and beyond), and to evaluate their accuracy by comparing the projections to climate data observed in the short-term past (Taylor et al. 2012).

The Couple Model Inter-comparison Project Phase 5 (CMIP5) includes more than 50 different models that are able to project the past and future climate data. CMIP5 is the newest set of coordinated climate model experiments conducted to provide a multi-model understanding of carbon cycle and clouds, evaluate climate prediction ability on decadal scales, and to determine the reasons that similarly forced climate prediction models lead to various responses (Taylor et al. 2012). Different types of climate scenarios vary based on their atmospheric horizontal resolution and their model types. These models also take the interaction of various natural effects such as oceans, vegetation, and land surfaces into account (Sheffield et al. 2013a, b; Maloney et al. 2014). It should be noted that these models may not provide appropriate results for every location of interest. Therefore, proper analysis should be performed to choose the best models for the location of interest. This is achieved by comparing historical results of the adopted climate model to the observed data at the location of interest; which can be performed using the risk quantification framework proposed in this chapter.

Statistical downscaling is a widely used tool to convert the global scale climate data (e.g., 2 degree scale) to regional scale (e.g.,1/8 or 1/16 degree scale). Several statistical downscaling methods such as bias correction and spatial downscaling (BCSD), constructed analogues (CA), and daily bias correction constructed analogs (BCCA) are available in the literature (Maurer et al.

2008 and 2010). The BCCA model is a hybrid downscaling method which uses a quantile mapping bias correction on large scale data. This method combines the bias correction and daily downscaling which are typically used separately in other methods. Due to the hybrid performance of BCCA, it was shown to produce more accurate prediction of climate data (Maurer et al. 2010).

Variability in future GHG emission can be modeled in terms of Representative Concentration Pathways (RCPs) (Stocker et al. 2013). Different RCP values consider the change in radiative forcing of GHG from pre-industrial times to the 21st century. Radiative forcing can be described as the difference between absorbed insolation energy and the reflected radiation energy by the earth. Four RCP levels commonly used are RCP 2.6, RCP 4.5, RCP 6, and RCP 8.5, where the number represents the range of radiative forcing values in the year 2100 with respect to pre-industrial years. RCP values are presented with Watts per square meters of earth surface (W/m2) and their positive value indicates the increase in the net energy gained by earth, which may drive the global warming. Accordingly, different RCP values will lead to differences in climate prediction regardless of the adopted GCM and downscaling technique. Therefore, various scenarios of RCPs should be considered to account for the uncertainties associated with the future GHG emission (Shrestha et al. 2016a).

In addition to uncertainties associated with global climate modeling and climate scenarios, the effect of internal variability of the climate models should be also considered. The internal variability of the climate system is defined as the natural fluctuations that arises without radiative forcing of the planet (Hawkins and Sutton, 2009). The effect of internal variability of the climate models can be assessed by using various ensemble runs for each model. Generally, there are several ensemble runs for each climate model; these ensemble runs represent different initial conditions associated with each model and RCP combinations.

Global climate modeling is generally a computationally expensive task. This is performed through general circulation model, which employs Navier–Stokes equations to simulate the interaction of different energy sources (e.g., radiation and latent heat) on land, earth, and oceans. Fortunately, due to the considerable research activity in climate change over the past few decades, meta-data for several GCMs is available in literature. For instance, the refined daily precipitation and temperature data for the time period 1960 to 2100 with BCCA downscaling method are available through Downscaled CMIP3 and CMIP5 Climate and Hydrology Projections archive at Brekke et al. (2013). The BCCA climate projection covers the North American Land-Data Assimilation System which contains contiguous United States plus portions of southern Canada and northern Mexico, spanning from 25.125° N to 52.875° N and - 124.625° E to -67.000° E. These data sets are used in this chapter for quantifying the flood hazard at the bridge location.

2.4. STREAMFLOW PREDICTION

In general, three types of rainfall-runoff models can be used to draw a relationship between climate data and streamflow: metric, conceptual, and physics-based models. While metric models use the observed rainfall and streamflow data to characterize the response of a given basin, conceptual models use internal processes of the basins to describe the storage and movement of water between atmosphere, lithosphere and hydrosphere. In addition, Physics-based models use numerical simulation of equations of motion to characterize the catchment response. Conceptual and physics-based models are generally more involving than metric ones; they require specialized software and can be computationally expensive (Croke and Jakeman 2008). Several physics-based hydrological models such as variable infiltration capacity (VIC) (Liang et al. 1994), RAPID (David et al. 2016), and Riverware (Zagona et al. 2001) have been developed in recent decades to estimate the response of a basin and the streamflow. In contrast, metric streamflow modeling tools are convenient in drawing a dynamic relationship between basin rainfall and streamflow of a river (Carcano et al. 2008).

For long-term streamflow prediction, considering stationary or nonstationary model parameters can have an effect on the prediction results. This chapter considers stationary parameters in the streamflow modeling module. Performing streamflow modeling with stationary model parameters is a common practice in literature; however, several factors can lead to non-stationarity in model parameters. Changes in channel flow geometry, systematic data errors, and changes in precipitation patterns in comparison with the calibrated model can be among the possible reasons behind non-stationarity (Westra et al. 2013). Several methodologies have been recently proposed to account for the effect of non-stationarity on streamflow modeling under changing hydrological conditions (Wallner and Haberlandt 2015; Pathiraja et al. 2016).

This chapter employs the hybrid conceptual-metric tool IHACRES (Croke et al. 2005) which uses statistical analysis to calibrate a streamflow prediction model and establish a relationship between the observed precipitation, temperature, and streamflow data. This relationship can be used to estimate the streamflow based on future precipitation and temperature profiles obtained from different GCMs. The tool uses a nonlinear module to convert observed rainfall into an effective rainfall and a linear module to convert the effective rainfall to streamflow. The model defines the effective rainfall, U_k as (Ye et al. 1997):

$$U_k = [c(\phi_k - 1)]pr_k \tag{2.1}$$

with

$$\phi_k = r_k + (1 - 1/\tau_k)\phi_{k-1} \tag{2.2}$$

and

$$\tau_k = \tau_w \exp(0.062\, f\,(T_r - T_k)) \tag{2.3}$$

in which c is the mass balance, ϕ_k is the soil moisture index, l represents the soil moisture index threshold, p is the nonlinear response term, and r_k is the observed rainfall. τ_k is the drying rate, τ_w is the reference drying rate, f is the temperature modulation, and T_r and T_k are the reference and drying temperature, respectively. The linear module finds the streamflow Q_k as:

$$Q_k = -\alpha Q_{k-1} + \beta U_{k-\delta} \tag{2.4}$$

Where α, β, and δ are the storage coefficient, fraction of effective rainfall, and the delay between the rainfall and streamflow, respectively. In addition, a second order transfer function is used to create a unit hydrograph as follows:

$$Q_k = \frac{b_0 + b_1 z^{-1} + b_2 z^{-2}}{1 + a_1 z^{-1} + a_2 z^{-2}} U_{k-\delta} \tag{2.5}$$

where z is the time-step shifter, a_i and b_i are fitted parameters that are defined based on the type of flow (i.e. quick or slow flow). Finally, the efficiency of the model is evaluated by computing the coefficient of determination that measures the fit between observed and modelled streamflow which is computed as follows:

$$R^2 = 1 - \frac{\sum \left(Q_o - Q_M\right)^2}{\sum \left(Q_o - \overline{Q_o}\right)^2} \tag{2.6}$$

where Q_o is observed streamflow value and Q_M is modeled streamflow value. Generally, R values greater than 0.75 are acceptable for big basins (Croke et al. 2005).

2.5. TIME DEPENDENT SCOUR PREDICTION

Scour depth is a key variable that significantly affects the time-variant performance of bridges subjected to flood conditions. Scour modeling is a process affected by several sources of uncertainty (e.g., modeling uncertainty and randomness in soil properties, bridge geometry, and

river discharge, among others). Local scour at piers is a function of bed material characteristics, bed configuration, flow characteristics, fluid properties, and the geometry of the pier and footing. In the U.S. bridge design and assessment practice, design specifications such as the AASHTO LRFD (2010) include recommendations for design of bridge piers against scour, which requires this design to be performed on the basis of an approved method for scour predictions. These methods are generally empirical equations with parameters calibrated mostly using experimental flume tests. These equations provide the maximum expected scour depth; the foundations must be placed under this depth to avoid scour failure.

In this chapter, the scour depth at piers is calculated based on Arneson et al. (2012). The time-dependent scour prediction process starts with identifying the approach velocity V_{appr} representing the water velocity at the location of interest and the pier width a. Next, the maximum pier scour at each day Z_{max} is computed as

$$Z_{\max} = 2.0\lambda y_1 K_1 K_2 K_3 \left(\frac{a}{y_1}\right)^{0.65} Fr_1^{0.43} \tag{2.7}$$

where λ is a factor accounting for modeling uncertainty, y_1 is the flow depth upstream of the pier, K_1 is correction factor for pier nose shape, K_2 is correction factor for angle of attack of flow, K_3 is correction factor for bed condition, a is the pier width, and Fr_1 is the Froude number given by

$$Fr_1 = \frac{V_{appr}}{\sqrt{(gy_1)}} \tag{2.8}$$

in which V_{appr} is the mean velocity of the flow directly upstream of the pier, and g is the acceleration of gravity (9.81 m/s^2).

Several empirical equations can be used for drawing a relationship between the discharge volume and the water velocity and depth. However, these equations may not be reliable for all locations

and channel types. Accordingly, the proposed approach employs a curve fitting technique to establish the relationship between the river discharge and the water velocity and depth. The nonlinear fitting process is based on the observed velocity and depth versus discharge data, at the location of interest, available through the United State Geological Survey database (USGS 2017).

Finally, the time dependent scour depth is calculated using multi flood accumulation model proposed in Briaud, et al. (1999a). The adopted scour depth prediction model is suitable for evaluating the time dependent scour depth in both cases of sand and clay (Briaud et al., 1999b). However, other scour prediction models can be easily accommodated in the proposed framework. Figure 2.1 presents the flowchart of the methodology implemented to establish time dependent scour depth prediction.

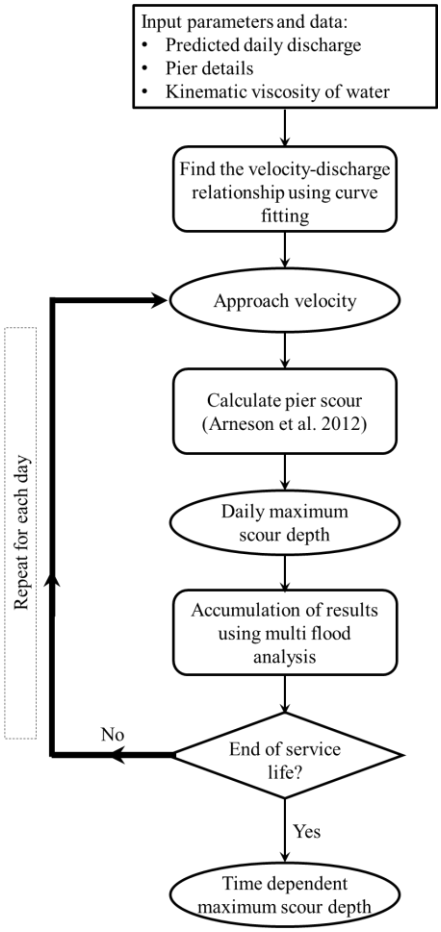

Figure 2.1. Flowchart of the adopted time-dependent scour prediction process

2.6. CAPACITY OF BRIDGE FOUNDATION

Although the proposed risk assessment approach is equally applicable to different types of bridge foundation, this chapter focuses on the capacity of pile foundation with steel H-piles. Lateral and axial limit states are considered to evaluate the behavior of this foundation type under horizontal and vertical loads. The ultimate lateral load carrying capacity H_L of one pile is (Prasad and Chari 1999)

$$H_L = 0.3\left(\eta K_P^2 + \xi K \tan\delta\right)\gamma a B(2.7a - 1.7L) \tag{2.9}$$

with

$$a = \frac{-\left(0.567L + 2.7e\right) + \left(5.307L^2 + 7.29e^2 + 10.541eL\right)^{0.5}}{2.1996} \tag{2.10}$$

where η is shape factor to account for the non-uniform distribution of earth pressure, K_p is passive earth pressure coefficient, K is lateral earth pressure coefficient, δ is interface friction angle between the pile and the soil, γ is effective unit weight of soil, a is depth to the point of rotation, B is diameter or width of the pile, L is embedded length of pile, and e is eccentricity of loading. In this model, shear resistance contribution from both the front soil and side soil is taken into account. In order to evaluate the capacity of each pile in the pile group, a reduction factor is applied to the capacity of a single pile (Hannigan et al. 1997). An equivalent circular diameter of H-pile is computed based on Reese and Van Impe (2010).

The ultimate axial load carrying capacity R_v is expressed as a sum of shaft resistance and toe resistance of a pile as:

$$R_V = R_s + R_p = f_s A_s + q_p A_p \tag{2.11}$$

where, R_s is the shaft resistance and R_p is the toe resistance of the piles. f_s is unit shaft resistance over the pile surface area, A_s is pile shaft surface area, q_p is unit toe resistance over the pile toe area, and A_p is pile toe area.

2.7. BRIDGE RISK ANALYSIS

In this approach, bridge piers are subjected to traffic live loads and dead loads computed using the AASHTO LRFD Bridge Design Specifications (AASHTO 2014). The adopted HL-93 live load model consists of the worst combination of the design truck plus design lane load or a design tandem plus design lane load. In addition, flood-induced lateral load F_L acting on bridge pier is calculated as (Cuomo et al. 2008):

$$F_L = p \times A \tag{2.12}$$

With

$$p = C_D \frac{\gamma}{2g} V_{appr}^2 \tag{2.13}$$

where A is the area of accumulated debris, p is water pressure on piers, C_D is drag coefficient, and V_{appr} is velocity of stream flow.

The load effects and load carrying capacity, performance functions are defined as

$$G_L(t) = R_L(t) - F_L(t) \tag{2.14}$$

$$G_V(t) = R_V(t) - F_V(t) \tag{2.15}$$

where $G_L(t)$ and $G_V(t)$ are the lateral and vertical performance functions at time t, respectively, $H_L(t)$ and $R_V(t)$ represent the respective time-variant lateral and vertical capacities, and $F_L(t)$ and $F_V(t)$ are the respective lateral and vertical load effects at time t. These performance functions are used to evaluate the probability of failure and risk due to flood and flood-induced scour.

In order to assess the failure probability of bridge foundation considering the time-variant scour under climate change, Monte Carlo simulation of the scour model, given by equation 2.7, is conducted in MATLAB environment (Mathworks 2016). This process uses the climate-based generated streamflow hydrographs and is used to draw samples from the scour depth at any time instance in the future given the climate scenario (i.e., for a certain GCM, downscaling method, and RCP value). The probability distribution function (PDF) of the time-variant lateral and axial capacity of the piles (given by equations 2.9 and 2.11, respectively) can be obtained using the simulation process. Next, the PDF of the time-variant flood loads are obtained from the generated climate-based river streamflow.

The PDFs of the time-variant capacity and load effects are next used within the Monte Carlo simulation to obtain the point-in-time probability of failure of the bridge pier as:

$$P_f(t) = P[any \quad g_i(t) < 0] \tag{2.16}$$

where $P_f(t)$ is point in time probability of failure and $g_i(t)$ is the i th performance function. The failure probability is computed as the failure probability of a system with failure modes connected in series. The cumulative annual probability of failure, representing the cumulative distribution function of the time to failure, is computed as (Decò and Frangopol 2011):

$$TDP(y) = \sum_{i=1}^{t} \left(P_{f,i} \prod_{j=1}^{i} \left(1 - P_{f,j-1}\right) \right) \tag{2.17}$$

where $TDP(y)$ and P_f are cumulative annual probability of failure and point-in-time annual failure probability of the piles. The risk of structural failure is established based on evaluated consequences as:

$$Risk(t) = TDP(y) \times C \tag{2.18}$$

where *Risk* (*t*) is the time dependent risk, and *C* represents the monetary value associated with bridge failure and calculated considering rebuilding cost C_{reb}, running cost C_{run}, and time loss C_{tl} due to the bridge failure and road closure. All of the costs are calculated in terms of U.S. dollars (USD) as (Stein et al. 1999)

$$C = C_{reb} + C_{run} + C_{tl} \tag{2.19}$$

where the rebuilding cost (C_{reb}) is estimated as a function of bridge area considering length and width of the bridge. In some cases, only some parts of the structure needs to be repaired or replaced, therefore, this consequence is also known as repair cost and is calculated as follows:

$$C_{reb} = C_{rc} W_b L_b \tag{2.20}$$

where C_{reb} is rebuilding cost ($) per unit area, W_b is bridge width (m), and L_b is bridge length (m). The running cost represents the additional expenses encountered through vehicle operation on the detour due to bridge closure and it is calculated as

$$C_{run} = C_{rv} DADTd \tag{2.21}$$

where C_{rv} is average cost of running vehicle ($/km), *D* is detour length (km), *ADT* is average daily traffic affected by bridge closure (vehicles/day), and *d* is duration of detour (days).

The time loss cost C_{tl} represents the loss of time per passenger for travelling through detour. This cost is calculated as:

$$C_{tl} = \left[C_1 O\left(1 - \frac{T}{100}\right) + C_2 \frac{T}{100} \right] \frac{DADTd}{S} \tag{2.22}$$

where C_1 is value of time per adult ($/hr.), C_2 is value of time for truck ($/hr.), S is average detour speed (km/hr.), T is average daily truck traffic (%), and O is occupancy rate. The flowchart of the risk analysis framework proposed in this chapter is shown in Figure 2.2.

The proposed bridge risk assessment framework contains various sources of uncertainty. The uncertainty associated with the final outcome can be addressed by regression or propagation methods. Second moment, structural reliability, and stochastic methods are among the main classes of uncertainty propagation approaches (Sudret 2007). Monte Carlo simulation is one of the widely and commonly used second moment methods in uncertainty propagation. Accordingly, it has been implemented in the proposed framework to account for various uncertainties associated with risk quantification.

The proposed framework contains four main modules: (a) flood prediction using climate modeling, (b) time-dependent scour prediction, (c) structural performance prediction considering floods and flood-induced scour, and (d) estimation of failure probability, failure consequences, and time dependent risk profile. As the first step of this framework, suitable global climate models for the region of interest should be selected along with associated downscaled precipitation and temperature profiles. Next, the discharge at the bridge location should be calculated using streamflow modeling techniques. This is performed herein through a hybrid conceptual-metric model which uses the historical records to establish a relationship between river discharge and precipitation and temperature patterns. The resulting river discharge profiles are then used to assess the scour propagation and structural performance. Next, the probability of bridge failure is computed using probabilistic simulations of the bridge performance function in terms of the resistance and load effects. The last module of this framework is focused on estimating the consequences of bridge failure and generating the time-dependent risk profile. As depicted in Figure 2.2, the proposed framework can identify the risk of bridge failure considering climate change. In this chapter, the framework has been applied to a steel girder bridge, However,

the framework can be applied to different bridges with various soil properties (clay, sand, etc.), scour types (pier scour, contraction scour, etc.), and structural systems.

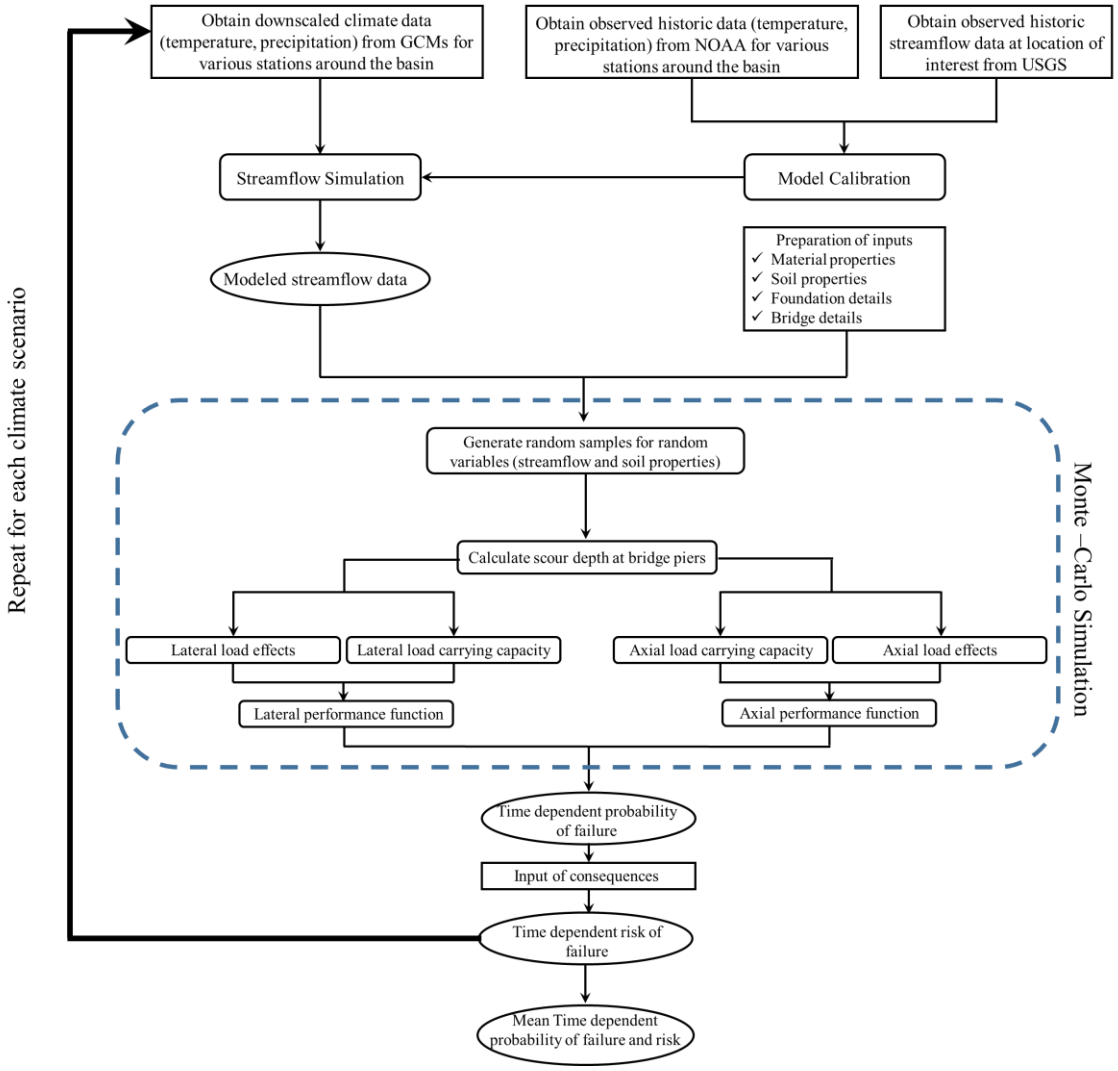

Figure 2.2. Flowchart of the proposed probabilistic approach for risk assessment under climate change

2.8. ILLUSTRATIVE EXAMPLE

The presented framework is illustrated on the South Bound I-35 Bridge over the Red River. The bridge serving a major freight route linking Southern and Northern US states is located on the Oklahoma-Texas border. This bridge accommodates an average daily traffic of 19,800 vehicles with 36% average daily truck traffic (FHWA 2016). During the past few decades, the Red River

has experienced several heavy floods which causing significant damage to surrounding areas. The most recent severe flood occurred in May 2015, in which the water reached the level of the superstructure. In addition, several other bridges along the Red River basin experienced partial or total failure during this flood (Fechter 2015; Danner and Fuller 2015). The I-35 bridge represents an ideal example due to its strategic location on a major freight route, the aggressiveness of flooding conditions on the Red River, the large daily traffic utilizing the bridge, and the lack of alternative routes in case of bridge failure.

The I-35 bridge superstructure consists of five plate girders supporting a reinforced concrete deck, while the substructure is composed of multiple piers supported by steel H-piles (Figure 2.3a). The bridge is 118.3 *m* long and 9.5 *m* wide, with two traffic lanes. The bridge has 11 piers and 32.3 *m* long spans. Since not all the characteristics of the bridge could be obtained, some assumptions related to dimensions were placed. These include the thickness of the concrete deck (35 cm) and the width of the bridge piers (1.2 m). Based on the original construction drawings, the riverbed level is considered to be 10 m below the deck. In this study, the failure risk analysis has been performed considering a single pier. However, system analysis covering all the piers can be performed using series-system reliability formulation. A layout of bridge pier with pile configuration is shown in Figures 2.3b and 2.3c. The studied bridge pier has two groups of 9 steel H-piles (HP 12x53 steel piles), each is 11.2 m long. Piles are aligned such that their strong axis is perpendicular to the direction of streamflow.

2.8.1. CLIMATE MODELING AND FLOOD PREDICTION

The downscaled climate data for MPI_ESM_LR, CCSM4, and MIROC5 global climate models downscaled using BCCA method with RCP 2.6, RCP 4.5, and RCP 8.5 are adopted from Brekke et al. (2013). In this study, two ensemble runs for each model and RCP combination are adopted. It should be noted that the framework can easily accommodate any number of runs and models

for the location of interest. The precipitation and temperature during the time window ranging from 1960 to 2100 is utilized.

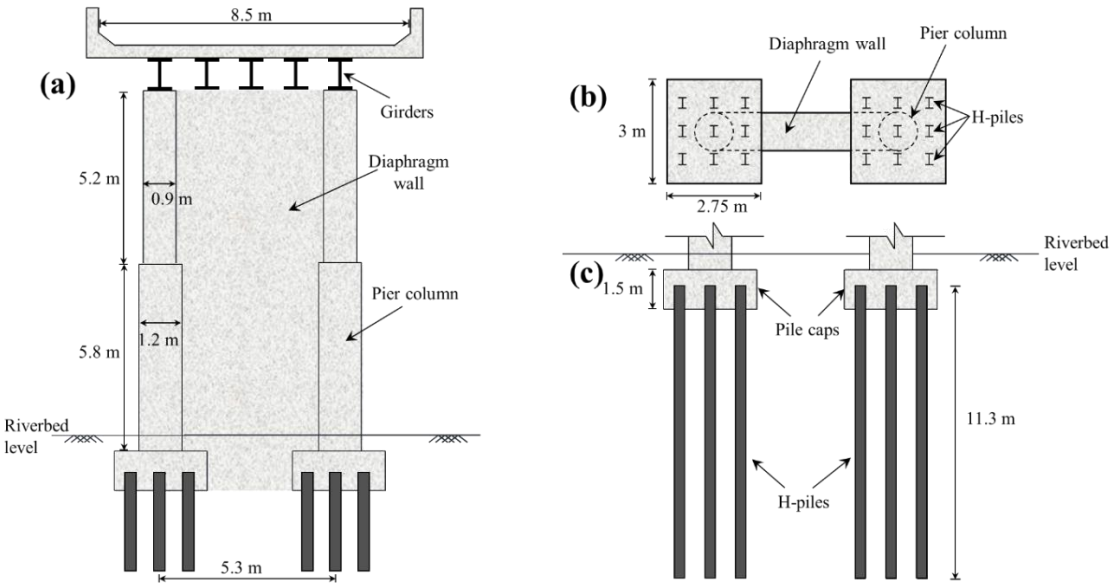

Figure 2.3. Layout of bridge pier with investigated pile configuration: (a) piers and superstructure; (b) plan view of pile caps; and (c) side view of pile caps and H-piles

The combination of three GCMs, three RCP values, and two model ensemble runs results in eighteenth different climate data sets. Table 2.1 shows the detailed information on the adopted climate scenarios. These selected GCMs were shown to provide reliable climate predictions for the location of interest (McPherson 2016). This has been performed through comparing the historical records of the region to the model predictions. The precipitation and temperature datasets are next used for streamflow prediction using IHACRES (Croke et al. 2005).

For the I-35 Bridge, the observed precipitation, temperature, and streamflow time-histories corresponding to the period of 2000-2015 are imported to the IHACRES for evaluating the accuracy of the prediction model. The observed streamflow datasets are adopted from the United State Geological Survey station on the Red River near Gainesville, TX (USGS ID: 07316000) (USGS 2017) located 300 m upstream of the bridge. The observed temperature and precipitation data is acquired from NOAA dataset (NOAA 2017) for the same time period. With an area of

almost 70,000 km^2 and 2200 km in length, the climate data within the Red River basin is subject to considerable variability due to the large basin size. IHACRES is a lumped model where the entire basin is treated as a single unit. Accordingly, the observed temperature and precipitation time-histories for 30 stations located throughout the basin are analyzed and their average time-histories are used as the lumped input for the river flow prediction. Next, the downscaled climate data of the same stations are also lumped and used to generate the future streamflow data at the location of interest.

Table 2.1. Adopted climate models for the investigated I-35 bridge

Modeling Center (or Group)	Institute ID	Model Name	RCP (W/m^2)	Resolutions	Datasets
National Center for Atmospheric Research	NCAR	CCSM4	2.6 4.5 8.5	1/8 degree	Max. temp. Min. temp. Precipitation
Atmosphere and Ocean Research Institute (The University of Tokyo), National Institute for Environmental Studies, and Japan Agency for Marine-Earth Science and Technology	MIROC	MIROC5	2.6 4.5 8.5	1/8 degree	Max. temp. Min. temp. Precipitation
Max-Planck-Institut für Meteorologie (Max Planck Institute for Meteorology)	MPI-M	MPI-ESM-LR	2.6 4.5 8.5	1/8 degree	Max. temp. Min. temp. Precipitation

Selection of the calibration period for climate prediction is related to the application of the model, if the model applies to flood peaks, then the calibration period should contain enough flood peaks to attain proper model calibration. In case of humid catchments, a two- or three-year calibration period is appropriate, while in arid or semi-arid areas a longer calibration period is usually needed (Croke and Jakeman 2008). For the location of interest in this chapter, a five-year calibration period from September 2004 to August 2009 is selected. The linear and nonlinear modules are used to draw a relationship between the observed rainfall and streamflow. The predicted data has a monthly R^2 value of 0.82 which meets the minimum recommended values (Croke et al. 2005).

Figure 2.4 shows a comparison between observed and modeled streamflow data from 2000 to 2016. As shown, a reasonable agreement between the observed and predicted data is achieved. Since the framework relies on the statistical parameters of streamflow peaks within each year, it is more important to achieve accurate prediction of the peak discharge intensity rather than its exact time.

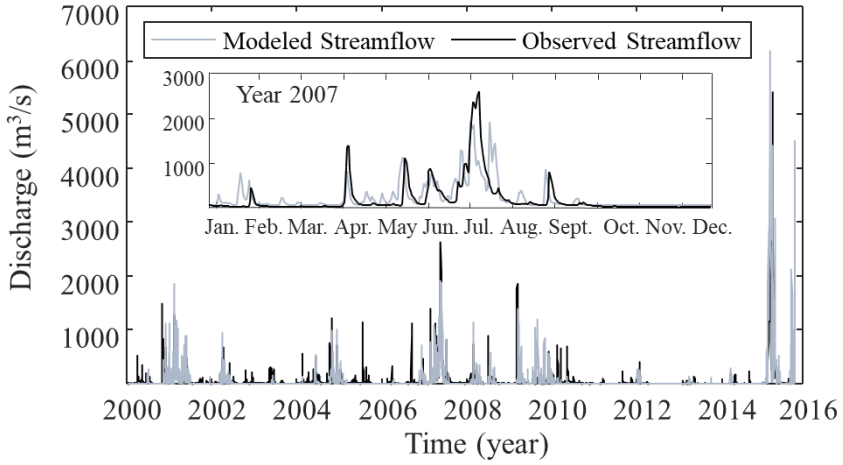

Figure 2.4. Comparison between observed and the modeled streamflow (calibration period September 2004 to August 2008)

After the calibration process, the downscaled temperature and precipitation datasets for the analyzed 30 stations are used and their average is calculated. These lumped values associated with each of the eighteenth climate scenarios (defined by different combinations of GCMs, RCPs, and ensemble runs) are used for predicting the streamflow. Next, the streamflow time-history associated with each climate scenario for the period of 1960 to 2099 is established using the achieved calibration parameters. Figures 2.5a, b, and c show the average precipitation, average temperature, and the predicted streamflow time series for CCSM4 model with RCP 2.6, respectively. Note that the users of the proposed framework can employ more detailed hydrological models to perform streamflow prediction for their location of interest. The results of such prediction can be easily implemented in the framework proposed in this chapter.

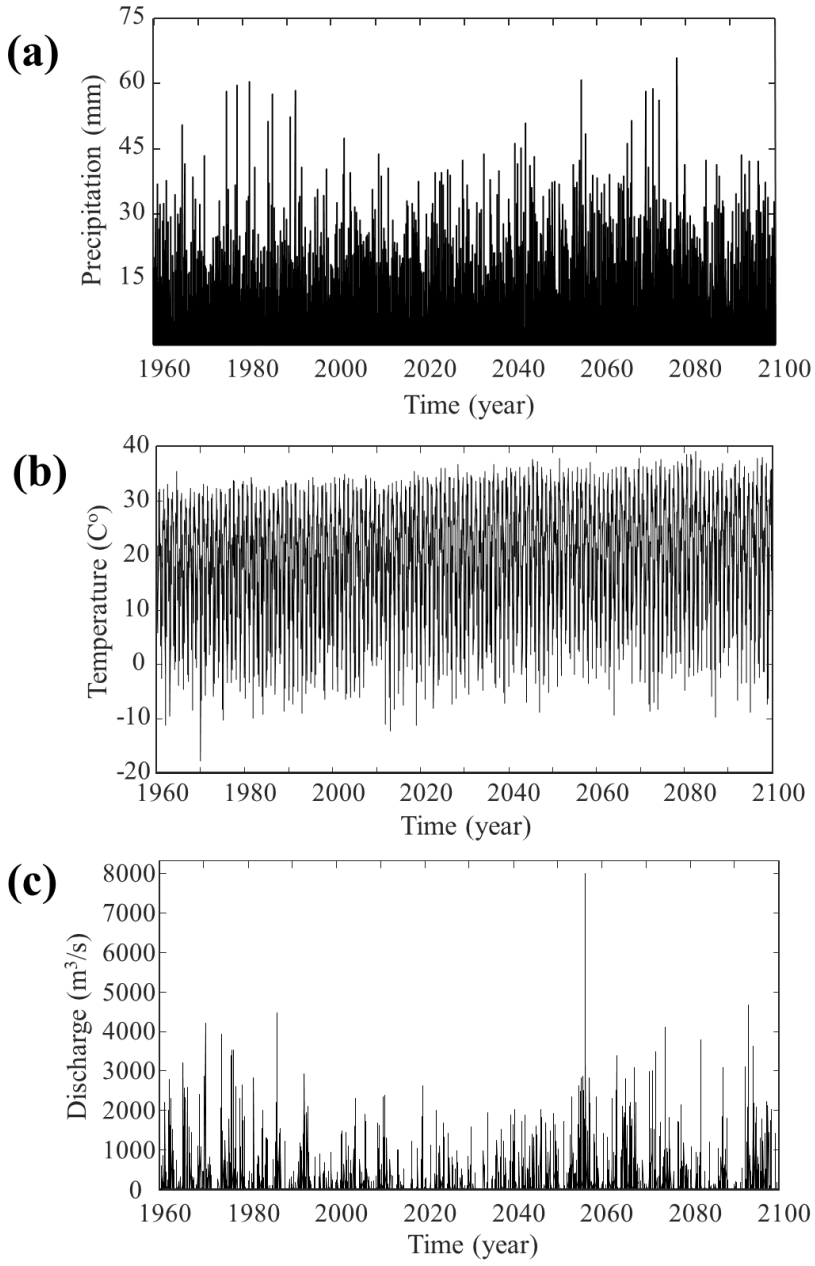

Figure 2.5. Average daily (a) precipitation; (b) temperature; and (c) streamflow based on CCSM4 model with RCP 2.6.

The analysis of predicted streamflow resulting from the considered climate models for the location of interest indicates that although the mean annual discharge during the period 1960 to 2100 is decreasing, the maximum annual discharge shows a steady increase. Figure 2.6a shows the annual discharge versus time for all of the adopted GCMs; additionally, it shows the mean and maximum annual discharge values, respectively. Figure 2.6b shows only the annual

maximum and mean discharge in addition the linear fit of these two profiles. The figure shows a clear trend indicating a decrease in the overall annual mean discharge. However, as indicated by the linear fit of the discharge peaks, the chance of having larger precipitation events is increasing. This highlights the importance of proper climate modeling during bridge risk assessment.

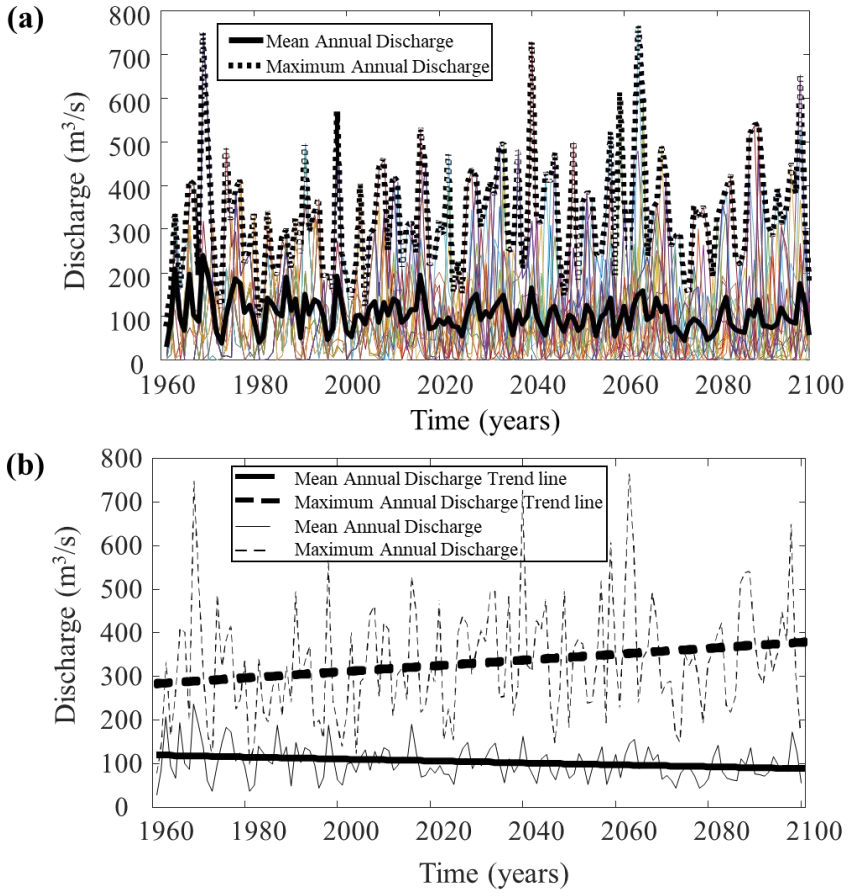

Figure 2.6. River discharge resulting from different climate scenarios:(a) mean and maximum annual discharge; and (b) linear fit of mean and maximum annual discharge

2.8.2. SCOUR PREDICTION AND RISK ASSESSMENT

Scour modeling for each streamflow time-series, corresponding to a given climate scenario, is performed using the equation 2.7. The implemented maximum scour-depth formulation requires water velocity and water depth as input parameters. The water velocity and depth can be predicted using empirical equations or using the observed data. In this chapter, the later method is

employed and the historical velocity and discharge data are used to establish a relationship between the velocity and discharge. These relationships for the investigated location have been constructed using the curve fitting technique in MATLAB curve fitting toolbox (MathWorks 2016). Figure 2.7 shows the results of the water velocity prediction. Water depth prediction is obtained in a similar manner.

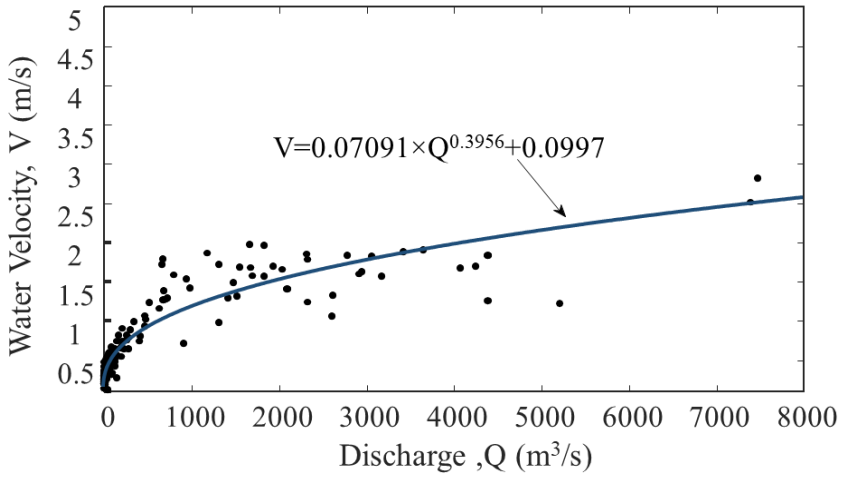

Figure 2.7. Curve-fitting results for establishing a relationship between water velocity and river discharge at the investigated location

The generated water velocity and depth time series for each climate scenario are then used to predict the maximum scour depth based on equation 2.7. The mean and coefficient of variation of the modeling uncertainty factor are assumed to be 0.44, and 0.79, respectively (Johnson et al., 2015). Time-dependent scour depth associated with different climate scenarios is then established. Figure 2.8 shows the time dependent scour depth profiles for all climate scenarios. As shown, there is a considerable variability in the scour depths among the considered scenarios. The results depict up to 30% difference in final scour depth between different climate datasets. This highlights the significant uncertainty associated with the scour prediction considering climate change and justifies the need for probabilistic analysis. In addition, the results of the scour depth show an increasing trend until it reaches the equilibrium scour level. Reaching the equilibrium level generally occurs in the first few decades and the subsequent increase is not

significant and is limited to 10-20% of the maximum scour depth. This increases after reaching the initial equilibrium level can be also justified by climate change effects.

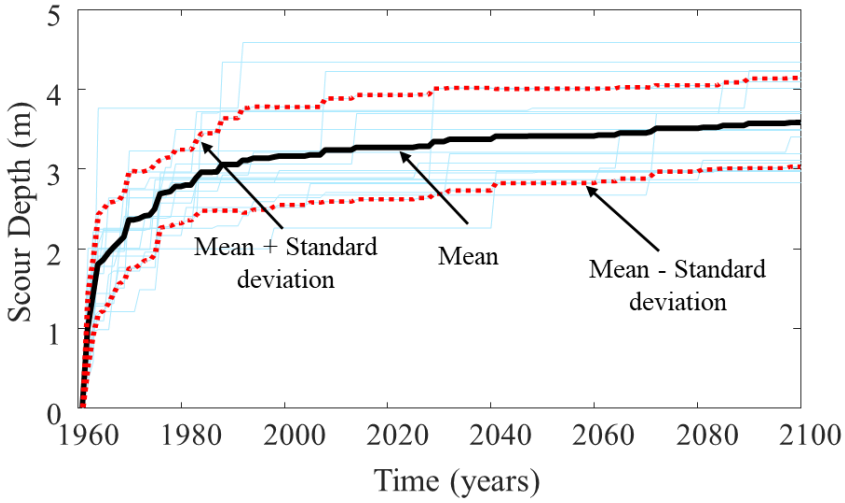

Figure 2.8. Time-dependent scour depth resulting from different climate scenarios

In order to consider this variability in the risk assessment, Monte Carlo simulation with 100,000 samples is used to draw samples from the time-variant scour depth at the investigated bridge pier. Next, each sample from the distribution is used to perform the time dependent scour depth prediction. In this chapter the soil is assumed to be coarse sand with medium erodibility which falls within category III of the erosion category proposed by Briaud (2008). The internal friction angle of soil is considered as a random variable that follows a normal distribution with mean value of 36° and standard deviation of 1.33 (Fellenius 1991). The unit weight of saturated soil is assumed 124 lbs /ft^3, and coefficient of lateral earth pressure is assumed 0.4. In addition to soil parameters, the streamflow is treated as a random variable. A probabilistic investigation is performed in order to establish the appropriate distribution parameters of the peak annual flow at the location of interest. A peak extraction analysis performed using MATLAB (Mathworks 2016) is carried out to isolate the peaks within each year. The best distribution type at 95% confidence level that fits the peaks is found. In this specific case study, the exponential distribution fits best the peak data. It should be noted that other probabilistic distribution

functions (e.g., generalized extreme value distribution or Pearson distribution) that fits the data of a given basin can be integrated into the framework. The predicted streamflow of each year is used to predict the parameter of the exponential distribution and the Monte Carlo simulation is used to find the annual histograms of the time-variant scour depth. The probabilistic scour depth is next used to calculate probability of failure using the performance functions given by equations 2.14 and 2.15.

Axial and vertical load capacity of the piles are calculated using equations 2.9 and 2.11. The shape factors η and ξ associated with the H-piles are assumed 1.0 and 2.0, respectively (Reese and Van Impe 2010). Monte Carlo simulation is used to estimate the load carrying capacity of the piles in axial and lateral directions. The results of scour depths are used to calculate the embedded length of the piles during each year. Next, axial and lateral load carrying capacities associated with each embedded length are then computed based on Equations 2.9 to 2.13. The profiles in Figure 2.9 show the mean and standard deviation of the probabilistic time-variant capacity of the piles in lateral and axial directions. In addition, the PDFs of resistance at the years 2000, 2030, and 2060 are shown in the figure. In addition, the PDFs of resistance at the years 2000, 2030, and 2060 are shown in the figure. It is shown that reduction in the lateral capacity reaches 50% at the end of the service life while the maximum reduction in axial capacity is 30%. Vertical loads from traffic and dead load of the structure are calculated based on AASHTO LRFD Specifications (AASHTO 2014) considering HL-93 loading to obtain maximum vertical forces on the bridge supports. Lateral load due to discharge is calculated using equation 2.12. With the probabilistic load and capacity terms in the limit state functions identified, the annual probability of failure can be obtained using the Monte Carlo simulation results.

After establishing the failure probability profiles, consequences due to bridge failure are evaluated considering repair cost, running cost, and time loss cost, calculated using equations 2.20, 2.21, and 2.22, respectively. The failure risk is then computed using equation 2.18. All the

parameters used in calculating the consequences are considered random variables, except the detour length (D) and the duration of detour (d). Table 2.2 presents the values of deterministic parameters and the descriptors of randomly distributed parameters used in calculating the failure risk.

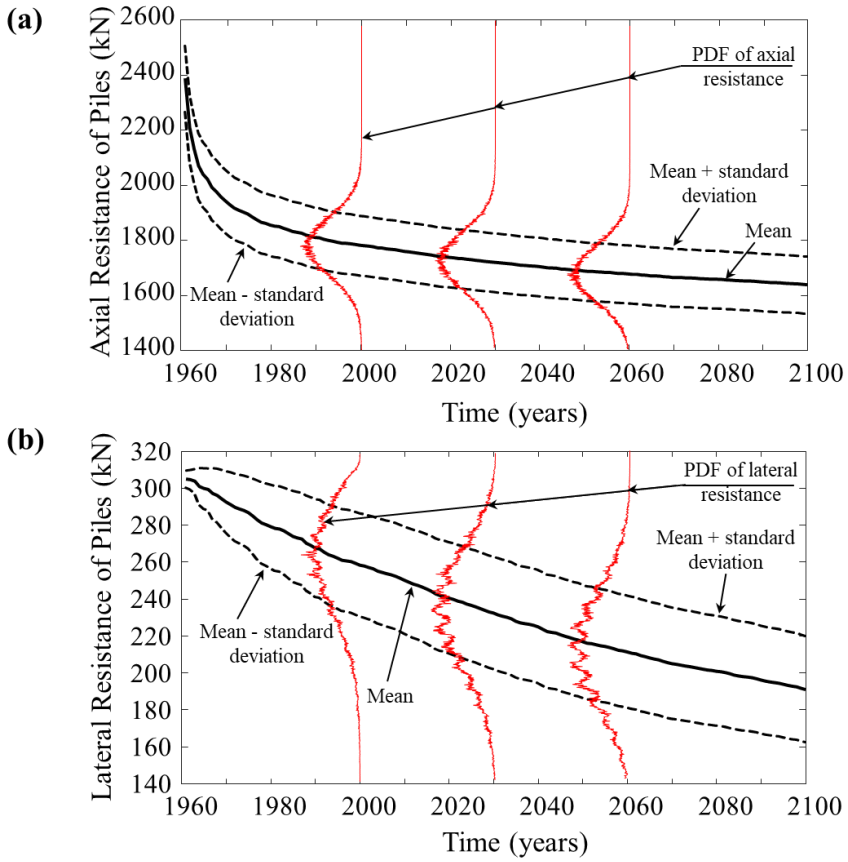

Figure 2.9. Time-variant resistance of piles in (a) axial direction; and (b) lateral direction

In this chapter, it is assumed that the effect of inflation negates the money interest; accordingly, the discount rate of money is assumed to be zero. The detour length is derived by analysis of the transportation network to which the bridge belongs. The area on the I-35 before and after the bridge is analyzed to identify alternative routes in case of bridge failure. The analysis indicates that the average travel time is 25 minutes with the intact bridge, while the detour will result in an average of 60 minutes travel time in case of bridge failure.

Table 2.2. Parameters for evaluating the rebuilding, running, and time-loss costs

Parameter	Notation	Value	Probabilistic Parameters	References
Rebuilding cost ($/m^2)	C_{rc}	\$894 / m^2	Lognormal, *COV*= 0.2	Deco & Frangopol (2011)
Average cost of running vehicle ($/km)	C_{rv}	\$0.08 / km	Lognormal, *COV* = 0.2	Deco & Frangopol (2011)
Detour Length	*D*	90 km	Deterministic	Estimated based on analysis of traffic network
Average Daily Traffic	*ADT*	19,800 vehicles/day	Lognormal, *COV* = 0.2	FHWA (2016)
Duration of detour	*d*	182.5 days (6 months)	Deterministic	Assumed
Cost of time per adult ($/hr.)	C_1	\$22.82	Lognormal, *COV* = 0.15	Deco & Frangopol (2011)
Cost of time for truck ($/hr.)	C_2	\$26.97	Lognormal, *COV* = 0.15	Deco & Frangopol (2011)
Average detour speed (km/hr.)	*S*	64	Lognormal, *COV* = 0.15	Deco & Frangopol (2011)
Average daily truck traffic (%)	*T*	36%	Lognormal, *COV* = 0.2	FHWA (2016)
Occupancy rate	*O*	1.5 adults	Lognormal, *COV* = 0.15	Deco & Frangopol (2011)

In order to compute the failure probability and risk, Monte Carlo simulation with 100,000 samples is employed. The point-in-time probability of failure is found using Equation 2.16. This equation employs the results of performance functions which are calculated using Equations 2.14 and 2.15. The point-in-time probability of failure is then used to generate the cumulative probability of failure using Equation 2.17. Figure 2.10a shows the mean point in time probabilities of failure for all climate models while Figure 2.10b shows the mean, mean plus one standard deviation, and mean minus one standard deviation of time dependent risk profile.

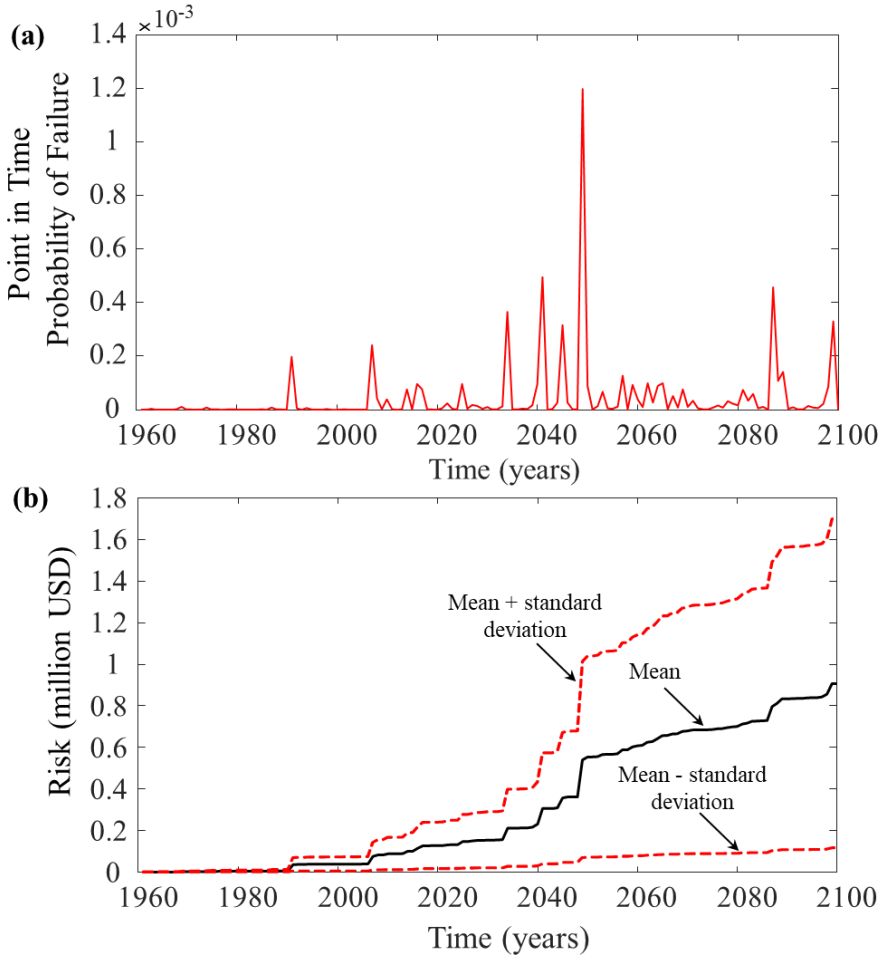

Figure 2.10. Results obtained based on all climate models: (a) point-intime probability of failure; and (b) time-dependent risk

2.8.3. IMPACT OF CLIMATE CHANGE ON BRIDGE FAILURE RISK

Since the main goal of the chapter is to evaluate the impact of climate change on the risk profile of a given bridge, the risk profile resulting from the proposed approach considering climate modeling is compared to the risk resulting from traditional approaches based on historical data. The streamflow data of the past 50 years (1960-2010) at the location of interest are extracted from the USGS database and used to generate future flood prediction. Two methods have been used for flood prediction with no consideration of climate change; (a) a traditional method where the historic 50-year record is repeated throughout the service life, and (b) a flood prediction based on the Q100-Q500 approach developed by Briaud et al. (2007). The Q100-Q500 approach uses the

estimated 100-year and 500-year floods (i.e. Q100 and Q500) to randomly generate daily streamflow data. Figures 2.11a and b shows the time dependent scour depth and mean risk profiles generated using the 50-year historic data, the Q100-Q500 approach, and the mean of all climate models. It can be seen that there is a considerable difference between the three risk profiles. As shown, the 50-year risk profile tends to underestimate the risk compared to the other two approached; while the Q100-Q500 predicted, at the end of the service life, approximately double the risk value established using proper climate modelling.

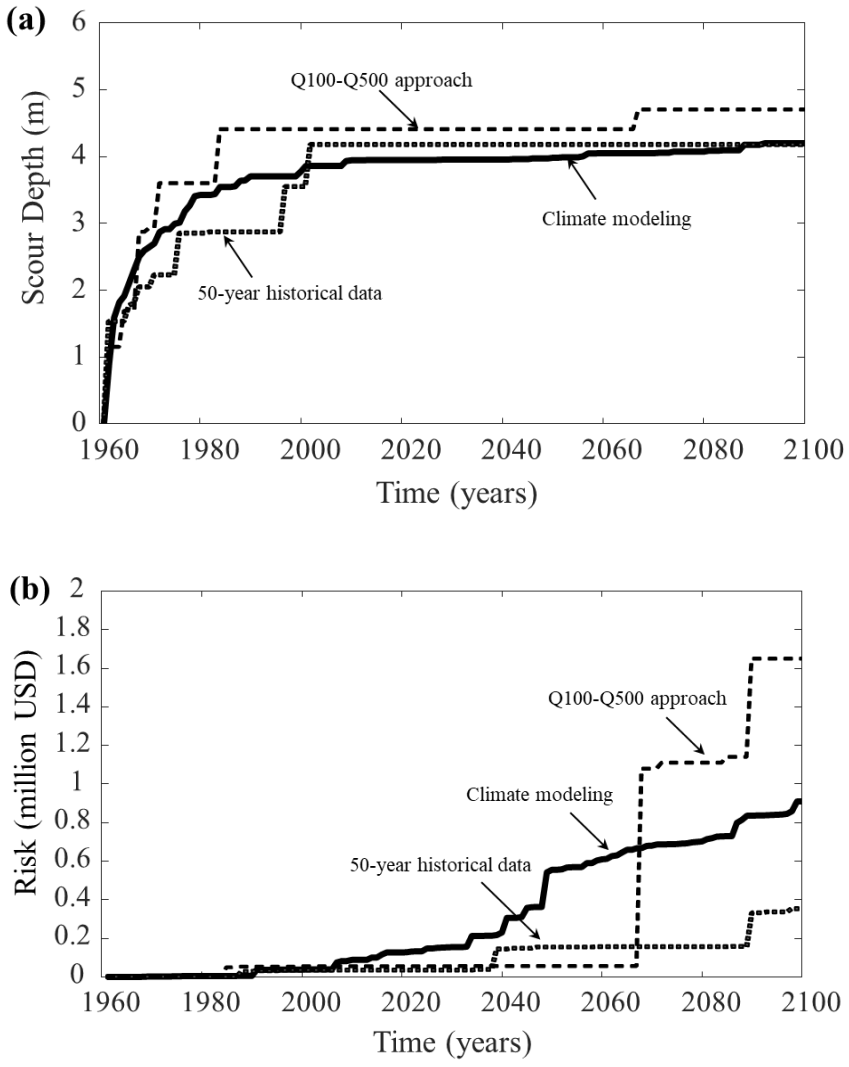

Figure 2.11. Comparison between results obtained from climate modeling, 50-year historical data, and Q100–Q500 approach for time-dependent (a) scour depth; and (b) risk profiles.

2.9. CONCLUSIONS

This chapter presents a probabilistic framework for risk assessment of bridges under flood and flood-induced scour considering climate change. The flood and streamflow prediction is performed using global climate models. The downscaled precipitation and temperature climate data are adopted from CMIP5 archive for the location of interest and the 1960 to 2100 time period. The IHACRES statistical model is used to convert the climate data to streamflow hydrographs at the bridge location. Time-dependent scour depth is quantified and its effect on the axial and lateral capacity of the bridge foundation is computed. The annual point-in-time failure probability of the bridge due to flood-induced loads is used to predict the cumulative failure probability profiles of the bridge foundation. After evaluating the consequences associated with bridge failure, the time variant bridge risk profile is established. The following conclusions are drawn:

- The time-variant scour depth significantly depends on the adopted climate scenarios. A variation of 29% in the final scour depth predicted using the different climate scenarios has been observed at the studied location. Accordingly, a probabilistic approach considering all potential scenarios is necessary to properly quantify the risk of bridge failure due to flood and flood-induced scour hazards.
- Analysis of the predicted streamflow considering climate data for the location of interest indicates that although the mean annual discharge has a general decreasing trend, the maximum annual discharge (i.e., flow peaks) shows a steady increase. This indicates a potential increase in the flood hazard and highlights the importance of proper climate modeling for bridge risk assessment.
- The MPI_ESM_LR model predicts the most aggressive time-dependent scour depth while MIROC5 model predicts the lowest scour depth for a given RCP. In addition, lower RCP levels generally result in a higher scour depth. Climate scenarios with RCP 2.6, regardless

of the associated climate model, predicted a higher scour depth compared to those with higher RCP levels. Furthermore, scenarios with RCP 8.5 predicted the lowest scour depth profiles.

- Traditional methods for streamflow prediction based on historic data can underestimate or over-predict the risk of bridge failure under flood and flood-induced scour depending on the assumptions used to establish the future streamflow data. In contrast, the proposed approach based on climate models provides a rational prediction of future risk while properly accounting for uncertainties associated with future climate and flood conditions.

CHAPTER III

ASSESSMENT OF TIME-VARIANT FLOOD FRAGILITY OF BRIDGES USING DEEP LEARNING NEURAL NETWORKS

3.1. OVERVIEW

Fragility analysis can assist infrastructure managers in properly quantifying the reliability of bridges under different flood hazard intensity levels. However, conducting such analysis while accounting for various uncertainties associated with bridge capacity, deterioration, and future climate conditions can significantly increase the computational cost of the bridge management procedure. To improve the computational efficiency of the fragility analysis while maintaining the desired accuracy, this chapter integrates deep learning neural networks in a simulation-based probabilistic framework for establishing time-variant fragility surfaces of bridges under flood hazard. Downscaled climate data, adopted from global climate models, are used to predict future precipitation and temperature profiles at a given location. Deep learning networks are employed with a twofold objective: (a) to predict the future river streamflow at the investigated location necessary for assessing the scour conditions and floodhazard at the bridge, and (b) to simulate the structural behavior of the bridge foundation under sour conditions. The trained deep learning networks are integrated into the probabilistic simulation process to quantify the failure probability and construct the bridge fragility surface under flood hazard. The proposed framework is illustrated on a bridge located in Oklahoma. The work in this chapter is based on the published papers Khandel and Soliman (2019d; and 2021).

3.2. BACKGROUND

Within the past few decades, extreme climate-related events (e.g., floods and hurricanes) were responsible for several cases of transportation infrastructure failure. Studies by Muis et al. (2015), Winsemius et al. (2016), and Wang et al. (2018), among others, predict a significant increase in the future flood hazard and attribute this increase to the effects of climate change. The alteration of temperature profiles, precipitation patterns, sea level, and frequency of coastal storms are examples of these effects (Neumann et al., 2015). A flood risk assessment conducted by Arnell and Gosling (2016) shows that climate change can be responsible for more than 180% increase in global flood risk by year 2050. Consequently, the vulnerability and failure risk of transportation structures may significantly increase unless new infrastructure management methodologies capable of accounting for this change are adopted. Bridges, in particular, should be a main focus of these management methodologies due to the potentially devastating and crippling consequences associated with their failure.

Accelerated scour, erosion of bridge approaches, and excessive loads due to direct water pressure and debris impact are among the mechanisms that may cause partial or total bridge collapse during floods (Ettouney and Alampalli, 2011). Scour can reduce the buckling resistance and lateral capacity of pile foundations or undermine the stability of shallow foundation. These effects increase the bridge vulnerability during future floods or other extreme events, such as earthquake excitations and traffic overloads (Hung and Yau, 2014; Banerjee and Ganesh Prasad, 2013; Ganesh Prasad and Banerjee, 2013). To properly assess bridge reliability under extreme events, a comprehensive approach capable of estimating the bridge performance under potential hazard intensities should be utilized. In recent decades, fragility models have gained broad acceptance by infrastructure mangers as a proper tool for performance assessment of structures under natural (e.g., seismic events and hurricanes) hazards. A fragility model is a function that represents the probability that the structure will reach or exceed a certain damage state given a specific hazard

intensity (Gidaris et al., 2017). Such models are widely used for earthquake assessment of different types of critical infrastructure, such as nuclear power plants and dams. They are also popular for performance assessment of bridges under the effect of seismic events (Wang et al., 2014a), tsunamis (Akiyama et al., 2012), hurricane-induced surge and wave hazard (Ataei and Padgett, 2012), or the combined action of multiple hazards (Banerjee and Ganesh Prasad, 2013; Wang et al., 2014b). Although river flooding is responsible for 28% of bridge failure in the U.S. (Cook et al., 2013), fragility models for bridges under river flood conditions are very limited (Gidaris et al., 2017).

Among the few flood fragility models available in literature, the Hazus® (Hazus, 2018) approach uses data from the National Bridge Inventory database (FHWA, 2016) to provide empirical failure probability values as a function of the flood return period and scour vulnerability rating. Due to the limited data available for model calibration, failure is defined by the presence of damage representing 25% of the bridge replacement cost (Hazus, 2018). However, since no detailed structural analysis is conducted, such qualitative models may not provide enough accuracy for proper application in infrastructure management. Turner (2016) constructed fragility curves for several bridges in Colorado considering hydro-dynamic uplift forces as the main failure criterion. The results were used to estimate the elevation change required to improve the bridge reliability against hydro-dynamic uplift forces. However, other flood-related failure modes such as pier failure due to scour or horizontal water pressure were not included. In addition, flood frequency was estimated based on probabilistic analysis of gage station records along the region of interest. However, the actual hazard occurrence probabilities may be subjected to significant variations due to climate change (Arnell and Gosling, 2016). In another effort, Kim et al. (2017) developed a flood fragility model for bridges that considers bridge scour, structural deterioration, and debris accumulation when computing the failure probability. Their study implemented finite element analysis coupled with reliability estimation. Due to the computational expenses related to

probabilistic analysis involving finite element modelling and Monte Carlo simulation, a simplified finite element model was integrated in their computational approach and the first order reliability method (FORM) was used to compute the failure probability under a limited number of random parameters.

In order to enable the use of finite element analysis in probabilistic simulations while maintaining a reasonable computational cost, some researchers resort to using approximation methods such as response surface analysis to generate an analytical relationship between the structural response and the underlying variables (e.g., Buratti et al., 2010; Park and Towashiraporn, 2014). This relationship can be next used in Monte Carlo simulation or other traditional reliability methods such as FORM. However, methods such as response surface and FORM can suffer from lack of accuracy in highly nonlinear problems or when multiple failure modes are to be considered (Kroetz et al., 2017; Song et al., 2018; Wang et al., 2018). Accordingly, using more advanced surrogate modeling techniques such as Polynomial Chaos Expansion (PCE), kriging models, and artificial neural networks can help in simulating complex and nonlinear structural systems considering multiple failure modes. In this regard, methods based on ANNs were shown to converge faster and offer a lower computation time for complex functions compared to PCE and kriging models (Kroetz et al., 2017). Therefore, the use of computationally efficient approaches is needed to enable the proper integration of detailed finite element modelling in fragility analysis of bridges under flood hazard. This approach should also consider the full set of random variables associated with bridge resistance, load effects, and hazard occurrence probability in light of changes expected to occur due to long-term variability in climate trends.

ANNs are often known as systems with black box nature, meaning that their parameters are generally uninterpretable (Zhang et al., 2002). However, most of other surrogate modeling techniques such as local Gaussian processes, polynomial response surfaces, support vector machines, and kriging models also approximate the response function without having a physical

understanding of the system processes (Ferrario et al., 2017). Given the complexity of the functions to be simulated by ANNs, these models may require large number of samples to be fully trained. However, ANNs can be also integrated with adaptive experimental design procedures to reduce the number of samples required for their training (Gomes, 2019). The availability of several cloud computing resources for machine learning applications and the adaptation of advanced and efficient optimization algorithms can assist in managing the computational expenses associated with these models.

This chapter addresses this need by presenting a probabilistic framework that relies on deep leaning neural networks for assessing the time-variant fragility of bridges under floods and flood-induced scour considering the future variability in climate. The proposed framework uses downscaled global climate modeling data to predict future time-dependent scour profiles under various climate scenarios. A deep learning tool (DN 1) is employed to perform streamflow prediction based on future precipitation and temperature profiles throughout the basin. The predicted streamflow profiles are then used in probabilistic simulation to predict the long-term scour depth and flood hazard. A finite element (FE) model is used to produce a dataset necessary for training a second deep learning network (DN 2) capable of predicting the response of the bridge foundation under flood and flood-induced scour. The effect of long-term material degradation (i.e., corrosion) is taken into account. The second trained deep learning network (DN 2) is then integrated in a Monte Carlo simulation that predicts the failure probability and generates the fragility surface. The fragility surface represents the bridge failure probability associated with a given service life and river discharge as the hazard intensity measure.

3.3. CLIMATE DATA ANALYSIS

Over the past few decades, significant research effort has been devoted to studying the climate behavior and predicting future climate trends (e.g., Sheffield et al., 2013a). The fifth phase of Coupled Model Intercomparison Project (CMIP5) is an innovative tool that provides an overall

understanding of the past and future climate trends (Taylor et al., 2012). More than 50 different models capable of projecting past and future climate are included in the CMIP5 dataset. The models are different in terms of model formulations, experiment conditions, climate noise, and model resolutions. In addition, multi-model ensembles are used to assist in considering the effect of uncertainties associated with a given model (Taylor et al., 2012). Due to the high computational cost associated with reliability analysis under climate change, employing all available climate models may not be feasible. In addition, not all climate models can generate appropriate results for every location; accordingly, Global Climate Models (GCMs) should be carefully selected. Selection of suitable GCMs for the location of interest can be performed through the comparison of GCM climate data to the observed historical records (Samadi et al., 2010).

Future greenhouse gas (GHG) emission scenarios represent another main source of uncertainty in climate prediction. The recent climate modeling practice defines the emission scenarios based on radiative forcing trends (Moss et al., 2010). Representative concentrative pathways (RCPs) characterize the radiative forcing which is defined as the difference between absorbed insolation energy and the radiation energy reflected by the earth. RCP 2.6, RCP 4.5, RCP 6.0, and RCP 8.5 are the four commonly used RCP cases. Different RCPs can be considered to account for the effect of variability of GHG emission and concentration pathways, as well as land use and future land cover (Shrestha et al., 2016b).

The GCM results are typically constructed in large spatial resolutions (125 to 500 km grids). Since hydrological impact studies require fine resolution data (typically 10 to 30 km grids), the coarse resolution of the GCMs will not be appropriate for regional scale predictions (Frost et al., 2011). Conversion of coarse resolution to fine resolution data can be performed using dynamic or statistical downscaling methods. The daily bias correction constructed analogs (BCCA) downscaling technique (Maurer et al., 2010) is adopted in this chapter. This technique is a hybrid

statistical method that employs both the quantile mapping bias correction and daily downscaling techniques to perform the downscaling. Maurer et al. (2010) shows that the hybrid performance of this model results in highly accurate climate prediction in regional scales. However, to account for uncertainties associated with the downscaling process, multiple downscaling techniques should be analyzed and the most appropriate ones for the location of interest can be included in the climate scenarios (McPherson et al., 2016). With the presence of several climate modelling variables, multiple climate scenarios can be defined, each of which is characterized by its own GCM, downscaling techniques, and RCP values. A total of 18 climate datasets, composed of three different GCMs, three RCP cases, and two ensemble runs of each model, are used herein. For each combination of climate model and emission scenario there are different ensemble runs with different initial condition assumptions. Different initial conditions lead to a slight fluctuation in model projections. However, the effect of internal variability of the models (i.e., under different initial conditions) decreases significantly in the long-term. This is especially true, when compared to other sources of uncertainties such as model uncertainty (different models) and scenario uncertainty (different future emissions pathways). The quantification of the effect of different uncertainties on climate prediction has been discussed in more depth in several studies (e.g., Hawkins and Sutton 2009; Yip et al. 2011).

3.4. LONG-TERM PIER SCOUR PREDICTION

Flood-induced scour can significantly affect the time-variant strength and stability of bridges subjected to flood conditions. Several scour depth prediction approaches (e.g., Breusers et al., 1965; Briaud et al., 2001) are available in literature. These formulations, which are mostly developed based on flume test experiments can account for the effects of pier size, shape, and alignment on the maximum expected scour depth. Erosion in cohesion-less soils generally occurs on a particle-by-particle basis (Arneson et al., 2012). This accelerates the scour initiation rate such that the maximum scour depth is reached within few hours or during few flood events. In

contrary, the resistance of cohesive soils against erosion highly depends on the electromagnetic and electrostatic interparticle forces which lead to slower scour rate (Arneson et al., 2012). Scour rate in different soil materials can be quantified using erosion function apparatus (EFA) test (Briaud et al., 2001). This test quantifies the equivalent time (t) required to erode 1 mm of soil under various flow velocities (v). The erosion rate ($\dot{Z} = \frac{1}{t}$ in *mm*/*hr*) and the hydraulic shear stress acting on the soil (τ) are quantified based on the results of the EFA test.

The maximum pier scour depth (Z_{max}) is computed as (Arneson et al., 2012)

$$Z_{\max} = 2.0\lambda_1 y_1 K_1 K_2 K_3 \left(\frac{a}{y_1}\right)^{0.65} Fr_1^{0.43} \tag{3.1}$$

where λ_1 is a factor accounting for modeling uncertainty, y_1 is the flow depth upstream of the pier, K_1 is correction factor for pier nose shape, K_2 is correction factor for angle of attack of flow, K_3 is correction factor for bed condition, a is the pier width, and Fr_1 is the Froude number given by

$$Fr_1 = \frac{V}{\sqrt{(gy_1)}} \tag{3.2}$$

in which V is the mean velocity of the flow directly upstream of the pier and g is the acceleration of gravity (9.81 m/s^2). The time dependent scour depth (Z) is computed as (Briaud et al., 2001)

$$Z = \frac{t_i}{\frac{1}{\dot{Z}_i} + \frac{t_i}{Z_{\max i}}} \tag{3.3}$$

where $\dot{Z}_i$, Z_{maxi}, and t_i represent erosion rate, maximum scour depth, and duration of the i^{th} flood, respectively. The predicted time dependent scour based on this model highly depends on the erosion rate ($\dot{Z}_i$). For soils with large erosion rates (e.g., in clean fine sand), the time-dependent

scour depth will reach the maximum depth in a short period of time while for soils with small rate (e.g., in highly cohesive clays), the predicted scour depth may represent a small fraction of the maximum scour depth (Briaud et al., 2001).

3.5. APPLICATIONS OF DEEP LEARNING IN THE FRAGILITY ANALYSIS

Quantifying the probability associated with the infrastructure failure relies on the ability to predict the structural behavior under the effect of natural and/or human-induced hazards, while considering the potential deterioration due to aging. Performing these predictions involves complex physical-based simulations that can be highly expensive from a computational perspective. This problem is exacerbated when probabilistic analysis is required to account for various uncertainties associated with capacity and load effects. Machine learning can accelerate this process and assist in performing complex simulations that are not possible with traditional techniques (Shen, 2018).

In recent years, deep learning (DL) has been instrumental in solving computationally intensive problems in various fields of science and engineering including medical image diagnosis (Sun et al., 2016), autonomous vehicles (Tian et al., 2018), and visual object recognition (Karpathy and Fei-Fei, 2015). The deep nature of these algorithms allows for better representation of complex functions compared to other machine learning algorithms. Several deep learning frameworks, such as Caffe™ (Jia et al., 2014) and TensorFlow™ (Abadi et al., 2016) have been developed in recent years. Owing to its programmatic approach, TensorFlow™ framework is adopted in this chapter to train deep feed-forward neural networks. The detailed layout of such networks is shown in Figures 3.1, respectively. Neural networks are generally composed of three types of layers; input, hidden, and output layers. An input layer is responsible for feeding the input parameters ($\boldsymbol{X}$) to the network. Each hidden layer ($h^{(m)}$) consists of several neurons (h_{nm}) responsible for converting the input units to nonlinear functions of linear combinations of assigned weights and bias values as

$$h_{nm}^{(m)} = f\left[\sum\left(w_{n,n}^{(m)} x_{n,n}^{(m)} + b_{n,n}^{(m)}\right)\right] \quad (3.4)$$

where $w_{n,n}^{(m)}$ and $b_{n,n}^{(m)}$ represent the weight and bias value assigned to the given input, respectively. The framework then optimizes the assigned weights and bias values and train the network by minimizing the error in prediction (Rampasek et al., 2016). TensorFlow™ employs a single dataflow graph to perform input preprocessing and mathematical operations in a machine learning environment. Each graph is made of several vertices (i.e., nodes) and edges. The vertices represent units of local computations and the edges represent the inputs or outputs routs to/from the vertices. In TensorFlow™, the computations at vertices and the numerical flow along the edges are referred to as operations and tensors, respectively.

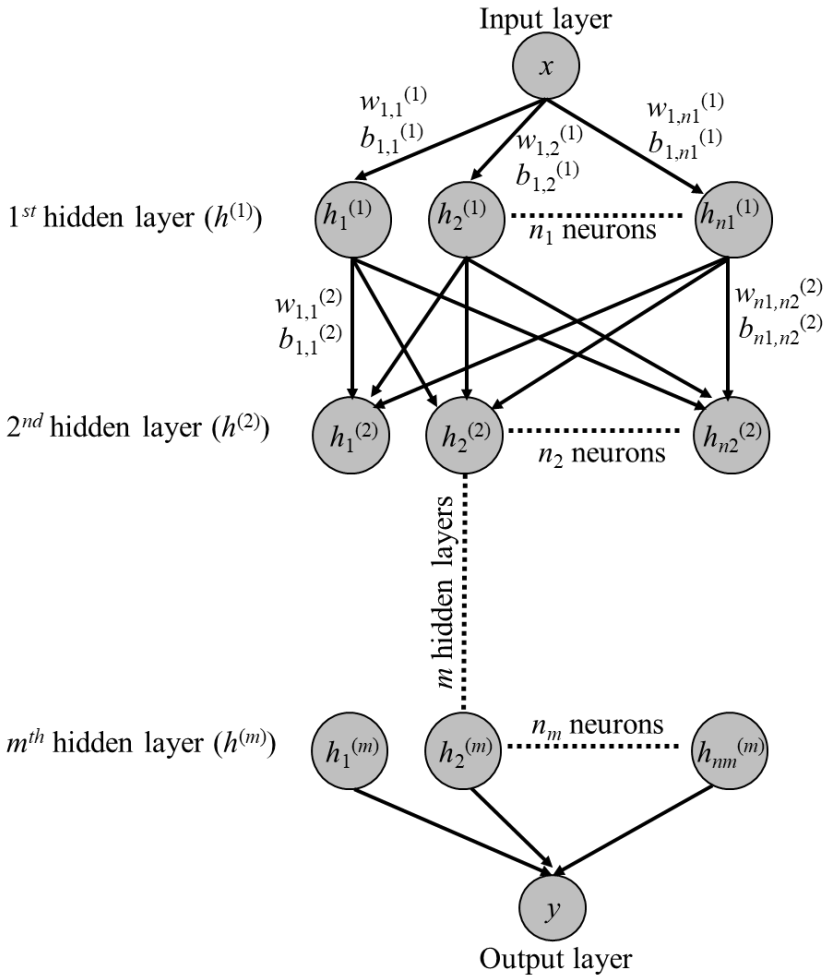

Figure 3.1. Detailed layout of feed forward neural networks

3.5.1. STREAMFLOW AND FLOOD PREDICTION

In this chapter, results of global climate modelling are employed to quantify future flood hazards. GCMs provide climate related parameters such as future precipitation and temperature profiles; however, flood prediction using these parameters remains a challenging task. Estimating the river discharge based on precipitation and temperature profiles requires detailed hydrologic modeling of the basin under consideration. Such detailed hydrological analysis may require considerable amount of resources or tools that may not be available to infrastructure managers. Applying innovative computational approaches such as machine learning can streamline this process and lead to a computationally efficient, yet highly accurate, streamflow predictions. This chapter adopts TensorFlow™ to predict future river discharge profiles based on downscaled temperature and precipitation data associated with different climate scenarios. It should be noted that common practice in streamflow prediction using statistical or hydrological streamflow prediction methods often rely on stationary assumptions (Humphrey et al., 2016). Several factors such as changes in channel flow geometry and precipitation patterns in comparison to historical records can be among the possible reasons behind non-stationarity (Westra et al., 2013). The streamflow modeling approach implemented in this chapter using deep learning neural networks assumes stationary parameters. More details regarding the employed deep network for predicting the future river discharge, denoted by DN 1, will be presented later in this chapter.

3.5.2. BEHAVIOR OF BRIDGE FOUNDATIONS UNDER FLOOD AND FLOOD-INDUCED SCOUR

This chapter focuses on fragility assessment of bridges with deep foundations. Several strength and serviceability limit states are considered to evaluate the time-variant reliability of the foundation under horizontal and vertical loads. OpenSees™ finite element software (Mazzoni et al., 2006) is employed to simulate the response of the pile group under applied loads. The piles

are modeled as a series of displacement-based beam-column elements and nonlinear springs. In addition to the aforementioned elements, pile nodes, fixed spring nodes, and slave spring nodes are also defined. The beam-column elements are used to model the pile elements while the springs, created using zero-length elements in the horizontal and vertical directions, are responsible for simulating the soil behavior.

The lateral soil behavior is simulated using *p-y* springs (API, 1987) while the shaft and tip behavior are modeled using the *t-z* (Mosher, 1984) and *Q-z* (Vijayvergiya, 1977) springs, respectively. Several parameters including the internal friction angle (ϕ), unit weight (γ), and shear modulus (G) of the soil are used for defining the springs. All nodes are three-dimensional with six transitional and rotational degrees of freedom. The pile elements, fixed springs, and slave nodes are vertically distributed along the embedded length of the pile. The embedded length of the piles is adjusted with respect to scour depth predictions (i.e., the embedded length of the pile L_2 = total pile length – scour depth Z). A schematic of the employed FE model is presented in Figure 3.2.

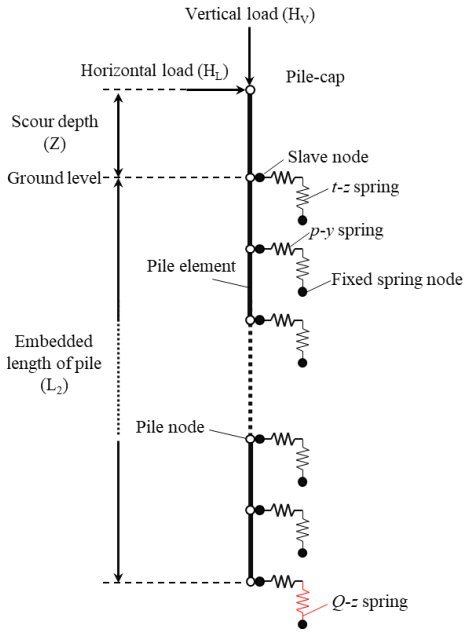

Figure 3.2. A schematic layout of the simulated pile in OpenSees™

Evaluating the behavior of closely-spaced pile groups under lateral and axial loads requires considering the effects of pile-soil-pile interactions. These effects often lead to a reduction in the soil resistance and can be addressed by applying appropriate modifications to the response of single piles (Brown and Reese, 1988). For laterally loaded piles, modified *p-y* curves accounting for group effects can be established by applying the reduction factors to the *p*-values (Dunnavant and O' Neill, 1986). In addition, the behavior of pile groups under axial loads can be modified using efficiency factors (O' Neil, 1983). In this chapter, resistance reduction factors accounting for the group effects in the lateral direction are defined based on experimental work conducted by Dunnavant and O'Neill (1986). The developed FE model is used to generate the required training dataset for a second TensorFlow™ deep neural network denoted herein by DN 2. Full factorial experimental design (Dieter, 2000) is used to generate an inclusive training dataset that covers the possible range of input parameters encountered in the next analysis steps. The trained deep network (i.e., DN 2) is then integrated into the probabilistic analysis to establish the bridge fragility under flood loads.

3.5.3. LONG-TERM CORROSION EFFECTS

Corrosion of steel piles can result in reduction of capacity under lateral and axial loading conditions. This reduction is often caused by loss of section thickness due to aggressive environmental conditions or repetitive dry-wet cycles (ElGawady et al., 2019). Several factors such as moisture, sulfate, chloride, and micro-organism contents affect corrosion losses. Resistivity, chemical composition, and pH of the soil, as well as the position of water table and oxidation potential, were shown to also affect the corrosion propagation in steel piles (Ding, 2019). Available literature suggests that corrosion rate in soil decreases with time (e.g., Schlosser and Bastick, 1991). This is mainly attributed to the depletion of oxygen and formation of a protective layer from the corrosion products (Ohsaki, 1982). Accordingly, time-dependent relationship for corrosion rate can be presented as (Kucera and Mattsson, 1987)

$$\Delta_e = kt^n \tag{3.5}$$

where Δ_e is thickness loss due to corrosion in μm, t is the exposure time in years, k is a multiplying constant, and n is the exponential constant.

3.6. FAILURE MODES AND CORRESPONDING PERFORMANCE FUNCTIONS

Dead and traffic live loads, acting on the bridge are defined based on AASHTO recommendations (AASHTO, 2017). HL-93 live load model is adopted to compute maximum axial load effects acting on the bridge foundation. Hydrodynamic flood-induced load (F_{dyn}) is calculated based on FEMA 55 (2011) recommendations as

$$F_{dyn} = \frac{1}{2} C_d \rho V^2 A \tag{3.6}$$

where C_d is drag coefficient, ρ is Mass density of fluid (9.81 kN/m^3 for fresh water), V is water velocity, and A is the surface area of obstruction normal to flow. The load effects and foundation capacity are used to define performance functions in the form of

$$G_i(\mathbf{X}) = R_i(\mathbf{X}) - LE_i(\mathbf{X}) \tag{3.7}$$

in which $G_i(\mathbf{X})$ is the performance function associated with the i^{th} limit state and the corresponding set of random variables $\mathbf{X}$. $LE_i(\mathbf{X})$ and $R_i(\mathbf{X})$ represent the load effects and the capacity of the foundation, respectively. Four performance functions are defined to cover (a) failure of the piles under combined effects of axial and flexural loads (b) shear failure under lateral loads, and (c) lateral deformations and (d) angular distortion (A_d) exceeding allowable limits (Hannigan et al., 2016). The interactive axial-flexural limit state considers the piles buckling capacity taking into account the increase in the unbraced length due to scour effects, while the flexural limit state considers the nominal bending capacity of the piles based on the

elastic and plastic properties of the H-pile section. The nominal plastic shear capacity is accounted for in the shear limit state (AASHTO, 2017). These limit states are suitable for bridge with deep H-pile foundations. Bridges with other foundation types can also be analyzed using the proposed framework with the definition of appropriate limit states that reflect potential foundation failure modes.

3.6.1. SERVICEABILITY LIMIT STATES

The serviceability performance functions corresponding to lateral deformation and angular distortion are defined, respectively, as

$$G_1(\mathbf{X}) = \Delta_{\text{limit}}(\mathbf{X}) - \Delta_{LE}(\mathbf{X}) \tag{3.8}$$

$$G_2(X) = A_{d,\text{lim}\,it}(X) - A_{d,LE}(X) \tag{3.9}$$

where Δ_{limit} and Δ_{LE} are, respectively, the displacement limit and load effects while $A_{d,limit}$ and $A_{d,LE}$ are angular distortions corresponding to the defined limit and load effects, respectively.

3.6.2. SHEAR FAILURE LIMIT STATE

The shear performance function $G_3(\mathbf{X})$ is defined as

$$G_3(\mathbf{X}) = 0.58\lambda_2 CF_y d_w t_w - V(\mathbf{X}) \tag{3.10}$$

where λ_2 is a factor accounting for modeling uncertainty, C is the ratio of shear-buckling resistance to shear yield strength, F_y is yield strength of the steel material, d_w *and* t_w are the web depth and thickness of the pile section. $V(\mathbf{X})$ is the shear load effect under the applied loads F_{dyn}. The shear load effect is also a function of the soil friction angle ϕ, corrosion rate, and the scour depth.

3.6.3. COMBINED AXIAL AND FLEXURAL FAILURE LIMIT STATE

The combined axial and flexural performance function for slender cross sections can be presented as

$$G_4(\mathbf{X}) = \lambda_3\lambda_4 - \left(\frac{P(\mathbf{X})}{P_n} + \frac{M_x(\mathbf{X})}{M_{nx}} + \frac{M_y(\mathbf{X})}{M_{ny}} \right) \tag{3.11}$$

where λ_3 and λ_4 are a factors accounting for uncertainty associated with modeling of combined axial and flexural resistance (Galambos, 2004). $P(\mathbf{X})$, $M_x(\mathbf{X})$, and $M_y(\mathbf{X})$ are the axial load and bending moments about *x* and *y* axes, respectively. P_n is the nominal compressive resistance, while M_{nx} and M_{ny} are the nominal flexural resistance about the *x* (i.e., strong) and *y* (i.e., weak) axes. The nominal axial load capacity P_n and bending moment capacities can be found in accordance with Sections 6.9 to 6.12 of AASHTO (2017).

3.6.4. PROBABILITY OF FAILURE USING MONTE CARLO SIMULATION

In this chapter, it is assumed that failure of each of the defined performance functions results in failure of the whole system. In other words, the limit states are defined as series system. Monte Carlo simulation is used to compute the probability of failure of the bridge foundation P_f as (Melchers and Beck, 2018)

$$P_f = \int \ldots \int I[\ ] f_{\mathbf{X}}(\mathbf{X})\, d\mathbf{X} \tag{3.12}$$

where $I[\ ]$ is the indicator function for a series system *f* in form of:

$$I[\bigcup_{i=1}^{m=4} G_i(\mathbf{X}) \le 0] = 1 \qquad \textit{if [ ] is true} \tag{3.13}$$

$$= 0 \qquad \textit{if [ ] is false}$$

where m is the number of considered performance functions (four herein) and $G_i(\boldsymbol{X})$ represents the i^{th} performance function corresponding to vector of random variables $\boldsymbol{X}$.

Note that accuracy of Monte Carlo simulation highly depends on the number of samples. Based on recommendations by Bronding et al. (1964) and Melchers and Beck (2018), the first estimate of number of samples (N) can be considered as

$$N > \frac{-\ln(1-C)}{P_f} \tag{14}$$

where C is the confidence interval, P_f is the probability of failure, and N is the number of required simulations. This estimate provides a minimum required number of simulations. Other estimates for the required number of samples (e.g., Shooman, 1968; Ang and Tang, 2007; Mann et al., 1974) are also available in literature. However, these methods do not offer a measure for the accuracy of the performed simulation. One of the most useful tools for identifying the adequacy of the number of simulations is to plot progressive results of the probability of failure estimate and monitor the convergence and stability of the solution (Melchers and Beck, 2018).

3.7. BRIDGE FRAGILITY ANALYSIS FRAMEWORK

The proposed framework establishes the fragility of bridges under flood hazard through three interconnected modules. Module 1 is responsible for predicting the future streamflow and long-term scour, while Module 2 generates the random samples used in the Monte Carlo simulation of the resistance and load effects. Module 3 computes the failure probability and established the bridge fragility. A layout of the framework is presented in Figure 3.3. As shown in the layout of Module 1, downscaled precipitation and temperature profiles associated with the selected climate scenarios are used to generate future streamflow profiles. This process relies on the deep neural network DN 1 trained using observed temperature and precipitation at various stations across the studied region, as well as the corresponding streamflow data at the bridge location. Note that the

application of Module 1 requires the availability of historical precipitation, temperature, and streamflow time-history data for the location of interest. The framework also assumes that downscaled climate prediction data is available for the considered bridge. Currently, this data is available for the Unites States through Brekke et al. (2013).

In Module 2, the resulting streamflow time-series associated with each climate scenario is integrated into Monte Carlo simulation, based on Equations 3.1 to 3.3, to generate samples from the random scour depth. Other random variables generated in Module 2 include the live load effects and soil properties. The developed OpenSees^{TM} FE model was initially employed to compute the load effects necessary for establishing the bridge fragility; however, given the large number of random variables, this process was proven to be computationally expensive. Accordingly, the FE model was used to generate training dataset for DN 2. This dataset covers the possible range of input parameters including the scour depth and soil properties, in addition to axial and lateral loads. DN2 is next used for computing the load effects (e.g., internal forces, stresses, and deformations) associated with each random sample and the corresponding value of the performance function. The capacity against axial, flexural, and shear failure modes is computed using AASHTO (2017) provisions.

The third module is responsible for computing the probability of failure and bridge fragility. Since the scour level can change along the bridge service life, the fragility established herein is a function of both the river discharge, as the hazard intensity parameter, and time. For a certain value of river discharge and service life, DN 2 is used to compute the corresponding load effects and failure probability. For a given climate scenario, the procedure is iterated to cover the full range of expected service life and hazard intensities resulting in a three-dimensional fragility surface. Finally, this process is repeated for all climate scenarios resulting in a mean fragility surface that assigns equal weights to the adopted climate scenarios (Weigel et al., 2010).

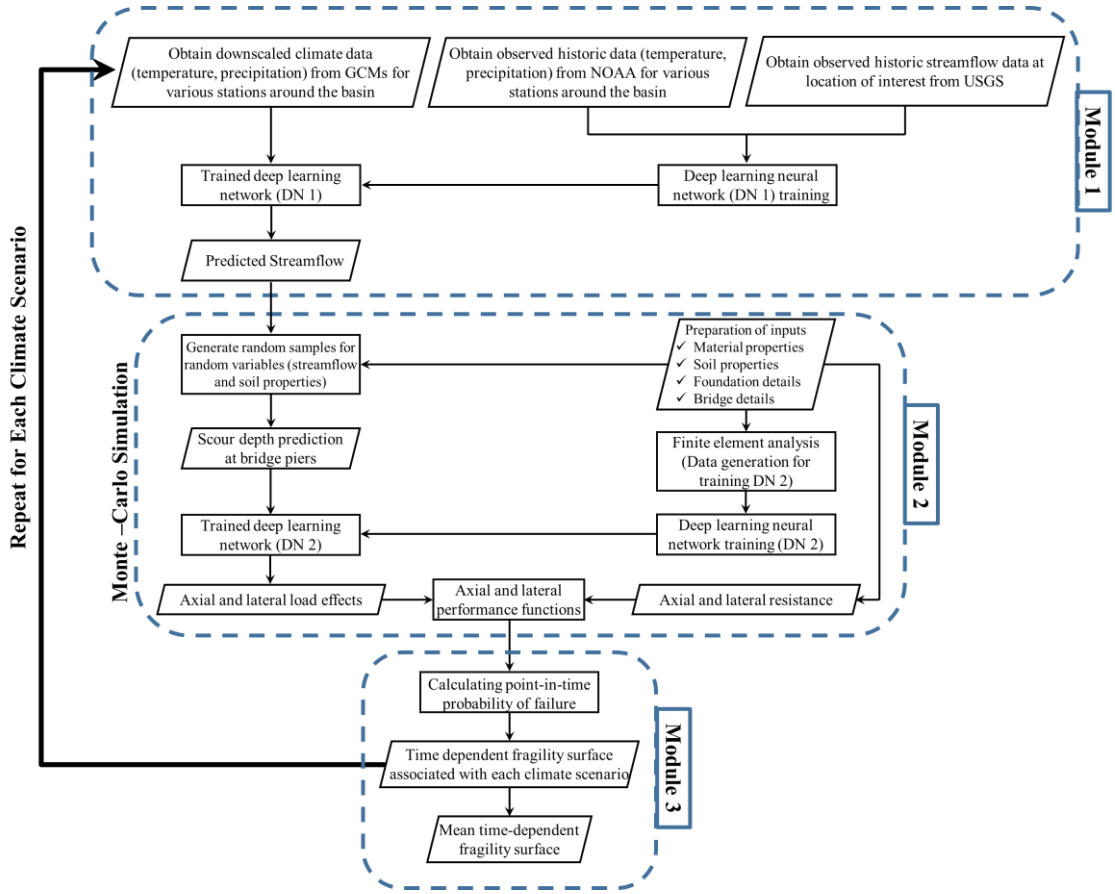

Figure 3.3. Proposed framework for establishing time-variant flood fragility

3.8. ILLUSTRATIVE EXAMPLE

The proposed framework is illustrated on the South Bound of I-35 Bridge over the Red River. This bridge, located on the Texas-Oklahoma border, serves a main transportation artery that links southern and northern states. The bridge is located on a major freight route with an average daily traffic of 19,800 vehicles per day (FHWA, 2016). The superstructure of the I-35 Bridge consists of ten 32.3 *m* long and 9.5 *m* wide spans, each of which has a 35 *cm* think reinforced concrete deck and five plate girders with two traffic lanes. The bridge substructure consists of 11 piers. The piers are 1.2 *m* wide and supported by two pile groups with nine 11.2 *m* long steel H-piles (HP 12x53 steel piles). Based on the original construction drawings, the riverbed level is considered to be 10 m below the deck. A layout of bridge pier with pile configuration is shown in

Figures 3.4a and b. In this chapter, it is assumed that the failure of a single pier constitutes the bridge failure event.

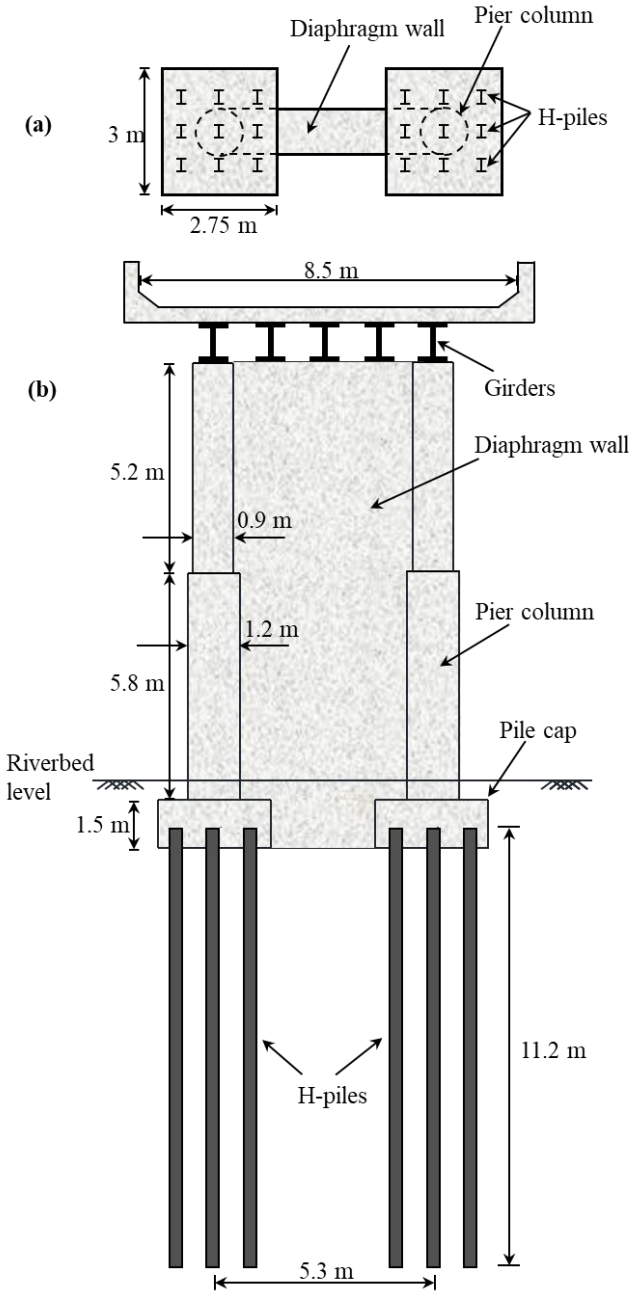

Figure 3.4. Layout of bridge pier with pile configuration (a) plan view of pile caps (b) side view of pier and H-piles

3.8.1. CLIMATE DATA ANALYSIS

Downscaled CMIP5 products are adopted from the public online database "*Downscaled CMIP3 and CMIP5 Climate and Hydrology Projections*" (Brekke et al., 2013). In particular, the MPI_ESM_LR, CCSM4, and MIROC5 global climate models downscaled using BCCA methods are employed. These models are selected based on the results of a detailed climate investigation performed by McPherson (2016) for the Red River basin. In their analysis, it was shown that the aforementioned GCMs are capable of providing reliable climate predictions for the region of interest. This has been addressed through comparing the historical records of the region with the model predictions.

In addition, the three radiative forcing cases RCP 2.6, RCP 4.5, and RCP 8.5, along with two different ensemble runs associated with each GCM and radiative forcing case are adopted. The combination of the three GCMs, three RCP cases, and two model ensemble runs provided eighteen individual climate datasets. These datasets consist of temperature and precipitation time-series of 140 years starting from the year 1960. For each combination of climate model and GHG emission scenario (e.g., CCSM4-RCP2.6) there are different ensemble runs, each with its own assumed initial conditions. Initial conditions lead to slight fluctuation in model projections. However, the effect of internal variability of the models (i.e., under different initial conditions) decreases in the long-term. This is especially true, when compared to other sources of uncertainties such as model uncertainty (i.e., different models) and scenario uncertainty (i.e., different future emissions pathways). The quantification of the effect of different uncertainties on climate prediction has been discussed in more depth in several studies including Hawkins and Sutton (2009) and Yip et al. (2011).

3.8.2. FLOOD PREDICTION USING DEEP LEARNING

A deep feed forward neural network is employed to perform the streamflow modeling. This deep network, referred to as DN 1 in this chapter, is created in TensorFlow™ environment and consists of 6 hidden layers. It was found that using 2048, 1024, 512, 256, 128, 64 neurons in the hidden layers 1 to 6, respectively, provides streamflow prediction with adequate accuracy. Adam optimizer (Kingma and Ba, 2014) is employed to establish the optimum weights $w_{n,n}^{(m)}$ and bias $b_{n,n}^{(m)}$ values that minimize the mean squared error (MSE) of the predicted data with respect to the target output.

Time-series of observed temperature and precipitation profiles of 30 weather stations across the Red River basin for the time period of 2000 to 2015 are extracted from the National Oceanic and Atmospheric Administration (NOAA, 2018) database. In addition, time-series of the observed streamflow data associated with the same time period (i.e., 2000 to 2015) is extracted from the United State Geological Survey (USGS) station on the Red River near Gainesville, TX (USGS ID: 07316000) (USGS, 2018). This station is located 300 *m* upstream of the investigated bridge. Selection of the stations was based on the following criteria (McPherson, 2016) (a) data for the modeling period must be available, (b) each station should at least have a drainage areas containing eight grid cells, and (c) if more than one station is located within the same 1/8°×1/8° grid cell, the station with larger drainage area should be chosen. The second and third criteria are selected to maintain compatibility with the adopted downscaled climate data which is provided in 1/8° resolution. Figure 3.5 depicts the map of the Red River basin, selected weather stations, and location of the investigated bridge. The observed precipitation, temperature, and corresponding streamflow datasets are used for training and testing the accuracy of DN 1. In this process, the precipitation and temperature profiles are used as the input parameters while the corresponding observed streamflow is considered the target output. Eighty percent of the observed dataset (i.e., 4,675 days) is randomly selected and allocated for training the model (i.e., the training dataset)

and the remaining 20% (i.e., 1,169 days) is used to evaluate the accuracy of the model (i.e., testing dataset). A common practice is to ensure that both the training and testing datasets are representatives of the underlying problem (Bickel et al., 2009). This can be achieved by comparing the statistical properties of the selected database to those of the available historical streamflow record for the investigated location. The daily coefficient of determination (R2) is used to evaluate the trained model as

$$R^2 = 1 - \frac{\sum(Q_o - Q_M)^2}{\sum(Q_o - \overline{Q}_o)^2} \tag{3.15}$$

where Q_o is observed daily streamflow, Q_M is the predicted daily streamflow using DN1. It should be noted that R^2 values greater than 0.75 can be considered acceptable for large basins such as Red River (Croke et al., 2005).

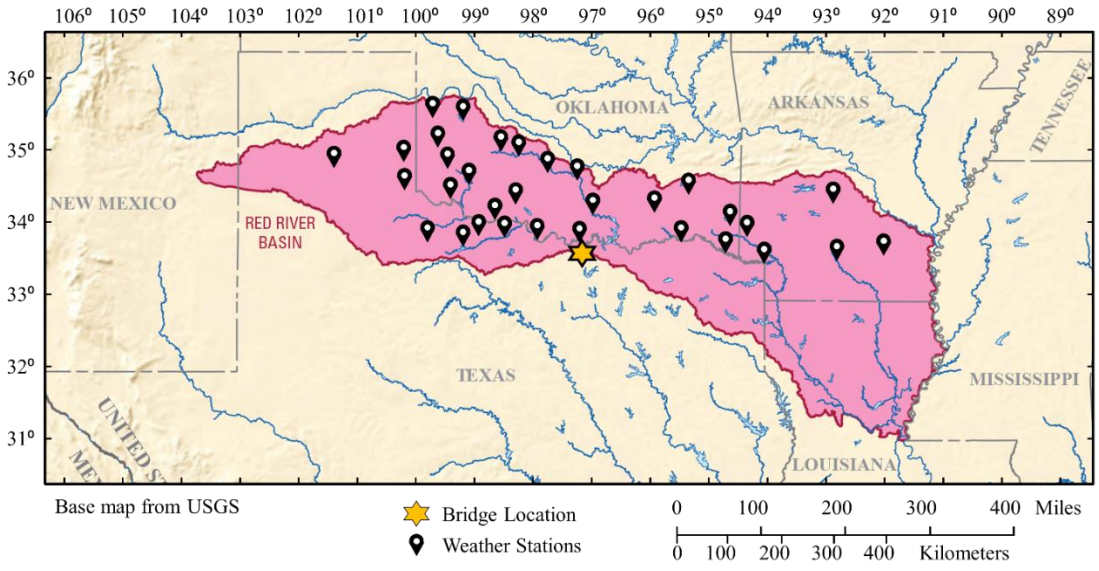

Figure 3.5. The Red River basin, investigated bridge location, and the considered weather stations

Figure 3.6 shows a comparison between the predicted and observed streamflow of the testing dataset. As shown, a reasonable agreement between the observed and predicted data is achieved. The evaluation of testing set indicates a R^2 value of 0.9116 and mean square error of 1.8452e-4.

More importantly, the trained network can accurately predict the high discharge values representing flood events.

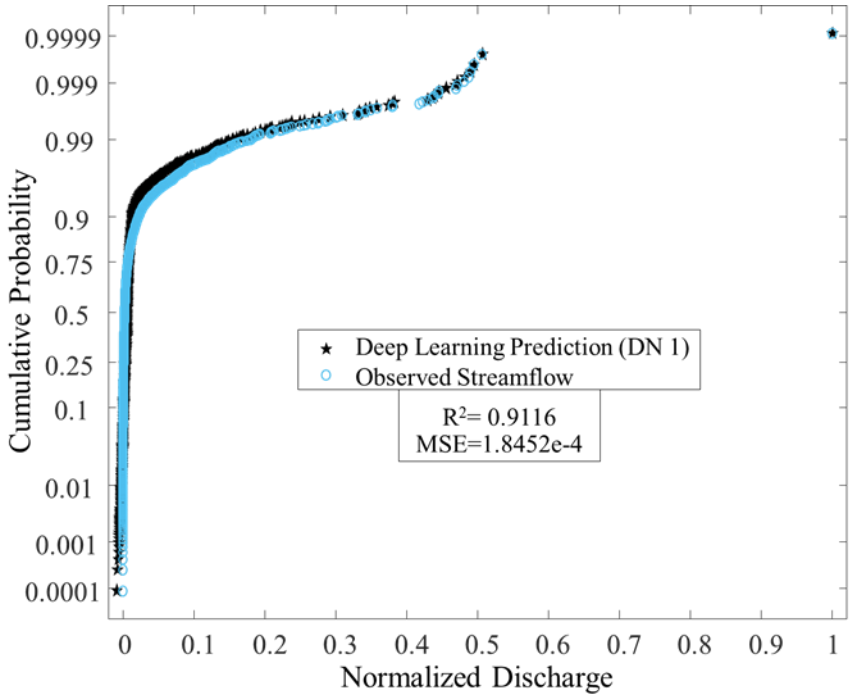

Figure 3.6. Comparison between the predicted versus the observed streamflow of the testing dataset

After the calibration process, the downscaled temperature and precipitation datasets associated with the adopted climate scenarios and corresponding to each of the 30 weather stations across the basin are extracted from the climate prediction database (Brekke et al., 2013). These datasets are then fed to the trained DN 1 to generate streamflow time-histories associated with each climate scenario and ensemble run for the period of 1960 to 2100. As an example, Figure 3.7 shows the generated streamflow profile associated with model CCSM4 with RCP 4.5. To assess the capability of this streamflow prediction method, the predicted river discharge is compared to the prediction results of the detailed hydrologic modeling conducted by McPherson (2016) for the bridge location. Figure 3.8 compares the probability plots of the streamflow obtained using the adopted deep learning approach and the corresponding results reported in McPherson (2016). A reasonable agreement can be seen between both predictions. The small variation between the two

profiles can be attributed to the different downscaling method and initial conditions adopted in McPherson (2016). Note that the trained DN1 is well generalized and is able to predict results outside the training dataset that has a maximum discharge of 5200 m^3/s.

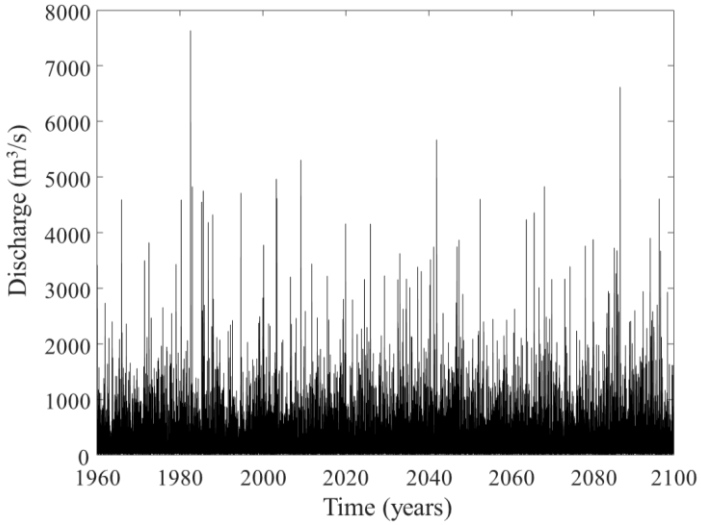

Figure 3.7. Streamflow time-series associated with CCSM4 model and RCP 4.5 generated using DN1

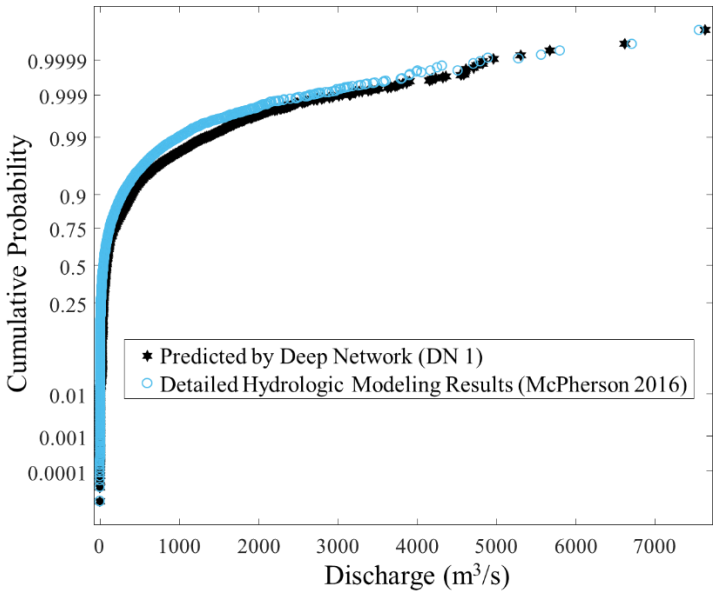

Figure 3.8. Simulated river discharge associated with CCSM4 model and RCP 4.5 using DN1 versus detailed streamflow modeling by McPherson (2016)

Figure 3.9 shows the randomly generated profiles of the long-term scour for all climate scenarios. The scour depth profiles are obtained based on Equations 3.1 to 3.3. The probability density

function (PDF) of the scour depths at the years 2000, 2040, and 2080 are also presented. This figure highlights the variability associated with the scour prediction especially when future climate scenarios are considered.

3.8.3. LONG-TERM CORROSION PREDICTION

The long-term corrosion effects are considered using Equation 3.5. The results of investigations conducted by Decker et al. (2008) on steel H-piles suggest that in moderate environmental condition, *k* and *n* can be assumed as 59 and 0.67, respectively. In addition, Ahammed and Melchers (1997) recommended that these constants follow a normal distribution with coefficient of variation (COV) of 0.56 and 0.26 for k and n parameters, respectively. The thickness loss due to corrosion is estimated given the exposure time (*t*) and the randomly generated *k* and *n* constants. The cross-sectional properties of the pile (e.g., thickness, area, and moment of inertia) are recalculated with respect to the estimated losses for each random sample. The updated cross-sectional properties are then used to quantify the effect of material deterioration on the predicted capacity. These results are then used in the performance functions to calculate failure probabilities at different points along the service life.

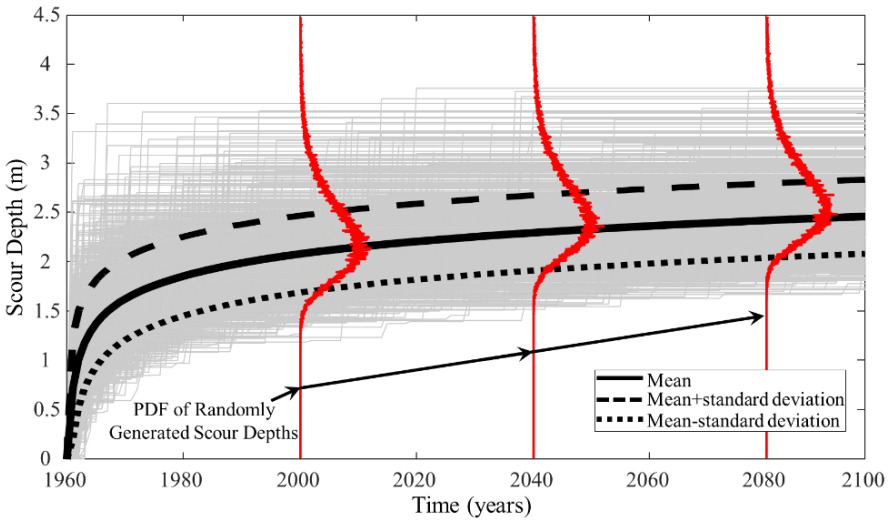

Figure 3.9. Randomly generated long-term scour depth profiles based on all climate scenarios

3.8.4. PILE GROUP ANALYSIS USING FE AND DEEP LEARNING

The developed FE model is employed to produce the required data for training the deep network (i.e., DN 2) used to quantify the foundation performance under lateral and axial loads. This network is used in place of the iterative execution of the FE model to accelerate the probabilistic simulation process. The pile group is modeled as a single pile discretized into 113 beam-column elements. Nonlinear pile nodes, slave nodes, modified *p-y*, and *t-z* springs are distributed along the depth of the simulated pile with 0.1 *m* spacing. The *p-y* curves are modified by applying a resistance reduction factors of 0.365 accounting for the closely spaced group effects in the lateral direction (Dunnavant and O' Neil, 1986).

The performance of the OpenSees™ model is benchmarked against the results of Group Software (Resse et al., 2016) which implements soil resistance curves and pile-soil-pile interaction effects to analyze pile groups under lateral and axial loadings. A comparison between the lateral displacements, bending moments, and shear forces generated by OpenSees™ and Group™ are presented in Figure 3.10. The presented Group ™ results show the mean of 9 responses associated with all the piles within the group.

The OpenSees™ model is then used to generate a training dataset for the deep learning network DN 2. Full factorial experimental design (Dieter, 2000) is used to create the pool of data used to run the OpenSees™ model; however, other experimental design approaches can be also used for more complex finite element models. A set of uniformly distributed variables including scour depths, lateral loads, axial loads, and angle of frictions are used to generate the training dataset. The values of these variables are selected to cover the possible range that may occur in the fragility analysis. Scour depths ranging from 0 to 5.0 *m*, lateral loads ranging from 20 to 200 *kN*, angle of friction ranging from 29 to 40 degrees, and axial loads ranging between 1200 and 4000 kN are used to generate a total of 40,000 different combinations of input and output data points.

A MATLAB® (MathWorks, 2018) script is developed to automatically define the combinations of input parameters, execute the FE analysis, and record the responses of the pile with respect to each input combination. Lateral and axial displacements, shear forces, bending moments, and axial forces along the depth of the simulated pile are recorded and used for training DN 2.

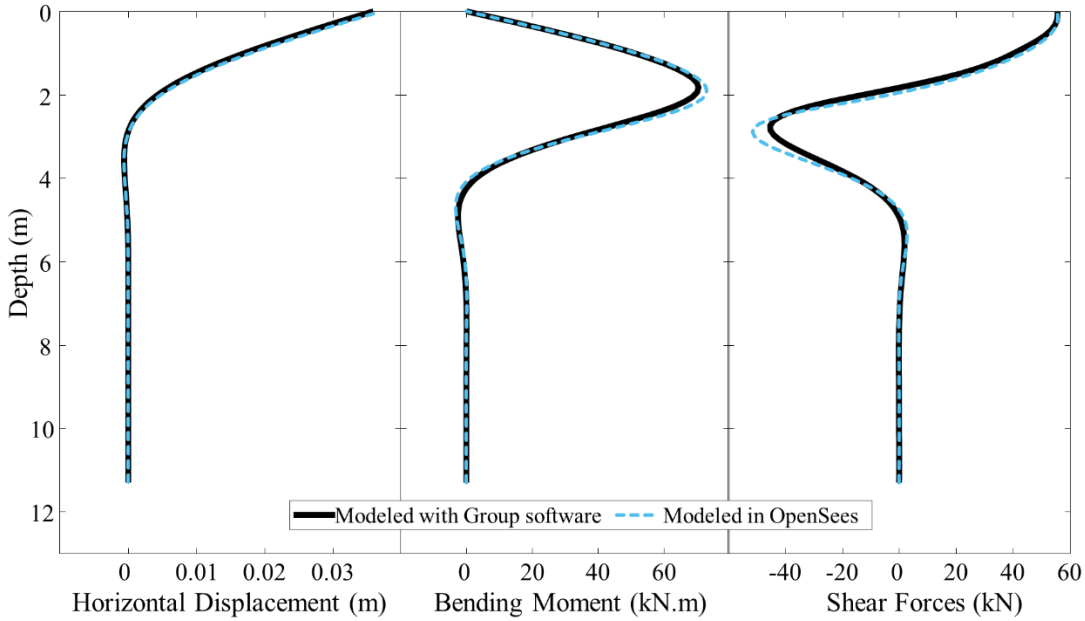

Figure 3.10. Generated lateral displacement, bending moment and shear forces based on OpenSees™ and Group™ software

DN 2 is next employed to predict the group pile response under the applied loads and scour deterioration. A deep network consisting of four hidden layers with 1024, 512, 256, and 128 neurons was able to provide highly accurate response predictions. An optimization procedure similar to the one adopted in DN 1 is used to establish the optimum weights and bias values. The scour depth, lateral load, axial load, and angle of friction are defined as the input parameters. The maximum internal forces, in addition to horizontal and vertical displacements represent the target output of DN 2. Eighty and 20% of the generated FE results are respectively used for training and testing the network. Figure 3.11 compares the deep learning results to their finite element counterparts. The coefficient of determination (R^2) and mean squared error (MSE) associated with each of the network output parameters are also presented in the figure. As shown, DN 2 is

capable of predicting the structural responses under the applied input parameters with high accuracy. In addition, the high accuracy of the trained DN2 highlights the fact that the response of the modeled pile system could also be simulated using other types of surrogate modeling techniques such as binary decision trees, regular neural networks, and regression models. Application of such models in simulating pile group behavior is also highlighted in several research articles such as Chan and Low (2012), Balomenos and Padgett (2018), and Singh et al. (2019). Among these techniques, surrogate models with interpretable model parameters such as logistic regression (Hosmer et al., 2013) and random forest regression (Liaw and Wiener, 2002) can provide useful information regarding the relationship and interdependencies between input parameters. This information can be particularly helpful in infrastructure management and risk mitigation decision making. It should be noted that the framework presented herein can be easily modified to accommodate other surrogate models for simulating the pile response function.

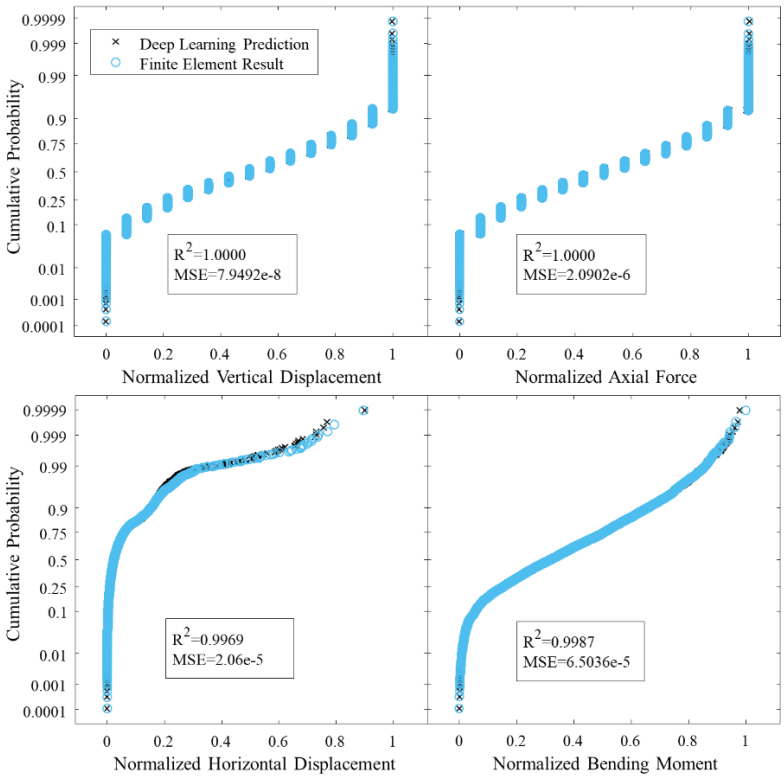

Figure 3.11. Displacements and internal forces generated using DN2 versus finite element results of the testing dataset

3.8.5. BRIDGE FLOOD FRAGILITY

The proposed bridge fragility surface provides the failure probability with respect to river discharge and service life. Generated scour depth profiles, in addition to dead and live loads are used to compute the failure probability of the bridge under different river discharge values. Lateral load effects encountered during floods are computed for different discharge values using Equation 3.6. Analysis of river discharge resulting from climate modelling and streamflow prediction revealed that a maximum discharge of 9,274 m^3/s can be expected at the bridge location; accordingly, the proposed bridge fragility surface covers discharge values up to 10,000 m^3/s. The live load acting on the pile group is assumed to follow a normal distribution with a COV of 0.18 (Wang, 2010). The angle of friction (ϕ) is assumed to follow a normal distribution with mean and COV of 35 and 0.06 (Kadar and Nagy, 2017), respectively.

Monte Carlo simulation with 10,000 samples corresponding to each climate dataset is implemented to compute the failure probability given the discharge and service life considering four limit states. This results in a total of 180,000 samples for the 18 climate datasets; however, more samples may be used if a finer resolution of the failure probability at low discharge volumes is required. The shear and combined axial-flexural failure limit states are given by Equations 3.10 and 3.11 in accordance with AASHTO (2017) recommendations. The limit states consider uncertainty associated with material properties (i.e., yield strength and modulus of elasticity) and resistance prediction models (i.e., shear, moment, and axial capacities). Allowable lateral displacement is assumed to follow a lognormal distribution with mean of 25 mm and COV of 0.2 (Haldar and Basu, 2014). An Axial displacement limit is defined to restrict the angular distortion (A_d) of the piles. This upper bound is considered to follow a lognormal distribution with mean and COV equal to 0.004 and 0.2, respectively (Hannigan et al., 2016). Descriptors of the considered random variables and their probabilistic distributions are presented in Table 3.1. Note that in this chapter, the considered random variables are assumed uncorrelated. However, the

proposed framework can easily accommodate other case studies with correlated random variables. Further information regarding the generation of correlated random samples can be found in Ang and Tang (2007) and Li et al. (2013).

Given the service life of the bridge, 10,000 samples representing the probabilistic distributions of the scour depth are extracted from the long-term scour prediction. These samples are used in conjunction with the random samples from the soil properties and external loads to compute the internal forces and deformations under a given discharge value by means of deep learning network DN 2.

This process is repeated for each combination of service life and river discharge to establish the fragility surface. The resulting three-dimensional fragility surface is depicted in Figure 3.12. As shown, the probability of failure increases in conjunction with both the service life and discharge values. The increase in failure probability for a given discharge value is due to scour accumulation and corrosion deterioration along the service life. The increase in the failure probability values at a given time can be attributed to the increase in applied lateral loads and moments due to more aggressive floods. Figure 3.13 a, and b depict, respectively, the two-dimensional fragility curves with respect to the service life and river discharge. As shown, due to the combined effects of corrosion and scour, the probability of failure corresponding to a given hazard intensity (i.e., discharge values) significantly varies during the service life.

Table 3.1. Properties of deterministic parameters and descriptors of the random variables

Parameter	Notation	Distribution	Mean Value	Coefficient of Variation	Reference
Scour modeling uncertainty factor	λ_1	Normal	0.44	0.79	Johnson et al. (2015)
Nose shape factor	K_1	Deterministic	1.1	-	Arneson et al. (2015)
Attack angle factor	K_2	Deterministic	1.0	-	
Bed condition correction factor	K_3	Deterministic	1.1	-	
Live load	LL	Normal	HL-93	0.18	AASHTO (2017); Wang (2010)
Angle of friction	ϕ	Normal	35	0.06	Kadar and Nagy (2017)
Lateral displacement limit	$\Delta_{L\_critical}$	Lognormal	25 (mm)	0.20	Haldar and Basu (2014)
Angular distortion limit	A_d	Lognormal	0.004	0.20	Hannigan et al. (2016)
Corrosion multiplying constant	k	Normal	59	0.56	Decker et al. (2008); Ahmmad and Melchers (1997)
Corrosion exponential constant	n	Normal	0.67	0.26	
Shear resistance uncertainty factor	λ_2	Lognormal	1.05	0.12	Galambos (2004)
Combined axial-flexural uncertainty factor	λ_3	Lognormal	1.01	0.04	Galambos (2004)
Combined axial-flexural uncertainty factor	λ_4	Lognormal	1.005	0.0093	Galambos (2004)
Yield Stress	F_y	Lognormal	350 (MPa)	0.07	JCSS (2001)
Modulus of elasticity	E	Lognormal	200 (GPa)	0.03	JCSS (2001)

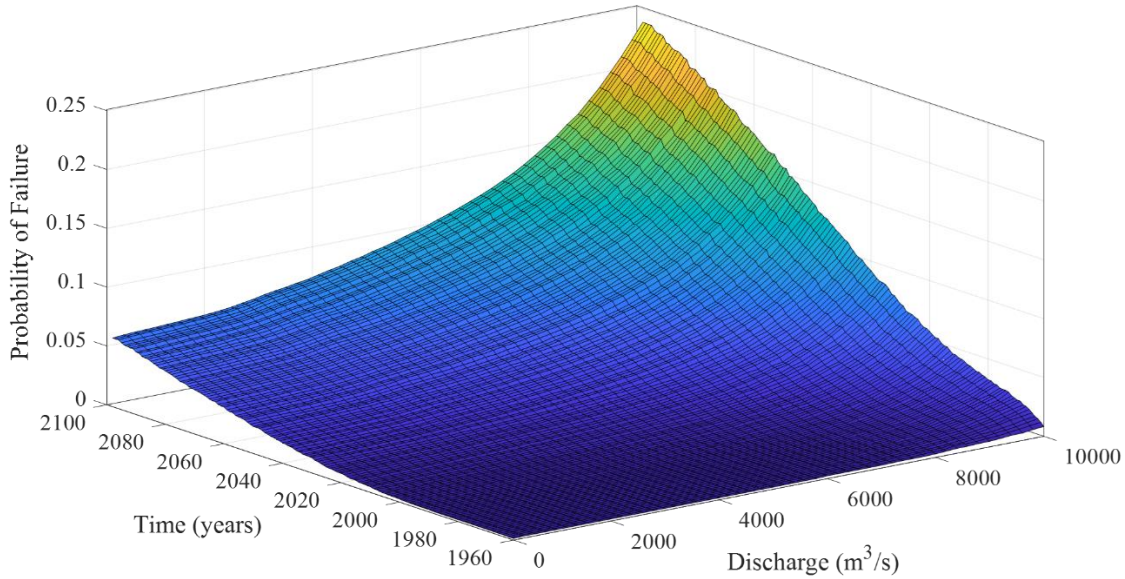

Figure 3.12. Time-variant fragility surface associated with the mean of adopted climate datasets

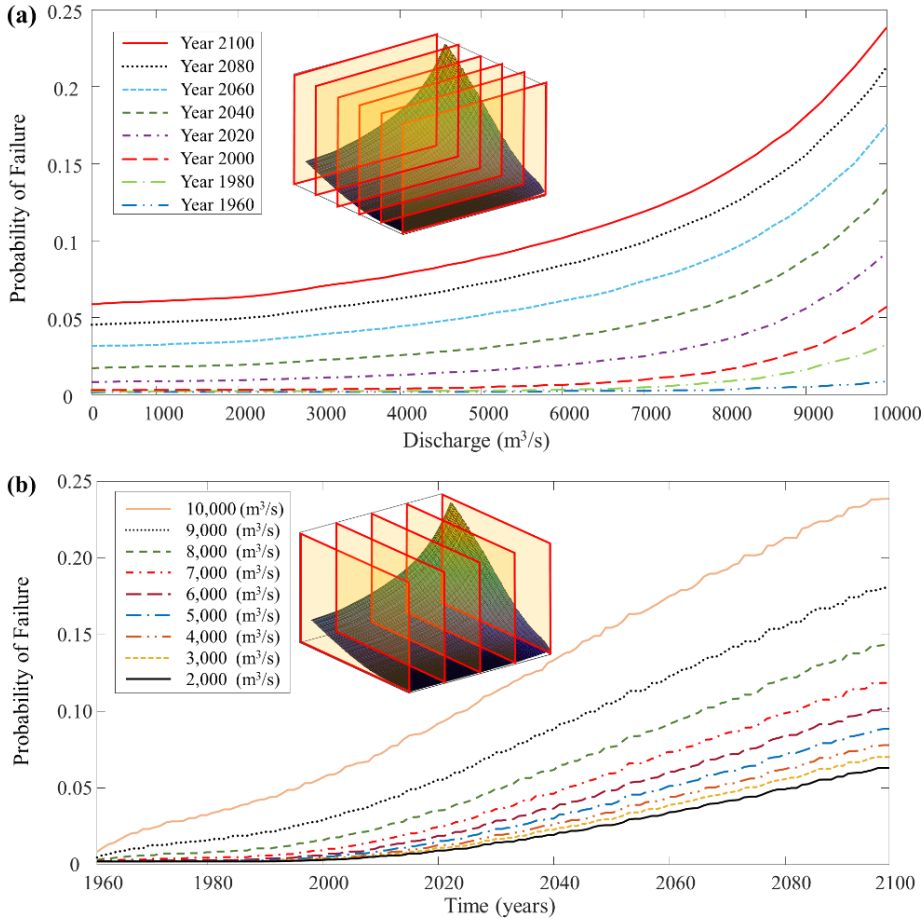

Figure 3.13. Variation in the flood fragility with respect to (a) river discharge and (b) service life

3.9. CONCLUSIONS

This chapter presented a probabilistic framework for fragility assessment of bridges under flood and flood induced scour considering climate change. Downscaled precipitation and temperature climate datasets, adopted from CMIP5 archive for the location of interest, are used to predict the river discharge and scour depth. A deep feed forward neural network (i.e., DN 1), trained by historic records at the bridge location, was adopted to predict the discharge. An OpenSees^{TM} FE model generated the required training data for a second deep neural network (i.e, DN 2) to compute the internal forces and displacements of the foundations given the service life and river discharge. The annual failure probability of the bridge under flood-induced loads was calculated and used to develop the time-variant fragility surfaces of the bridge. The following conclusions are drawn:

- The proposed approach is capable of establishing the bridge flood fragility as a function of the service life and river discharge. This fragility surface can help bridge officials in making informed decisions related to management activities (e.g., retrofit) aiming at reducing the failure probability under future flood hazard. In addition, it provides a quantitative measure that can assist in making bridge closure decisions during flood events.
- The employed neural network (i.e., DN 1) is able to predict the streamflow, given the temperature and precipitation patterns, with a sufficient accuracy. This was highlighted by a daily coefficient of determination (R^2) of 0.9116 during the calibration phase. In addition, the streamflow prediction results provided a good agreement with those published in literature based on detailed hydrological analysis.
- The generated fragility surface shows that scour propagation along the service life can significantly reduce the bridge reliability against future floods. This highlights the importance of applying appropriate scour countermeasures to reduce the failure probability.
- The employed surrogate deep learning networks were fully trained in approximately 30 hours using 40,000 FE executions conducted on a desktop computer with 16 GB memory

and a dual core i7-7700 @ 3.6 GHz Intel processor. Given that a total of 70,000,000 simulations was required for developing the fragility surface for each climate scenario, with an average FE model analysis time of three seconds, significant reduction in the computational time was achieved through the proposed framework.

CHAPTER IV

PERFORMANCE ASSESSMENT OF PRESTRESSED CONCRETE BRIDGE GIRDERS USING FIBER OPTIC SENSORS AND ARTIFICIAL NEURAL NETWORKS

4.1. OVERVIEW

Structural health monitoring (SHM) activities are essential for achieving a realistic characterization of bridge structural performance levels throughout the service life. These activities can help detect structural damage before the potential occurrence of component- or system-level structural failures. In addition to their application at discrete times, SHM systems can also be installed to provide long-term accurate and reliable data continuously throughout the entire service life of a bridge. Owing to their superior accuracy and long-term durability compared to traditional strain gages, fiber optic sensors are ideal in extracting accurate real-time strain and temperature data of bridge components. This chapter presents a statistical damage detection and localization approach to evaluate the performance of prestressed concrete bridge girders using fiber Bragg grating (FBG) sensors. The presented approach employs Artificial Neural Networks (ANNs) to establish a relationship between the strain profiles recorded at different sensor locations across the investigated girder. The approach is capable of detecting the presence of damage at the sensor location without requiring detailed loading information; accordingly, it can be suitable for long-term monitoring activities under normal traffic loads. The work in this chapter is based on the published papers Khandel et al. (2019c; and 2020).

4.2. BACKGROUND

Due to various deterioration processes (e.g., corrosion and fatigue), more than 10% of bridges in the United States are categorized as structurally deficient (FHWA, 2016). Among those, approximately 53% are multi-beam/girder bridges. A large number of newly constructed bridges in the U.S. use prestressed concrete. In order to facilitate informed repair and replacement decisions when these structures approach the end of their service life, they could be instrumented, during construction, with sensors that can provide accurate and reliable data throughout the entire service life. In this context, fiber Bragg grating (FBG) sensors can provide outstanding long-term stability and highly reliable strain and temperature measurements with minimal processing effort (Lin et al., 2004). These sensors, when embedded into the prestressed concrete (PSC) components during construction, can provide accurate real-time strain and temperature measurements at any time during the service life. The measurements obtained from these sensors can be used to assess the initial strain levels from the prestress forces and to develop a baseline strain profile under normal traffic loads that can help in evaluating the long-term condition of the bridge component. Statistical damage detection techniques can be used to achieve this goal by identifying the deviation of a future state of the system from the baseline state (Gres et al., 2017).

The introduction of the fiber FBG sensors by Morey et al. (1990) opened the door for applying fiber optic sensors in strain-based performance monitoring activities. Dunphy et al. (1990) demonstrated the feasibility of using FBG sensors in monitoring the response of layered graphite/epoxy composite components. Prohaska et al. (1993) employed FBG sensors to measure strains in a large-scale reinforced concrete beam under pure bending. Research on the application of fiber optic sensors in health monitoring of structures covers other applications including monitoring long-term prestress losses (e.g., Maaskant et al., 1997), quantifying the short- and long-term changes in the response of concrete structures (e.g., Idriss et al., 1998; Inaudi and Vurpillot, 1999; Lin et al., 2004), studying structural vibration characteristics (Kang et al., 2007;

Chung and Kang 2008), and detecting concrete cracking. FBG sensors have also been used to quantify prestress losses (Butler et al., 2016; Abdel-Jaber and Glisic 2019) and long-term effects due to creep and shrinkage (Webb et al., 2017).

Fiber optic sensors have also been employed for damage detection in PSC components. Zhang et al. (2006) employed fiber optic sensors to identify the damage in externally prestressed concrete T-beams by comparing their recorded response to analytically derived limit states. Uva et al. (2014) proposed a method to identify damage in prestressed concrete viaducts based on expected theoretical strains and actual strain recorded with FBG sensors. Abdel-Jaber and Glisic (2015) used long-gauge FBG sensors to detect pre-release cracks and monitor prestressing force transfer in PSC girders. Their approach focused on damage due to crack opening during the pre-release phase. Waeytens et al. (2016) applied model updating techniques for damage detection in a post-tensioned concrete beam under static loading using distributed fiber optic sensors. Their method, which requires detailed loading information, updates physical parameters (e.g., modulus of elasticity) of different subdomains in a finite element model to match the experimental results. Anastasopoulos et al. (2018) used FBG sensors to develop strain mode shapes and identify structural damage based on the change in top-to-bottom strain ratio in a prestressed concrete roof girder. However, their approach is more suitable for isolated individual structural components.

Statistical damage detection can be performed using supervised or unsupervised methods. The former method requires damage-sensitive features (DSFs) from both damaged and undamaged states of the structure, while unsupervised methods detect the damage using information from a baseline undamaged structural state (Santos et al., 2013). Due to the fact that obtaining DSFs from the damaged state of the structures is challenging, common statistical damage detection practices often rely on unsupervised methods (Jin and Jung 2018). Several methodologies are available for damage detection and localization in bridges using unsupervised statistical damage detection (e.g., Mattson and Pandit, 2006; Reiff et al., 2016; Weinstein et al., 2018). However,

these methods are often based on small-scale laboratory tests on idealized structures or may require comprehensive finite element analysis and detailed loading information for proper damage detection. In addition, less focus has been placed on the application of unsupervised statistical damage identification in PSC bridge components using fiber optic sensing systems. In particular, an approach capable of assessing damage in PSC bridge components under random loading is required.

This chapter presents a framework for damage detection and localization in newly constructed prestressed concrete bridge girders using fiber optic sensing and Artificial Neural Networks (ANNs). The presented approach uses an inferred relationship between the strain profiles at different sensors distributed across the girder to detect damage under variable amplitude loading. The presented damage detection and localization approach does not require applied loads as input parameter or detailed finite element analysis of the investigated component. In addition, it has higher accuracy compared to other monitoring techniques relying on foil-type strain gages. The approach is illustrated using experimental data obtained from flexural testing of a large-scale prestressed concrete girder instrumented with FBG sensors. The strain readings obtained during an initial random loading stage are used to train ANNs and define acceptable prediction error bounds to judge whether or not the girder is damaged. The trained ANNs are then used to predict strain profiles at target sensors for other randomly generated variable amplitude and monotonic load tests. Finally, the error between the predicted strains and experimental data is compared to acceptable error bounds to identify and localize the damage in the girder during subsequent load tests.

4.3. DAMAGE DETECTION AND LOCALIZATION PROCEDURE

4.3.1. ARTIFICIAL NEURAL NETWORKS (ANNS)

Artificial Neural Networks (ANNs) are algorithms designed to recognize numerical

patterns. Several types of neural networks, such as feedforward, radial basis function, convolutional, recurrent, and modular neural networks, have been introduced to assist in solving complex computational problems in various research areas (Mehta, 2019). Owing to their superior prediction accuracy and computational efficiency, feed forward ANNs, which consist of one or more hidden layers, have been one of the most widely adopted network types (Montana, 1989). ANNs consist of input, output, and hidden layers. An input layer is responsible for introducing the input parameters (**X**) to the ANN. The Output layer is the last layer of neurons that streamlines the results matrix (**Y**), while g hidden layers ($h^{(1)}$ to $h^{(g)}$), each consisting of several neurons (e.g., $n_1^{(1)}$ to $n_{a1}^{(1)}$ for hidden layer one and, $n_1^{(g)}$ to $n_{ag}^{(g)}$ for hidden layer g), are responsible for converting the input units to nonlinear functions of linear combinations of weights (e.g., $w_{1,a2}^{(2)}$ for weights between neuron 1 of first hidden layer and neuron $a2$ of the second hidden layer) and bias values (e.g., $b_{a1,a2}^{(2)}$ for bias between neuron $a1$ of first hidden layer and neuron $a2$ of the second hidden layer) assigned to a given input parameter. A transfer function (f) will then determine the state of each hidden layer during the training as (Montana, 1989)

$$h^{(p)} = f\left[\mathbf{W}^{(p)}\mathbf{X} + \mathbf{B}^{(p)}\right] \quad \text{and} \quad p = 1 \text{ to } g \tag{4.1}$$

where $\mathbf{W}^{(p)}$ and $\mathbf{B}^{(p)}$ are the matrices of the weights and bias values associated with the transformation through neurons in hidden layer p, respectively. Comparing the ANN prediction to the target output, the assigned weights and bias values are optimized such that the prediction error is minimized.

Feedforward ANNs are known as networks with no closed-loops, meaning that data moves only in one direction from the input nodes, through the hidden nodes, and to the output nodes. Figure 4.1 shows a generalized layout of a multilayer feedforward ANN.

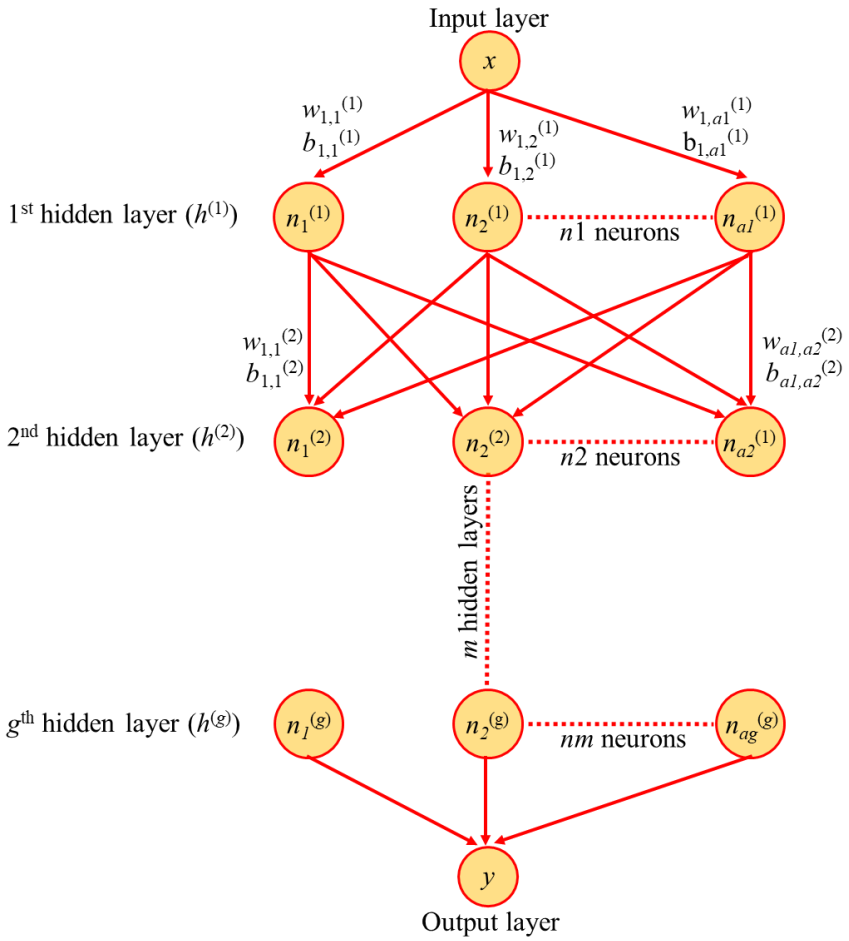

Figure 4.1. Generalized layout of multilayer feedforward ANNs

These networks often benefit from a backpropagation algorithm that calculates the gradient of the error with respect to the assigned weights and bias values for a given input. Levenberg-Marquardt (Levenberg, 1944; Marquardt, 1963) nonlinear least squares optimization algorithm is adopted in this chapter for ANN training. This method is well known for its high efficiency and fast convergence (Hagan and Menhaj, 1994).

4.3.2. DAMAGE DETECTION USING ANNS

The approach developed in this chapter employs ANNs to establish a relationship between the strains recorded under normal traffic loads by the FBG sensors embedded along the girder. After establishing this relationship, future strain responses recorded under normal traffic loads can be

used to identify whether or not the beam is damaged. The proposed framework is designed to identify the damage based only on the strain records without relying on information about the magnitude of applied loads. Several ANNs are trained and tested in order to account for modelling uncertainties associated with their prediction. The adopted criteria for defining each ANN is discussed in more detail later in this chapter. Each individual ANN is trained using a randomly selected sample of the training dataset. The relationship between the strain records of sensors can be different due to the dissimilar nonlinear fit that each ANN establishes. The strain records of all except one sensor (i.e., the target sensor) along the beam are used as the input of the ANNs to predict the strain in the target sensor. After training the ANNs, other available strain records collected during future monitoring, referred to as the set-aside dataset, are fed to the trained ANNs to predict the expected strains at the target sensor. Finally, damage is assessed by comparing the ANN predicted strain response to the actual response obtained by the FBG sensors. Figure 4.2 shows the layout of the proposed damage detection framework.

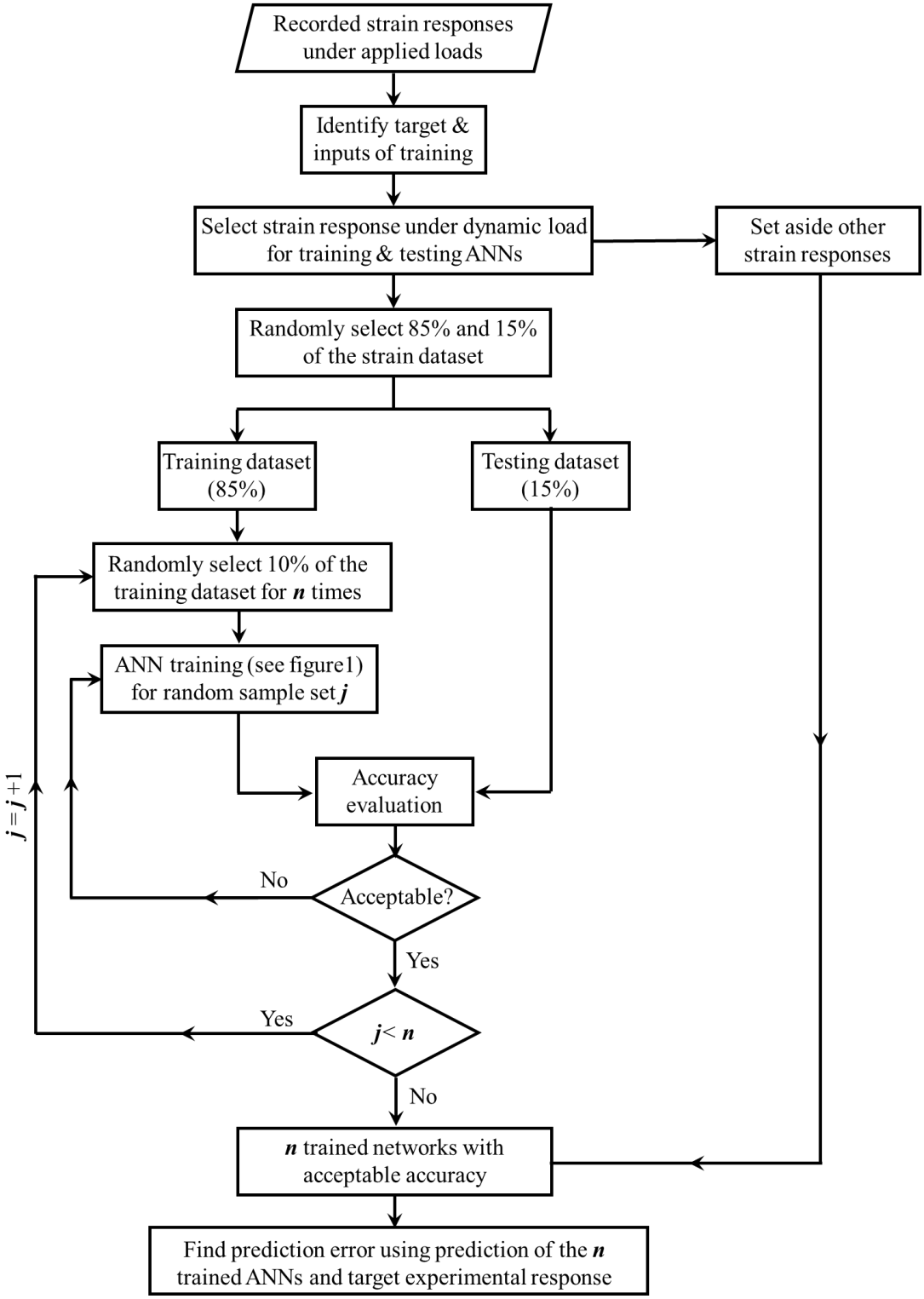

Figure 4.2. Layout of the proposed damage detection framework

To assess the damage occurrence, prediction error is used to compare the simulated strains against those recorded under next load applications. The prediction error associated with individual ANNs at different time instants is.

$$E(i,j) = \varepsilon_{ANN}(i,j) - \varepsilon_{\exp}(i) \tag{4.2}$$

where $E(i,j)$ is the error associated with j^{th} ANN at the i^{th} time instant, $\varepsilon_{exp}(i)$ is FBG strain record at target sensor associated with the i^{th} time instant, while $\varepsilon_{ANN}(i,j)$ is the strain predicted by the j^{th} ANN at the same time. n and m represent the total number of ANNs and strain data points, respectively. The mean prediction error ME is

$$ME = \frac{\sum_{j=1}^{n}\sum_{i=1}^{m} E(i,j)}{m \times n} \tag{4.3}$$

In addition, the mean lower and upper bounds of the strain prediction error associated with the trained ANNs at 95% confidence intervals are

$$E_{LB} = ME + \frac{\sum_{j=1}^{n} E_{2.5}(j)}{n} \tag{4.4}$$

$$E_{UB} = ME + \frac{\sum_{j=1}^{n} E_{97.5}(j)}{n} \tag{4.5}$$

where E_{LB} and E_{UB} are the lower and upper bounds of prediction error associated the testing dataset, respectively, $E_{2.5}(j)$ and $E_{97.5}(j)$ are the 2.5th and 97.5th percentiles of the prediction error associated with j^{th} trained neural network and testing dataset. A damage is detected if the mean prediction error under a specific loading condition falls outside the defined bounds, otherwise the beam is considered undamaged. Note that the defined bounds should be established for the

undamaged state of the structure. This is due to the fact that these bounds will be used as a baseline to compare the future behaviour of the girder and identify the potential presence of structural damage. In this chapter, these bounds are defined based on Weinstein et al. (2018).

Note that the proposed approach is designed to detect damage in newly constructed bridge girders. In such applications, the ANNs will be only trained once, during the undamaged (i.e., pre-cracking) state of the girders and after installing the girders in place. Although there is no need for continuous training of the ANNs, there is a need for regular analysis of strain records to assess the presence of damage in the monitored component. This process should to be conducted for each monitored girder. Due to the uncertainties associated with material properties, variation in sensor locations, and unforeseen construction conditions, girders with identical design specifications can have different relationship between the strain responses of embedded sensors. In addition, the approach can be also applied to existing bridge girders that are (a) in an undamaged state and (b) instrumented using any sensor type capable of providing continuous strain readings under variable amplitude loading at several locations along their length.

4.3.3. DAMAGE LOCALIZATION USING ANNS

To localize damage in PSC girders, the beam is divided into several regions. For each region, a configuration of ANN with unique selection of input and target sensors responsible for predicting damage is developed. The flowchart of the proposed damage localization approach is presented in Figure 4.3. Strain readings in the undamaged state are used to train the ANNs for different configuration corresponding to regions 1 to $\boldsymbol{l}$. Eighty-five percent and 15% of the strain records are randomly selected and defined as training and testing datasets. A number of ANNs (n) are next trained for each configuration corresponding to defined regions. Each of the n ANNs is then trained using a randomly selected 10% of the training dataset. This process is repeated for the

considered damage regions (i.e., ANN configuration 1 to ***l***). Finally, the prediction error corresponding to ANNs with different configurations is compared to localize the damage.

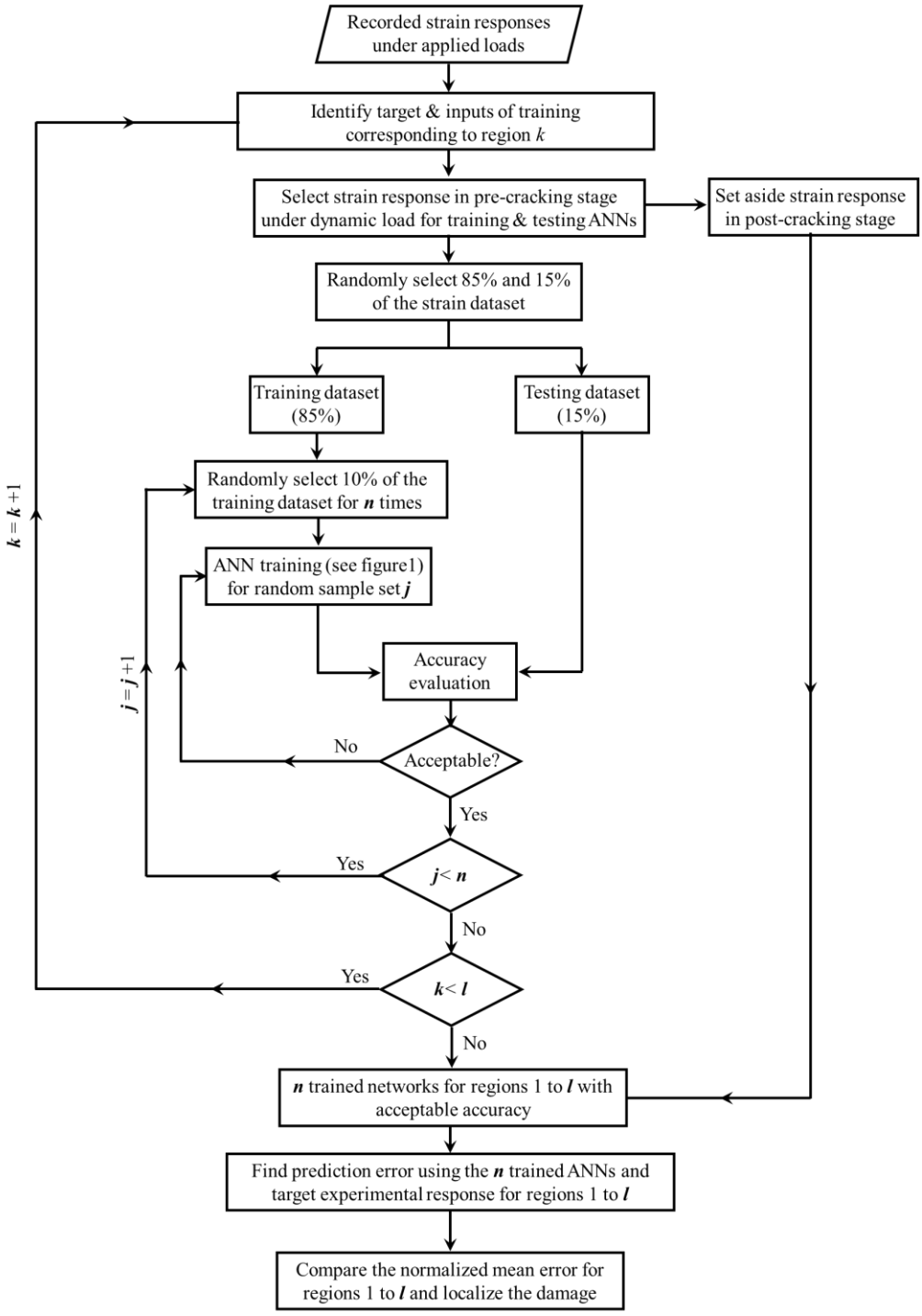

Figure 4.3. Layout of the proposed damage localization approach

A normalized mean error is defined to compare the prediction error in each region. This is essential since the recorded strains at target sensors and their associated errors may be in different ranges. Accordingly, the prediction error associated with the configured ANNs may not be directly comparable. In this chapter, the normalized error is computed as:

$$NME(k, j) = \frac{\sum_{i=1}^{m} \frac{\varepsilon_{ANN}(i, j, k) - \varepsilon_{\exp}(i, k)}{\varepsilon_{\exp}(i, k)}}{m} \tag{4.6}$$

where $NME(k,j)$ is the normalized mean error associated with prediction of the j^{th} ANN in configuration k, $\varepsilon_{exp}(i,k)$ is FBG strain record at the target sensor of ANN configuration k associated with the i^{th} time instant, and $\varepsilon_{ANN}(i,j,k)$ is the strain record at the target sensor of ANN configuration k predicted by the j^{th} ANN at time instant i..

4.4. ILLUSTRATIVE EXAMPLE

The proposed damage detection procedure is illustrated on an approximately ½ scale AASHTO Type II prestressed girder. The beam was instrumented during construction with FBG sensors, vibrating wire strain gages (VWSGs), and a mid-span displacement sensor.

4.4.1. SPECIMEN DESIGN

The cross section of the tested girder consisted of two 13.2 mm diameter (0.52 in.) low-relaxation prestressing strands with minimum ultimate strength of 1,860 MPa (270 ksi). The strands were tensioned to 75% of their specified tensile strength and placed 5 cm (2 in.) above the bottom fiber of the cross section. In addition, two No. 16 (#5) reinforcing bars were placed 5 cm (2 in.) below the top fiber of the cross section to counteract the concrete tensile stresses at time of prestress release. No. 10 (#3) Z-shaped bars were also placed transversely to resist shear stresses. Transverse shear reinforcement was designed to ensure flexural failure under a four-point-bending test. The beam was longitudinally symmetrical with respect to its mid-span. Figure 4.4

shows the geometry of the section, placement of reinforcement and prestressing strands, and spacing of shear reinforcement along one half of the beam. A self-consolidating concrete mixture was designed to achieve a compressive strength of 27.5 MPa (4,000 psi) and 55 MPa (8,000 psi) at 7 and 28 days, respectively. Figures 4.5 a and b show, respectively, an elevation of the beam reinforcement and concrete placement process during the girder construction in Donald G. Fears Structural Engineering Laboratory located at the University of Oklahoma.

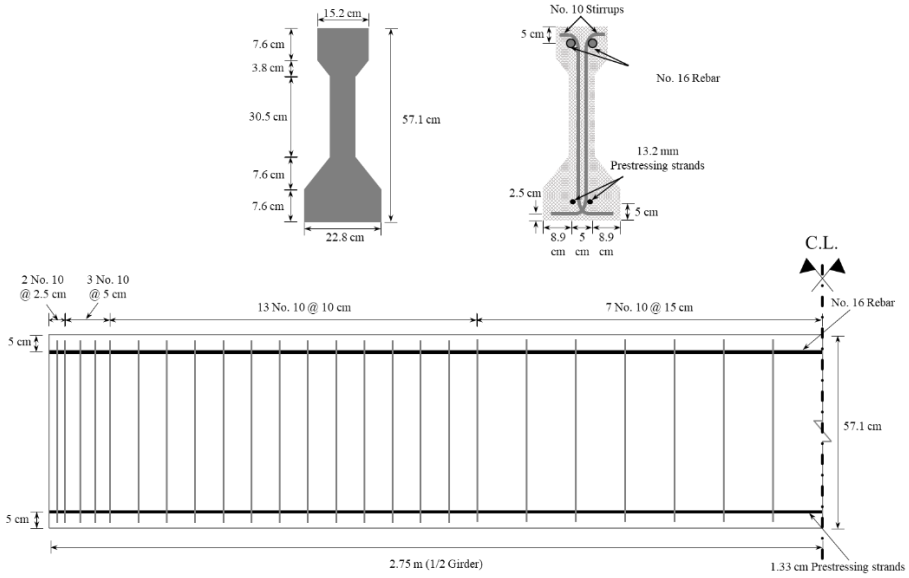

Figure 4.4. Geometry of the section and reinforcement details

Figure 4.5. View of the (a) beam reinforcement before casting and (b) beam during construction

4.4.2. TEMPERATURE, DEFLECTION AND STRAIN MONITORING USING FIBER BRAGG GRATING (FBG) SENSORS

Two fiber optic cables, each consisting of 15 FBGs, were placed along the girder at the prestressing strand level. Each cable was placed to position 15 sensors in one half of the girder. A third fiber optic cable containing two temperature sensors, each in one half of the beam, was also embedded in the girder. The instrumentation was symmetric with respect to the centerline of the girder. Figure 4.6 shows the layout of the strain and temperature sensors (FBGs) distributed along one half of the beam. Note that the girder was longitudinally symmetrical. Clustering the sensors near the supports aimed at capturing the behaviour of the end regions during and after prestress transfer.

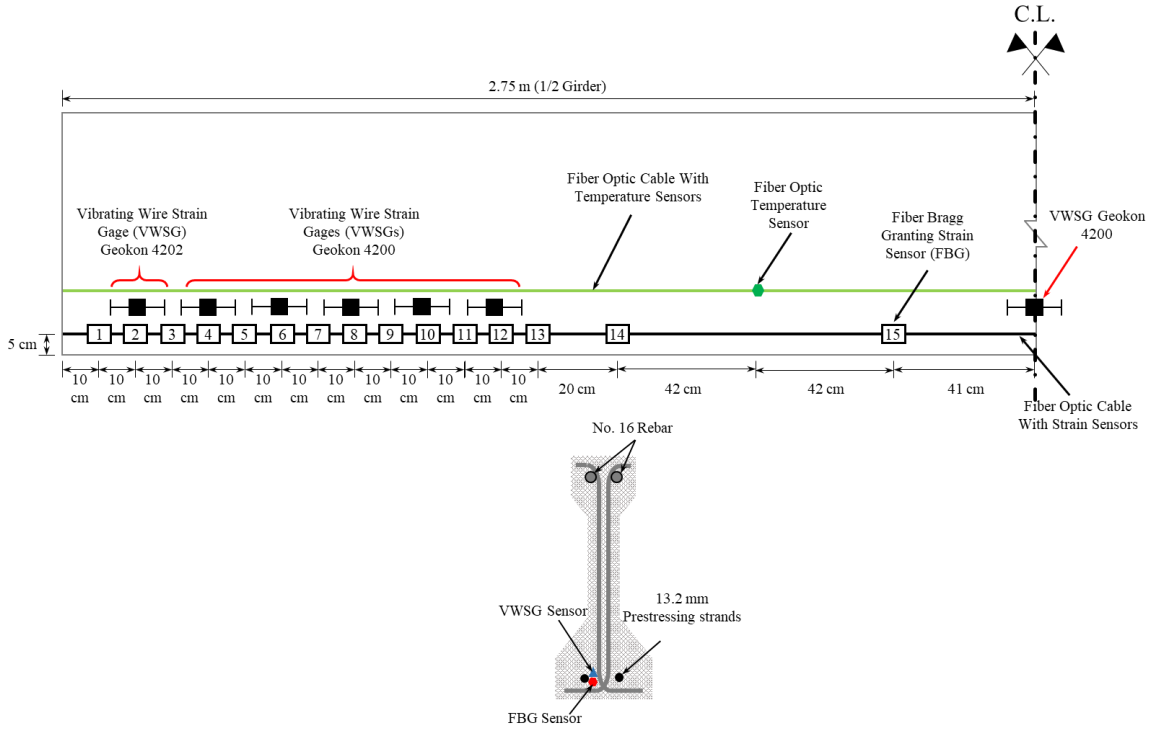

Figure 4.6. Layout of the FBGs and VWSGs distributed along one half of the beam

An interrogator featuring four channels and optimized for measuring static and dynamic measurements (FAZ Technology 2019) was used to provide a source signal (i.e., laser light) for

the fiber optic sensors and interpret the wavelength data under the applied loads. The recorded change in wavelength from the strain and temperature sensors at different time instants during testing were then used to calculate the change in temperature and strain. Equation 4.7 shows the relationship between the temperature sensor reading and actual temperature in ℃ (Faz Technology, 2019).

$$T_t = T_{S1}\left(\frac{\lambda T_t - \lambda T_{ref}}{\lambda T_{ref}}\right)^2 + T_{S2}\left(\frac{\lambda T_t - \lambda T_{ref}}{\lambda T_{ref}}\right) + T_{S3} \tag{4.7}$$

where T_t is the temperature in ℃ at time t, T_{S1}, T_{S2}, and T_{S3} are temperature calibration coefficients provided by the manufacturer. λT_t is the wavelength recorded by temperature sensor at time t during the experiment, and λT_{ref} is the reference wavelength for the temperature sensor provided by the manufacturer. The change in strain can be computed as (Faz Technology, 2019)

$$\Delta\varepsilon_t = \frac{\frac{\lambda_t - \lambda_{initial}}{\lambda_{initial}} - B\left(T_t - T_{initial}\right)}{A} \tag{4.8}$$

in which $\Delta\varepsilon_t$ is change in strain at time t with respect to initial strain value, $\lambda_{initial}$ and $T_{initial}$ are initial wavelength and temperature readings at the starting time of the test, and λ_t and T_t are wavelength and temperature reading at time t during testing. A and B are calibration constants provided by the manufacturer. The values of the calibration parameters provided by the manufacturer are presented in Table 4.1.

Table 4.1. Calibration parameters for temperature and strain sensors

Calibration Parameter	Temperature Sensor #1	Temperature Sensor #2	Strain Sensors
T_{S1}	-1,676,707.293078550 [℃]	140,364.36897385 [℃]	----
T_{S2}	54,069.9715208757 [℃]	53,482.2408014799 [℃]	----
T_{S3}	22.5024283936152 [℃]	22.4751371210772 [℃]	----
λT_{ref}	1,557.486 [nm]	1,537.725 [nm]	----
A	----	----	7.6362571E-07 [$\mu\varepsilon^{-1}$]
B	----	----	5.9684121E-06 [$℃^{-1}$]

4.4.3. VIBRATING WIRE STRAIN GAGES (VWSGS)

Thirteen VWSGs were also embedded in the girder during construction with six gages at each end and one at mid-span as shown in Figure 4.6. Two different models of VWSGs were used, Geokon 4200 and 4202 (Geokon, 2019) with 152 mm (6 in.) and 51 mm (2 in.) gage lengths, respectively. One Geokon 4202 strain gage with ±0.4 $\mu\varepsilon$ measurement resolution and six Geokon 4200 gages with ±1 $\mu\varepsilon$ resolution were distributed along each half of the specimen. The Geokon 4202 sensor was placed 10 cm (4 in.) away from the girder end while the Geokon 4200 sensors were distributed along the length of the beam as shown in Figure 4.6. In addition, a VWSG temperature sensor was attached externally to the girder surface to measure the ambient temperature during load tests. A single data-logger was used to record the VWSG sensor readings during testing. Figure 4.7 shows the placement of FBG and VWSG sensors in the constructed girder.

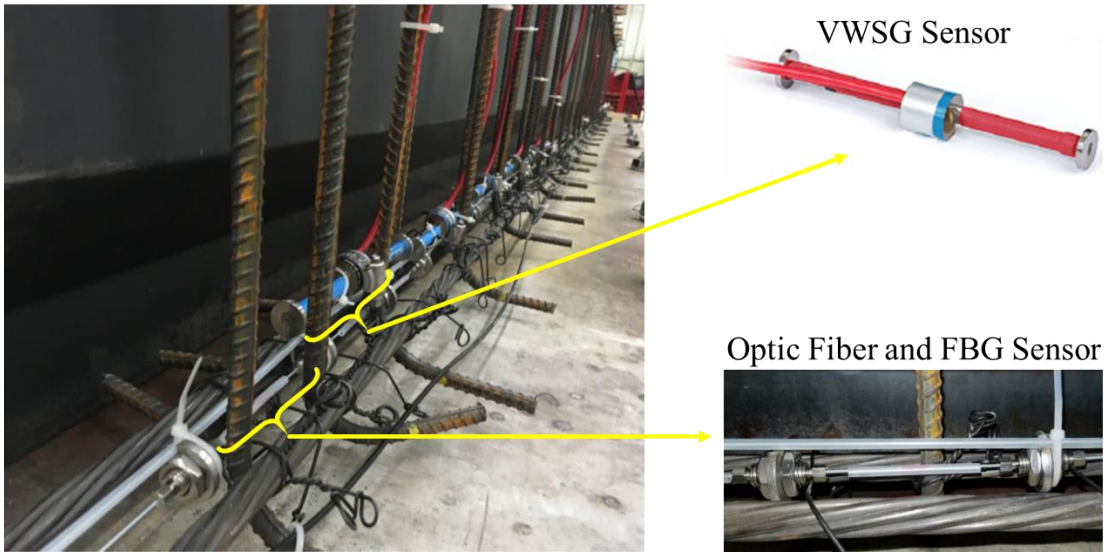

Figure 4.7. Placement of the FBGs and VWSGs in the constructed girder

4.4.4. TEST PROCEDURE AND LOADING

The constructed girder was tested under four-point bending with load points 75 cm (30 in.) away from the mid-span. The point loads were applied through a spreader beam with two support points and a 250 kN (55 kip) hydraulic actuator with MTS FlexTest 60 load controller (MTS, 2019). Figures 4.8a and b show the layout of the loading set up, and the actual test frame constructed in Bert Cooper Engineering Laboratory located at Oklahoma State University. The strain and temperature profiles during the testing were recorded using the FBG sensors with 1,000 Hz sampling frequency. The VWSG sensors were used to record strains during the monotonic tests. A sample from the VWSG sensors was recorded at each load increment. A linear variable displacement transducer (LVDT) was installed at mid-span to measure the beam deflections with 1,000 Hz sampling frequency during all tests. The testing phase consisted of 19 loading runs, including 10 monotonic tests and 9 randomly generated dynamic load tests (i.e., variable amplitude loading). For the monotonic loading tests, the load was applied at a constant rate until a predefined maximum load level was reached; this maximum load was then kept constant for 5 minutes to allow beam inspection. Next, the specimen was unloaded at a constant rate of 13.4 kN/min (3 kip/min) until fully unloaded.

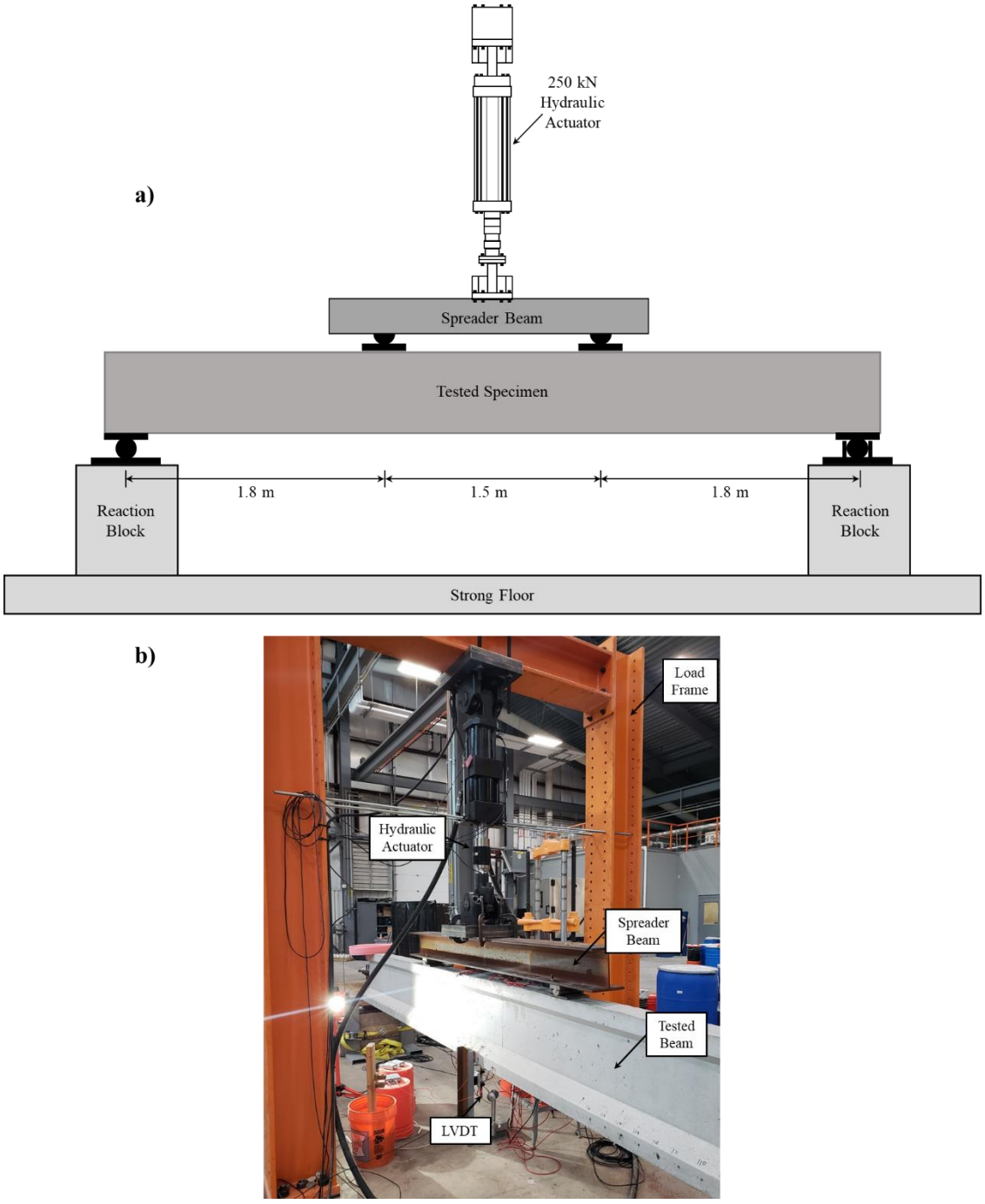

Figure 4.8. (a) Layout of the loading setup (b) test frame and the prestressed girder during load

The experimental phase started with recording the response of the constructed prestressed girder under 3 different randomly generated variable amplitude dynamic loads) and 4 monotonic loads (i.e., Dyna 1 to Dyna 3 and Mono 1 to Mono 4). Table 4.2 shows the attributes of different load runs. Note that the tests IDs are organized with respect to the order of conducting the tests. Next,

another monotonic ramp load (i.e., Crack 1) was applied to the girder at 13.4 kN/min (3 kip/min) loading rate for the first 111 kN (25 kip) and with a reduced rate of 4.45 kN/m (1 kip/min) until the first crack was observed. During the Crack 1 load run, the loading was paused for two minutes at 4.45 kN (1 kip) increments to inspect the beam and identify the crack initiation. This process was continued until the first crack was observed at 160 kN (36 kip). The cracking pattern in this stage can be seen in Figure 4.9.

Table 4.2. Attributes of different load tests

Test ID	Load Type	Maximum load - kN (kip)	Frequency (Hz)	Loading Rate - kN/min (kip/min)	Notes	Duration (s)
Dyna 1	Random	45 (10)	2	---	No cracks	556
Dyna 2	Random	62 (14)	2	---	No cracks	695
Dyna 3	Random	102 (23)	2	---	No cracks – Training & Testing dataset	1,200
Mono 1	Monotonic	45 (10)	---	13.4 (3)	No cracks	440
Mono 2	Monotonic	67 (15)	---	13.4 (3)	No cracks	640
Mono 3	Monotonic	89 (20)	---	13.4 (3)	No cracks	840
Mono 4	Monotonic	111 (25)	---	13.4 (3)	No cracks	1,040
Crack 1	Monotonic	160 (36)	---	Variable	First crack observed	3,000
Dyna 4	Dynamic	102 (23)	2	---	Small cracks	1,075
Dyna 5	Random	107 (24)	2	---	Small cracks	614
Crack 2	Monotonic	191 (43)	---	Variable	Cracks widened	2,600
Dyna 6	Random	107 (24)	4	---	Wide Cracks	321
Dyna 7	Random	107 (24)	6	---	Wide Cracks	241
Dyna 8	Random	107 (24)	8	---	Wide Cracks	175
Dyna 9	Random	107 (24)	10	---	Wide Cracks	308
Mono 5	Monotonic	89 (20)	---	22.3 (5)	Wide Cracks	520
Mono 6	Monotonic	134 (30)	---	22.3 (5)	Wide Cracks	760
Mono 7	Monotonic	156 (35)	---	22.3 (5)	Wide Cracks	880
Mono 8	Monotonic	180 (40)	---	22.3 (5)	Wide Cracks	1,000

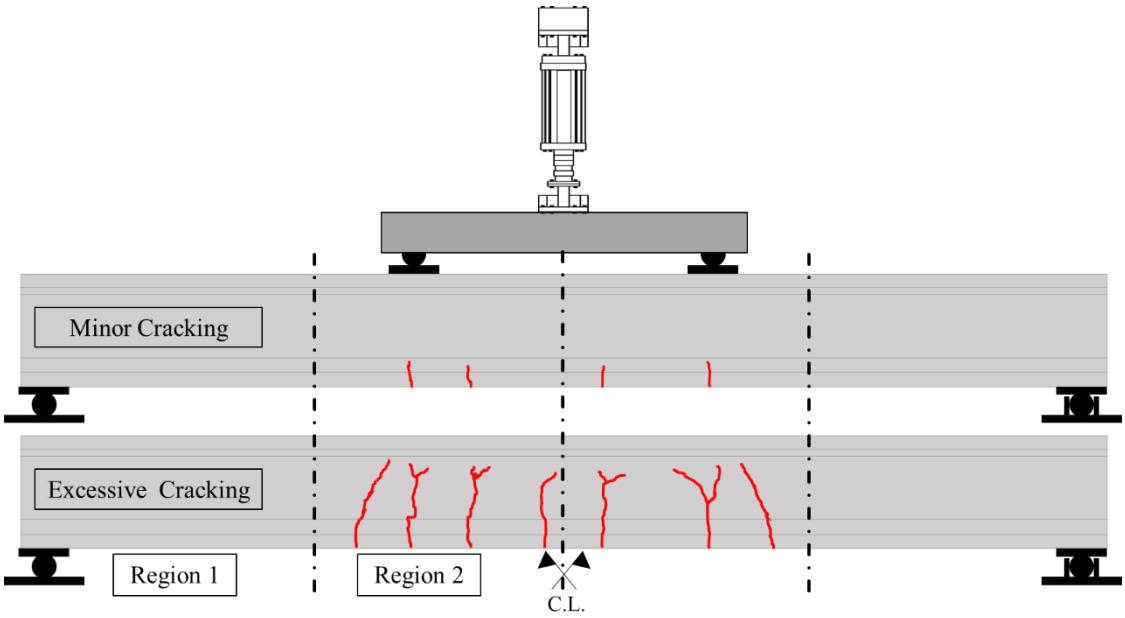

Figure 4.9. View of the beam showing minor and excessive cracking patterns

As shown, four cracks initiated and propagated to a level approximately 100 mm from the bottom fiber of the girder. This condition of the girder is referred to as the *minor cracking* state in this chapter. Two more randomly generated dynamic loads runs (i.e., Dyna 4 and Dyna 5) were applied after the first minor cracking was observed. Next, another monotonic load (i.e., Crack 2) was applied to the girder. The load run was applied at 22.3 kN/min (5 kip/min) for the first 134kN (30 kip) and continued at 4.45 kN/m (1kip/min) loading rate with a pause at each 4.45 kN (1 kip) until the cracks propagated to the upper half of the cross section at 191 kN (43 kip). The damage extent of the beam after this test is referred to as the *excessive cracking* state in this chapter. The crack pattern in this stage is also shown in Figure 4.9. The experiment then continued with applying three more monotonic (i.e., Mono 5 to Mono 8) and four randomly generated dynamic loads (i.e., Dyna 6 to Dyna 9).

4.5. RESULTS AND DISCUSSION

4.5.1. CONCRETE COMPRESSIVE STRENGTH

Concrete compressive strength specimens for the girder were tested at 1, 7, and 28 days of age and before conducting the load tests at 69 days. Table 4.3 presents the average compressive strength of three cylinders tested at the aforementioned ages. The cracking and ultimate capacities of the beam were estimated based on the compressive strength test results, cross-section, and loading configuration to be 148 kN (33.4 kips) and 210 kN (47.2 kips), respectively. These capacities were used to design the loading procedure suitable for developing the proposed damage detection and localization approach.

Table 4.3. Concrete compressive strength test results

Concrete Age (days)	Compressive Strength – MPa (psi)
1	31.7 (4,600)
7	47.4 (6,870)
28	52.9 (7,670)
69 (flexural testing)	57.2 (8,290)

4.5.2. LOAD TESTING AND STRAIN MEASUREMENT USING FBGS AND VWSGS

As indicated previously, the FBG sensors distributed along the girder were used to obtain the strain time histories during monotonic and randomly generated dynamic load tests. Figure 4.10 shows the recorded response of sensor 15 during Dyna 3 load test. To ensure the proper operation of the fiber optic sensors, the strains recorded by the FBGs were compared to those obtained by the VWSGs during monotonic load tests. Figure 4.11 compares the change in strains obtained from FBG sensor 15 to those of the embedded VWSG at mid-span under various monotonic load values. In summary, it was found that the FBG sensors provide a reliable and stable reading at different load levels.

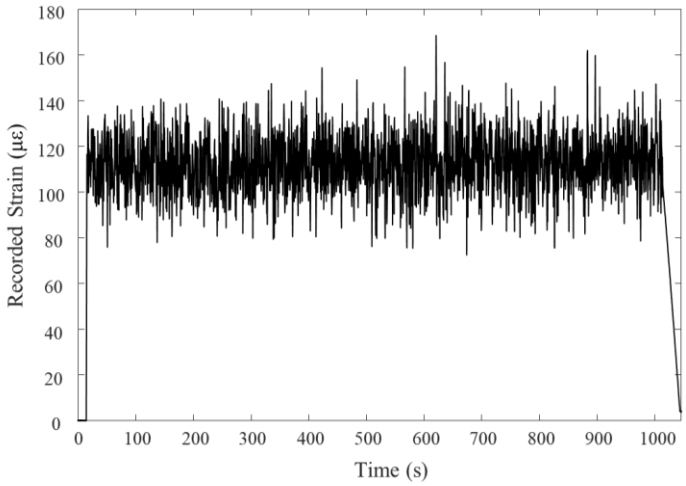

Figure 4. 10. . Recorded strain at sensor 15 during Dyna 3 load test

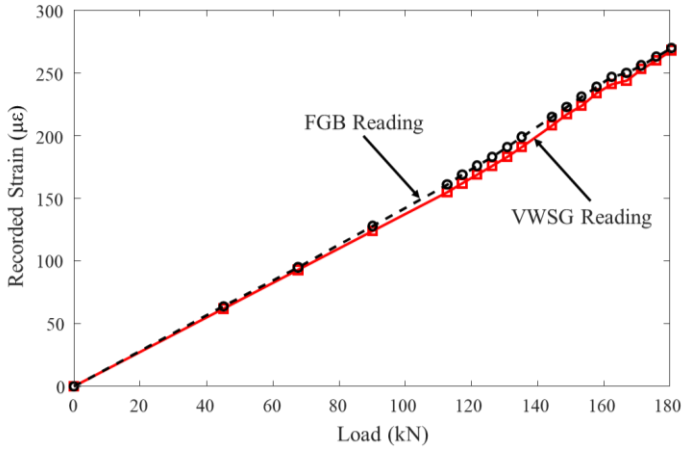

Figure 4.11. Comparison between the measured strains using FGB sensor #15 and the embedded VWSG at mid-span under various monotonic load values

4.5.3. ANN TRAINING

Feed forward neural networks with 10 hidden layers (see Figure 4.1) were used to establish the relationship between the strain readings of sensors along one half of the tested girder. Strain records associated with Dyna 3 load run were randomly divided into training and testing datasets representing 85% and 15% of the data points, respectively. These percentages which are initially selected based on the common practice of ANN applications (e.g., Ezeldin & Sharara 2006; Khandel & Soliman 2019d) were evaluated to make sure both the datasets have similar statistical properties. Note that any other strain record under dynamic loads in pre-cracking stage (e.g.,

Dyna 1 or Dyna 2) can be used for training the ANNs. The strain records of eight sensors, namely 1, 2, 3, 10, 11, 12, 13, and 14 along one half of the beam were used as the input to predict the strains at target sensor 15. Given the large size of the training dataset, statistical analysis was performed, and it was found that a randomly selected 10% of the data can properly represent the statistical properties of the whole training database. However, higher percentage of the training dataset may be needed for other applications. Accordingly, for training each individual ANN, 10% of the training database was randomly selected and used for training. The accuracy of each ANN was then evaluated using the testing database. In order to account for modelling uncertainty associated with ANN predictions, 1,000 individual ANNs were trained in this chapter. Levenberg-Marquardt (Levenberg, 1944; Marquardt, 1963) optimization method was employed to obtain the fitting parameters that minimize the mean square error (MSE) between the predicted strains and the defined target dataset by optimizing the fit parameters in Equation 4.1. The ANNs were created and trained using the MATLAB (MathWorks, 2019) neural network toolbox. For damage detection and localization, the strain readings of the eight sensors from the other load tests were then fed to the 1,000 trained ANNs and the strain time histories for the target sensor were predicted.

4.5.4. ERROR ESTIMATION

The error between the experimentally- and ANN-generated strains was estimated for the testing dataset to evaluate the performance of the trained neural networks. The prediction error associated with individual ANNs was found using Equation 4.2 while the mean, lower bound, and upper bounds of strain prediction error were estimated using Equations 4.3, 4.4, and 4.5, respectively. Figure 4.12a shows the probability distribution of the prediction error, as well as the mean (ME), lower bound (E_{LB}), and the upper bound error (E_{LB}). The mean prediction error was estimated to be very close to zero (7.2823e-04 με), the standard deviation was estimated to 0.1905 με, whereas the lower and upper bounds at 95% confidence intervals were estimated to be

-0.3825 and 0.3846 με, respectively. The small mean error value shows that trained ANNs were able to simulate the behaviour of the girder in the pre-cracking state with high accuracy. In addition, there is 95% confidence that the error in pre-cracking stage falls within the calculated lower and upper bounds. Figure 4.12b shows the ME prediction versus the number of ANNs used to monitor convergence of the proposed framework. As shown, the fluctuation of the mean prediction error is stabilized and limited to approximately 0.00015με after employing 200 ANNs. A similar trend was also observed for convergence of minimum and maximum prediction error. This can imply that the number of employed ANNs and the size of training dataset was adequate to accurately predict the flexural behaviour of the tested girder.

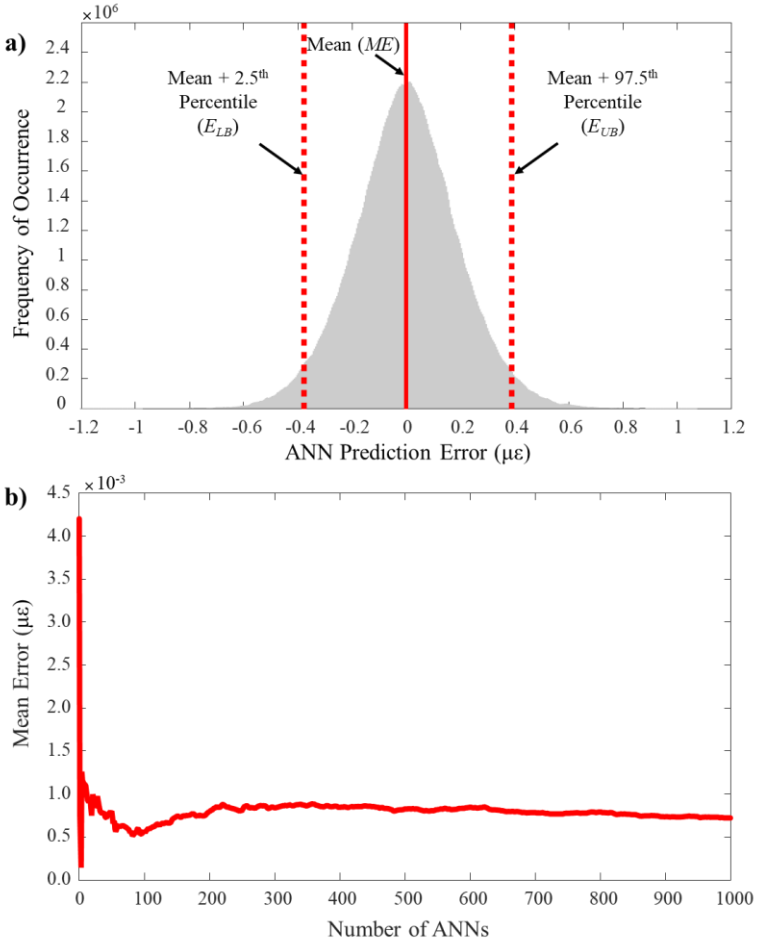

Figure 4.12. (a) Probability distribution of the prediction error (E), mean error (ME), lower bound error (E_{LB}), and upper bound error (E_{LB}) associated with the testing dataset (b) mean error convergence plot

4.5.5. DAMAGE DETECTION

After training the ANNs and evaluating the prediction error, the strain records of sensors 1, 2, 3, 10, 11, 12, 13, and 14 from the set-aside datasets were fed to the trained ANNs and the resulting strain at sensor 15 was predicted. The predicted strains were then compared to the recorded ones during the load tests and the associated mean error was calculated using Equation 4.3 to predict the damage occurrence. Figure 4.13 compares the experimental strain time history to ANN predictions at sensor 15 for two load cases in the pre-cracking (i.e., Dyna 2 test) and post-cracking phases (i.e., Dyna 6 test).

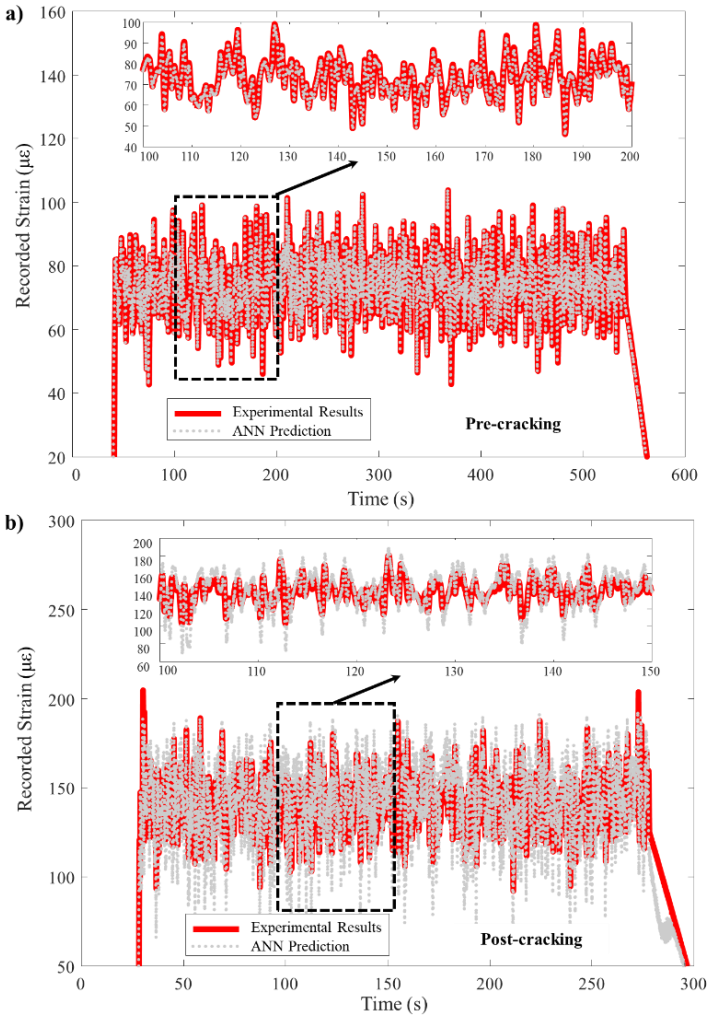

Figure 4.13. Comparison between experimental results and ANN predictions for two load cases in (a) pre-cracking and (b) post-cracking phases

As shown, the trained ANNs were able to accurately predict the strains in the pre-cracking stage, while there seems to be a significant prediction error associated with the post-cracking stage. In other words, the predicted strains at the target sensor are considerably different than the recorded ones. This implies that it is highly likely that damage has occurred. This is based on the fact that due to damage in the post cracking stage, the stiffness of the system changes compared to the pre-cracking state and the relationship between different sensors, established in the uncracked state, leads to an increase in the ANN prediction error. Figure 4.14a shows the mean prediction error for the randomly generated variable amplitude load tests. This figure is divided into three zones, *no cracking*, *minor cracking*, and *excessive cracking*. Referring to Table 4.2, Tests Dyna 1 and Dyna 2 were conducted before cracking the girder, while Tests Dyna 4 and Dyna 5 occurred after load test Crack 1 that resulted in the initiation of minor cracking. Finally, Test Dyna 6 to Dyna 9 were conducted after applying the Crack 2 loading, in which cracks increased in width and length. In the *no crack* zone, the two data points fall within the previously defined upper and lower bounds of prediction error (E_{UB} and E_{LB}). In the other two regions, the prediction error falls outside of the defined criteria indicating the presence of damage in the beam. This highlights the ability of the proposed criterion to detect the damage occurrence. In addition, the large difference between the *ME* values in the minor and excessive cracking regions shows that the proposed approach can indicate the relative level of damage experienced by the girder during load tests. Figure 4.14b shows the mean prediction error for different monotonic load tests. It provides a comparison between the damage prediction results associated with different monotonic load tests. The insert in the no cracking zone highlights the mean prediction error in the first four monotonic runs with respect to the upper and lower bounds. The *ME* values associated with monotonic load tests applied before crack initiation (i.e., Mono 1 to 4) fall within the defined bounds, where the *ME* values for the other cases fall outside of the defined bonds indicating the presence of damage. As shown, larger monotonic loads resulted in larger mean error values. This can be mainly attributed to the fact that larger loads caused larger crack opening and resulted in larger error

compared to the ANN prediction. Note that the specimen was designed to be a fully prestressed with no cracking under service loads. The presented approach can be adapted to partially prestressed beams by relaxing the bounds on prediction errors to permit allowable cracking and isolate excessive cracking. However, more testing may be needed on such cases to establish these new bounds.

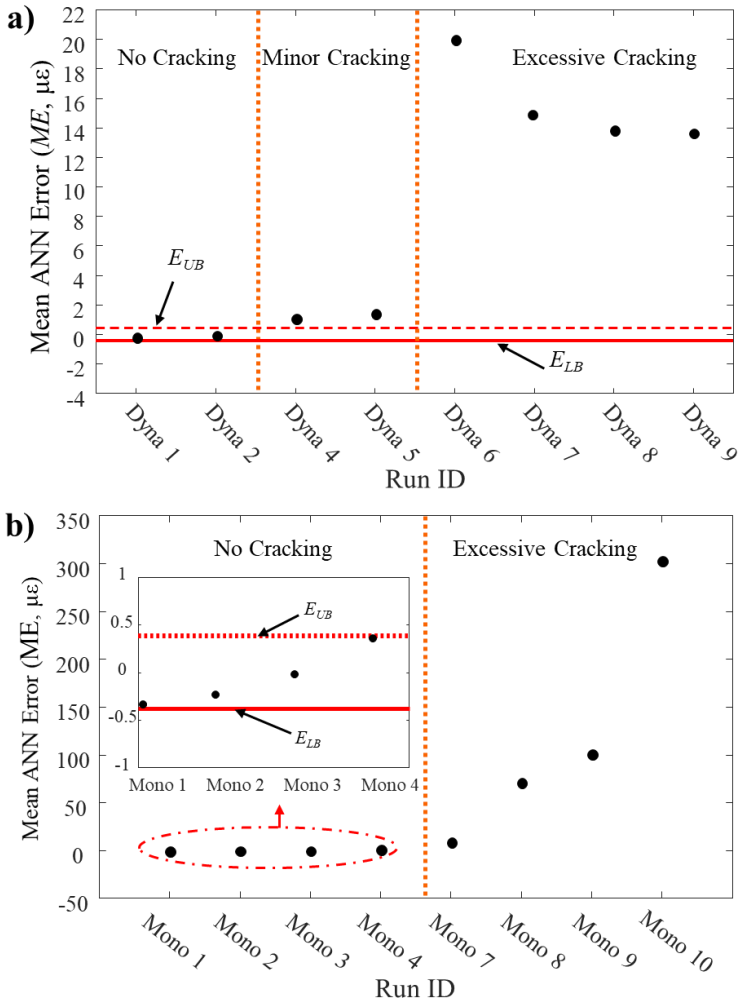

Figure 4.14. Mean prediction error for (a) randomly generated variable amplitude load cases (b) monotonic load tests

4.5.6. DAMAGE LOCALIZATION

In order to localize damage in the tested girder, two damage regions and ANN configurations were defined and trained using the strain records of Dyna 3 load test. Region one was considered

to span between the support and sensor 14 (1.5 m (59 in.) away from the end), and region two was defined to be between sensors 14 and mid-span (i.e., 1.25 *m* (49 in.) away from the mid-span). ANN with configuration 1 (AN 1) used the strain records of sensors 1, 2, 3, 10, 11, 12, and 13 to predict the strain in sensor 14, and ANN with configuration 2 (AN 2) was the same configuration introduced in the damage detection process. Figure 4.15 shows the defined regions and their associated sensors. These configurations are suitable for predicting flexural damage in the tested beam; however, other configurations may be needed to localize damage if other failure modes are expected.

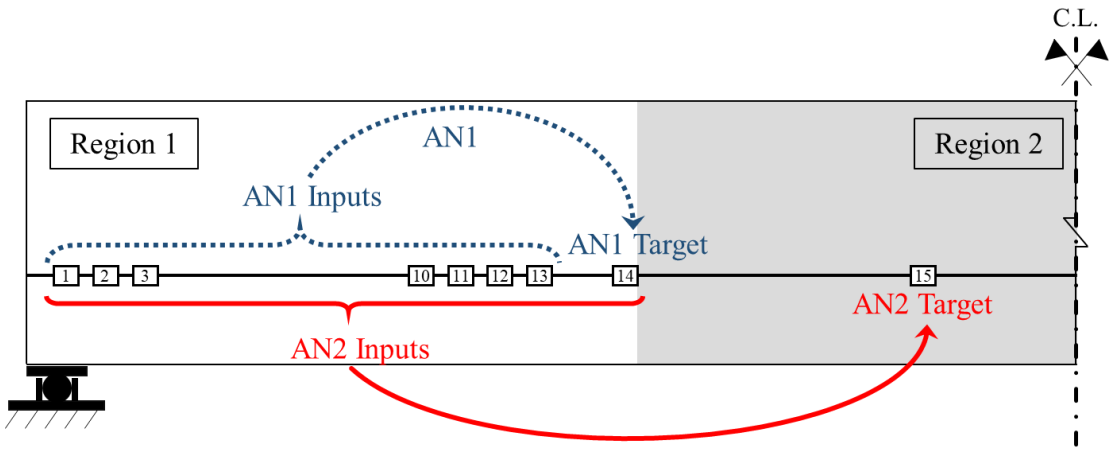

Figure 4.15. Visualization of AN1, AN2, Region 1, and Region 2

The prediction error of each ANN based on Dyna 6 load test was then used to localize damage along the beam. The normalized mean error (*NME*) associated with the prediction of AN1 and AN2 configurations was found using Equation 4.6 and Dyna 6 load test data. Figure 4.16 shows the probability distribution of the calculated *NME* values associated with 1,000 AN1 and AN2 trained ANNs. The mean and standard deviation of the predicted *NME* for AN1 are 0.0233 and 0.0268, respectively. While the mean and standard deviation for AN2 are found to be 0.1767, and 0.0356, respectively. This shows that the established relationship between the sensor readings in Region 1 (see Figure 4.15) can predict the strains in the post-cracking phase with ±2.3% mean error. However, the 17.67% *NME* for AN2 reveals that established relationship between the

sensors in Region 2 (see Figure 4.15) cannot accurately simulate the strains in the post-cracking phase. Accordingly, it is more likely that the cracks occurred in Region 2. This conclusion is also consistent with the observations made during the experiment, where the cracks initiated and propagated in the pure bending zone (see Figure 4.9).

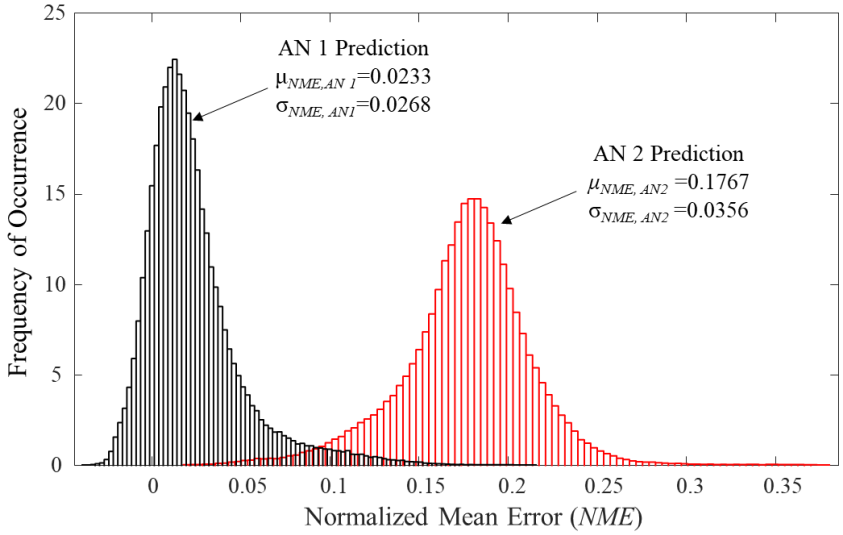

Figure 4.16. Probability distribution of the calculated NME values associated with AN1 and AN2

4.6. CONCLUSIONS

This chapter presented a statistical damage detection and localization approach for evaluating the long-term performance of newly constructed prestressed concrete girders instrumented with fibre Bragg grating sensors. The approach was illustrated using experimental laboratory data obtained from flexural testing of a large-scale prestressed concrete girder under monotonic loads and randomly generated variable amplitude loading. Artificial Neural Networks (ANNs) were employed to establish a relationship between the strain time-histories at multiple sensors distributed along the girder. The trained ANNs were used to predict strain at target sensors based on the readings of other sensors during a load test. The predicted strains were then compared to their experimental counterparts for damage assessment. Lower and upper error bounds were defined based on the intact girder conditions. These bounds were then used to evaluate the condition of the investigated prestressed concrete girder and localize induced damage. The

proposed damage detection approach does not require any information on loading conditions and detects the damage based only on the relationship between different FBG signals. The following conclusions are drawn:

- The employed feedforward ANNs with the adopted characteristics were capable of establishing a relationship between strain readings recorded at various sensors along the tested girders. The predication accuracy was highlighted by low mean error and standard deviation of 7.2823e-04 με and 0.1905, respectively.
- The proposed lower and upper error bounds led to successful detection of various damage levels. The approach was able to identify the occurrence of minor and excessive cracking during testing. The identified damage levels were consistent with observations made during testing. The load tests conducted on the heavily cracked beam showed a large mean error while tests at early cracking stages showed relatively small mean error values that were still out of the defined bounds.
- The proposed damage localization approach was capable of identifying the region that experienced higher damage levels. The identified damage zone matched the observations made during the experimental testing. However, more research is needed to optimize sensor placement and region selection.
- The presented approach has been validated for flexural damage in fully prestressed simply supported beams. More research is needed quantify the effect of loading location, temperature gradients, boundary conditions, and shrinkage and creep strains on the proposed approach. Accordingly, future efforts are required to implement the presented damage identification and localization approach for long-term performance monitoring of bridges under field conditions.

CHAPTER V

SENSITIVITY AND RELIABILITY ASSESSMENT OF CONCENTRIC COMBINATION STEEL CONNECTIONS USING META-MODELING APPROACH

5.1. OVERVIEW

Combination bolted-welded connections are often needed in practice for retrofitting existing structures, updating the design to meet changes in the loading conditions, and addressing construction errors. This chapter quantifies the reliability level of connections, combining slip-critical bolts and fillet welds, using a probabilistic approach that integrates finite element (FE) modeling, meta-modeling, and Monte Carlo simulation. The proposed approach relies on experimental results to quantify the uncertainties associated with various input parameters and calibrate a FE model. The FE model is next integrated into a low-rank tensor approximation process to provide variance-based sensitivity measures associated with the considered random variables. The influential variables, along with the calibrated FE model, are then used to evaluate the reliability by means of adaptive polynomial chaos kriging Monte Carlo simulation. Finally, the proposed approach is applied to combination bolted-welded connections under direct tension to evaluate their time-dependent reliability considering different faying surface conditions. The results of the conducted sensitivity analysis indicated that weld geometry, bolt pretensioning forces, and friction coefficient of steel surface are variables that largely contribute to load carrying response of the investigated connections. For connections with Class A and Class B faying surfaces, the minimum reliability index found to be 3.97 and 3.81, respectively.

5.2. BACKGROUND

Combination welded-bolted connections are mainly used for retrofitting existing structures, resolving construction errors, and improving the capacity to resist updated loading conditions. In this context, the behavior of bolted or welded only connections has been well investigated during in literature. Application of high strength bolts in preventing excessive slip in structural steel joints was first recommended by Batho and Bateman (1934). Wilson and Thomas (1938) observed an improved fatigue performance for cases with pretensioned bolts. The research on this topic continued through the following decade and led to the introduction of first specification for structural joints using high-strength bolts in 1951 (RCRBSJ, 1951) through a cooperative effort between the Research Council on Riveted and Bolted Structural Joints (RCRBSJ) and the American Society of Testing and Materials (ASTM, 1949). This specification permitted the replacement of ASTM A141 rivets with by ASTM A325 bolts on one to one basis (Kulak et al., 2001). The German Committee for Structural Steelwork (GCSS) and British Standards Institution (BSI) published their respective specifications in late 1950s (Kulak et al., 2001). The research in the United States further continued and led to several editions of the RCRBSJ specifications until the introduction of the first edition of the Guide to Design Criteria for Bolted and Riveted Connections by Fisher and Struik (1974). This guideline provided expressed the slip resistance of the bolted connections as the product of number of slip planes, slip coefficient, and total bolt pretension force applied on the connection. This expression is still used as the basis of the modified formulation of American Institute of Steel Construction Specification (AISC, 2017) which considers the effect of bolt pretension over-strength and filler usage.

In 1928, the American Welding Society (AWS) Code for Fusion Welding and Gas Cutting in Building Construction provided guidelines quantifying the shear strength of fillet welds based on the allowable stress on the weld throat Quinn 1991). Further investigation by the Structural Steel Welding Committee in 1931 specified design shear stress threshold of 11.3 ksi (Bowman &

Quinn 1994). Since the introduction of covered electrodes improved the weld behavior, a 20% increase in allowable shear strength, resulting in 93.8 MPa (13.6 ksi) limit, was recommended by Godfrey and Mount (1940). Further investigation by Higgins and Preece (1969) defined the allowable shear strength as 30% of the weld tensile strength. Finally, Fisher et al. (1978) defined the allowable weld shear stress as 60% of the specified minimum tensile strength of the weld electrode. This limit, which is the basis for current shear design provisions (AISC, 2017), assumes that the weld is under pure shear and Von Mises criteria defines its strength.

The research on combination welded-bolted connection has gained attention in late 1960s. In one of the earliest efforts, Steinhardt et al. (1969) conducted an experimental study on several small tension butt splices with bolted-only, welded-only, and combined welded-bolted configurations. The results of their investigation suggested that capacity of combination connections can be predicted as the sum of slip resistance and the ultimate capacity of welds parallel to the loading direction. Holtz and Kulak (1970) further investigated combination connections to evaluate the effect of weld orientation and bolt hole clearance. They recommended that using longitudinal welds substantially improves the load carrying capacity of combination connections. In addition, a research conducted by Jarosch and Bowman (1986) confirmed the higher efficiency of using longitudinal welds compared to transverse welds in combination connections. This study also concluded that the sum of slip resistance and the ultimate capacity of welds parallel to loading direction can well represent the capacity of combination connections. The research into the behavior of combination connections continued by Manuel and Kulak (2000) to further investigate the effects of weld orientation, bolt tension, and bolt bearing condition. This study also confirmed the advantage of using longitudinal welds and introduced an analytical model for estimating the ultimate capacity of combination connection as the sum of contributions of total slip resistance, bolts shear strength, longitudinal welds, and transverse welds. In a more recent effort, Shi et al (2011a and b) investigated the ultimate capacity of combination connections

through experimental testing and finite element (FE) modeling. Their work concluded that the combination connection capacity may not be equal to the sum of the weld capacity and friction resistance and may depend on the on the ratio between bolt to weld capacities. Finally, Waite (2019) conducted an experimental research to investigate the effect of various parameters including bolt pattern, bolt size, tensioning techniques, faying surface, and weld to bolt strength ratio that might affect the behavior of combination connections.

Reliability assessment of slip-critical connections in the literature is limited to a single study conducted by Grondin et al. (2007) with the objective to investigate reliability of bolted only slip critical connections. The study considered the randomness in slip coefficient and pretensioning force based on the available experimental data in the literature. In addition, several studies such as Ng et al. (2002), Callele et al. (2005), Li et al. (2007) Kwan et al. (2010) investigated the reliability of welded connections. However, no combinational connection was investigated in these studies and the reliability analyses were performed based on analytical formulations.

Despite the long history of research on slip critical and combination connections, the lack of a comprehensive reliability analysis on this type of connections is apparent in the literature. Accordingly, this chapter aims to evaluate the reliability of slip-critical combination connection through an integrated framework. The proposed framework considers a full range of uncertainties associated with different parameters that may affect the load carrying capacity of combination connections. A Finite element (FE) model is developed and validated using the experimental test data. The validated model is then integrated with Low-rank Tensor Approximation-based (LRA-based) methods to perform a variance-based sensitivity analysis and evaluate the effect of different random variables on the load carrying capacity of welded-bolted connections. The performed sensitivity analysis is next used to select the variables that greatly affect the load response of the investigated connection. Finally, the selected variables and the validated FE model are used to perform reliability analysis through Accelerated Polynomial Chaos Kriging

Monte Carlo Simulation (APCK-MCS). The effect of long-term pretensioning losses is taken into account. The proposed framework is applied on 2 by 2 combination welded-bolted connections with Class A and B faying surfaces to evaluate the long-term reliability of current AISC formulations.

5.3. VARIANCE-BASED SENSITIVITY

Sensitivity analysis is required to select the key contributing factors that affect the response of a system. In this regard, variance-based Sensitivity methods generally decompose the output variance into a sum of contributions of each or a combination of input variables. This method generally referred as ANalysis of VAriance (ANOVA) and it is applicable to the cases where the input variables are independent. Sobol' indices (Sobol', 2001) are recognized as one of the widely used sensitivity measures defined based on ANOVA method. These indices can be calculated using Monte Carlo simulation, low-rank approximation (LRA), or polynomial chaos expansion (PCE) methods (Marelli et al., 2019a). In this chapter, LRA-based Sobol' indices are employed. The following sections briefly discuss the basics required to perform sensitivity analysis using LRA-based Sobol' indices.

5.3.1. SOBOL' DECOMPOSITION

Consider $f(x)$ as a mathematical model with input vector $\mathbf{X}$ composed of n input parameters which produces a scalar output y as:

$$\mathbf{Y} = f(\mathbf{X}) \qquad \text{where} \qquad \mathbf{X} \in K^n = \{\mathbf{X} : 0 \le x_i \le 1, i = 1,\ldots,n\} \tag{5.1}$$

The Sobol' decomposition (Sobol', 2001) of $f(x)$ is then defined as:

$$f(x_1,\ldots,x_n) = f_0 + \sum_{i=1}^{n} f_i(x_i) + \sum_{1\le i<j\le n}^{n} f_{ij}(x_i,x_j) + \ldots + f_{1,2,\ldots,n}(x_1,x_2,\ldots,x_n) \tag{5.2}$$

where f_0 is constant and equal to expected value of $f(\mathbf{X})$ while the integral of summands with respect to their independent variables is equal to zero as:

$$\int_0^1 f_{i_1,\ldots,i_s}(x_{i_1},\ldots,x_{i_s})dx_{ik} = 0 \quad \text{where} \quad 1 \le k \le s \tag{5.3}$$

Based on Equation 5.3, it can be concluded that the summands are orthogonal to each other. In addition, if the input variables are independent and the integral of the function exists over K^n, the expansion exists and is unique (Sobol', 2001). Accordingly, the univariate and multivariate terms of the decomposition can be found using equations 5.4 and 5.5, respectively:

$$f_i(x_i) = \int_{K^{n-1}} f(x)dx_{\sim i} - f_0 \tag{5.4}$$

$$f_{ij}(x_i, x_j) = \int_{K^{n-2}} f(x)dx_{\sim\{ij\}} - f_i(x_i) - f_j(x_j) - f_0 \tag{5.5}$$

where "~" symbol represents the variables that are excluded (e.g., $\int_{K^{n-1}} f(x)dx_{\sim i}$ symbolizes the integration over all variables except x_i). Finally, using the presented decomposition technique, the total and partial variances can be found using equations 5.6 and 5.7, respectively:

$$D = \int_{D^{\mathbf{X}}} f^2(x)dx - f_0^2 \tag{5.6}$$

$$D_{i_1,\ldots,i_s} = \int_{K^s} f^2_{i_1,\ldots,i_s}(x_{i_1},\ldots,x_{i_s})dx_{i_1},\ldots,dx_{i_s} \quad \text{for} \quad 1 \le i_1 < \ldots < i_s \le n \quad \text{and} \quad s = 1,\ldots,n \tag{5.7}$$

As shown in Equation 5.2, the mean for summands is zero, therefore the sum of partial variances is equal to the total variance:

$$D = Var[f(\mathbf{X})] = \sum_{i=1}^{n} D_i + \sum_{1 \le i < j \le n}^{n} D_{ij} + \ldots + D_{1,2,\ldots,n} \tag{5.8}$$

5.3.2. SOBOL' SENSITIVITY INDICES

Sensitivity indices quantify the relative contribution of input variables with respect to the total variance. Partial Sobol' sensitivity indices associated with each group of variables can be defined based on the ratio of partial to total variances (Sobol', 2001) as:

$$S_{i_1,\ldots,i_S} = \frac{D_{i_1,\ldots i_S}}{D} \tag{5.9}$$

Note that indices associated with only one input variable (i.e., $\mathbf{X_i}$) are referred as first-order Sobol' indices while higher-order Sobol' indices (i.e., $S_{i,j}$, $i \neq j$) accounts for the interaction effects of multiple variables which cannot be separately quantified using first order indices. Total sensitivity (S_i^T) indices are defined as the total of all partial sensitivity indices involving variable *i* as:

$$S_i^T = \sum_{i \subset \{i_1,\ldots,i_S\}} S_{i_1,\ldots,i_S} \tag{5.10}$$

Since the summation of partial indices yields to one, the total sensitivity indices can be also found as:

$$S_i^T = 1 - S_{\sim i} \tag{5.11}$$

where $S_{\sim i}$ represents the sum of all partial indices excluding index *i*.

5.4. SOBOL' INDICES USING LOW-RANK TENSOR APPROXIMATION (LRA-BASED SOBOL' INDICES)

Sobol' indices are originally introduced to be evaluated using Monte Carlo simulation (Sobol', 2001). However, due to large number of samples required for performing Monte Carlo simulation, this method can be computationally expensive for cases with complex models (e.g.,

finite element models). Accordingly, meta-modeling techniques can help to overcome the cost challenge. A meta-model is a computationally inexpensive model capable of providing statistically equivalent results for a complex model without a known closed-form solution through a limited number of original model executions (Konakli and Sudret 2016b). Several meta-modeling tools such as low-rank approximation (LRA) (Konakli and Sudret 2016a), or polynomial chaos expansion (PCE) (Sudret 2008) have been presented in recent years. Among these methods, the former (i.e., LRA) was shown to converge faster and outperform the PCE in predicting extreme model responses (Konakli and Sudret 2016a and b).

5.4.1. NON-INTRUSIVE META-MODELING

Consider $f(x)$ as a computational model that represent the behavior of a complex system; given an input vector $\mathbf{X} = \{x_1, \ldots, x_M\}$, an output vector $\mathbf{Y} = \{y_1, \ldots, y_N\}$ is generated. Since the input vector $\mathbf{X}$ is uncertain, the output vector $\mathbf{Y}$ becomes random. Considering a scalar realization of the response, the following holds true (Konakli and Sudret 2016b):

$$\mathbf{X} \in D_{\mathbf{X}} \subset \mathbf{R}^M \mapsto \mathbf{Y} = f(\mathbf{X}) \in R \tag{5.12}$$

where $D_{\mathbf{X}}$ represents support of $\mathbf{X}$. Accordingly, a meta-model is defined as an analytical function (e.g., $\hat{\mathbf{Y}} = \hat{f}(\mathbf{X})$) that generates results with similar statistical properties as $\mathbf{Y}$. Meta-models can be developed using non-intrusive method which treats the original model (i.e., $f(x)$) as a black box. In this case, a set of input vectors $\boldsymbol{\varepsilon} = \{\mathbf{X}^{(1)}, \ldots, \mathbf{X}^{(N)}\}$ which are generally referred as experimental design samples are assigned to the original model to generate the response $\mathbf{Y} = \{f(\mathbf{X}^{(1)}), \ldots, f(\mathbf{X}^{(N)})\}$ from the original model ($f(x)$). The experimental design samples and the corresponding generated response are then used to develop the meta-model.

5.4.2. LOW-RANK TENSOR APPROXIMATION

Considering the mapping presented in Equation 5.12, a rank one function of the input vector **X** can be expressed as (Konakli and Sudret 2016a):

$$w(\mathbf{X}) = \prod_{i=1}^{M} v_l^{(i)}(\mathbf{X}_i) \tag{5.13}$$

where $v_l^{(i)}$ represents a univariate function of $\mathbf{X}_i$ in the i^{th} dimension and function f can be represented as finite sum of number of rank-one functions. The resulting is a canonical decomposition which its rank is equal to the number of employed rank-one functions. Rank-R approximation of the original function $\mathbf{Y}= f(\mathbf{X})$ can be expressed as (Konakli and Sudret 2016a):

$$\hat{\mathbf{Y}}^{LRA} = \hat{f}^{LRA}(\mathbf{X}) = \sum_{l=1}^{R} b_l \left(\prod_{i=1}^{M} v_l^{(i)}(\mathbf{X}_i) \right) \tag{5.14}$$

where $v_l^{(i)}$ is a univariate function of $\mathbf{X}_i$ of the l^{th} rank-one summand (l = 1, …, R), and b_l is normalizing constant. In addition, $v_l^{(i)}$can be written using polynomial functions as:

$$v_l^{(i)}(\mathbf{X}_i) = \sum_{k=0}^{p_i} z_{k,l}^{(i)} P_k^{(i)}(\mathbf{X}_i) \tag{5.15}$$

where $P_k^{(i)}$ is the k^{th} degree univariate polynomial associated with i^{th} input variable and maximum degree of p_i, $z_{k,l}^{(i)}$ is coefficient of $P_k^{(i)}$ in the the l^{th} term. Finally, due to the orthogonality of the univariate conditions, LRA-based meta model can be written as (Konakli and Sudret 2016a):

$$\hat{\mathbf{Y}}^{LRA} = \hat{f}^{LRA}(\mathbf{X}) = \sum_{l=1}^{R} b_l \left(\prod_{i=1}^{M} \left(\sum_{k=0}^{p_i} z_{k,l}^{(i)} P_k^{(i)}(\mathbf{X}_i) \right) \right) \tag{5.16}$$

5.4.3. CALCULATION OF NON-INTRUSIVE LRA COEFFICIENTS

Using Alternated Least Squares (ALS) minimization is a common practice in calculating LRA coefficients (i.e., $z_{k,l}^{(i)}$). This method treats the problem as a sequential least-squares minimization along only one dimension (i.e., 1, …, M) while freezing all other dimensions. In this regard, Chevreuil et al. (2015) proposed a robust updated greedy algorithm which is capable of providing an optimal selection of LRA coefficients using cross validation techniques. The algorithm adopts a progressive increase in the number of rank-one summands (i.e., approximation ranks) up to a predetermined maximum number. Consequently, a set of candidate decompositions with different ranks becomes available. Generally, the optimal rank *R* is not known beforehand, therefore an efficient algorithm is required to select the optimal-rank decomposition. Konakli and Sudret (2016a) proposed an efficient rank-selection algorithm that relies on average generalization error in a *k*-fold cross validation problem. The algorithm first partitions the experimental design into *n* sets. Next, it allocates *n*-1 partitions to the training set, the remaining one partition is used as a testing set. The training set partitions are used to generate LRAs with increasing ranks. The error of these LRAs is then evaluated using the set aside testing partition. Finally, by minimizing the error, optimal rank (R^{opt}) can be selected. Further details regarding this process can be found in Konakli and Sudret (2016a, b) and Konakli et al. (2019).

5.4.4. CALCULATION OF LRA-BASED SOBOL' SENSITIVITY INDICES

LRA-based Sobol' indices can be calculated based on the developed meta-models in terms of polynomial coefficients ($Z_{k,l}^{(i)}$) and normalizing constants (b_l). In this regard, Konakli and Sudret (2016a) derived an analytical expression for the LRA-based partial and total Sobol' indices as presented in Equations 5.17 and 5.18:

$$S_i = \frac{E\left[E\left[\hat{f}^{LRA}(\mathbf{X}) \mid X_i\right]^2\right] - E\left[\hat{f}^{LRA}(\mathbf{X})\right]^2}{Var\left[\hat{f}^{LRA}(\mathbf{X})\right]} \tag{5.17}$$

$$S_i^T = 1 - \frac{E\left[E\left[\hat{f}^{LRA}(\mathbf{X}) \mid X_{\sim i}\right]^2\right] - E\left[\hat{f}^{LRA}(\mathbf{X})\right]^2}{Var\left[\hat{f}^{LRA}(\mathbf{X})\right]} \tag{5.18}$$

where the expected value, variance and conditional expectation terms can be computed using Equations 5.19, 5.20, 5.21, and 5.22 (Konakli and Sudret, 2016a), respectively:

$$E\left[\hat{f}^{LRA}(\mathbf{X})\right] = \sum_{l=1}^{R} b_l \left(\prod_{i=1}^{M} z_{0,l}^{(i)}\right) \tag{5.19}$$

$$Var\left[\hat{f}^{LRA}(\mathbf{X})\right] = \sum_{l=1}^{R}\sum_{l'=1}^{R} b_l b_{l'} \left(\left(\prod_{i=1}^{M}\left(\sum_{k=0}^{p_i} z_{k,l}^{(i)} z_{k,l'}^{(i)}\right)\right) - \left(\prod_{i=1}^{M} z_{k,l}^{(i)} z_{k,l'}^{(i)}\right)\right) \tag{5.20}$$

$$E\left[E\left[\hat{f}^{LRA}(\mathbf{X}) \mid \mathbf{X}_i\right]^2\right] = \sum_{l=1}^{R}\sum_{l'=1}^{R} b_l b_{l'} \left(\prod_{j\neq i}^{M} z_{0,l}^{(i)} z_{0,l'}^{(i)}\right)\left(\sum_{k=0}^{p_i} z_{k,l}^{(i)} z_{k,l'}^{(i)}\right) \tag{5.21}$$

$$E\left[E\left[\hat{f}^{LRA}(\mathbf{X}) \mid \mathbf{X}_{\sim i}\right]^2\right] = \sum_{l=1}^{R}\sum_{l'=1}^{R} b_l b_{l'} z_{0,l}^{(i)} z_{0,l'}^{(i)} \left(\prod_{j\neq i}\left(\sum_{k=0}^{p_i} z_{k,l}^{(j)} z_{k,l'}^{(j)}\right)\right) \tag{5.22}$$

Further details regarding these expressions can be also found in Konakli and Sudret (2016a and b) and Konakli et al. (2019).

5.5. RELIABILITY ANALYSIS METHODS

A proper reliability quantification approach should consider a full range of uncertainties associated with the system properties (e.g., uncertainties associated with physical properties or environmental and operating conditions). This task can be performed through classical

approximation methods such as First and Second Order Reliability Methods (i.e., FORM and SORM, respectively), simulation methods such as Monte Carlo Simulation (MCS), and methods based on meta-modeling such Kriging. Classical approximation methods generally aim to approximate the limit state function through gradient-based search, while simulation methods offer a sample-based estimation of failure probability (P_f). Kriging (i.e., Gaussian process regression) surrogate models are capable of approximating the limit state function with high accuracy. Among these three methods, MCS solution is usually known as the reference solution (Sudret 2008). However, due to large number of samples required, this method may not be applicable to cases with computationally demanding models (e.g., complex finite element models). In addition, among the classical approximation and meta-modeling methods, the latter method generally converges faster and provides results with higher accuracy (Marelli et al., 2019b). Accordingly, in this chapter, a meta-modeling approach is selected to perform the reliability analysis.

5.5.1. ACCELERATED KRIGING MONTE CARLO SIMULATION (AK-MCS)

Accelerated Kriging Monte Carlo Simulation (AK-MCS) can provide an efficient solution for cases with computationally expensive response functions. This method can significantly reduce the number of model evaluations in comparison with traditional MCS method. AK-MCS employs Kriging meta-models to surrogate the original response model. Ordinary Kriging (Echard et al. 2011) or Polynomial-Chaos-Kriging (PC-Kriging) (Schöbi et al. 2016) can be used as a surrogate model in this method. Due to the faster convergence, PC-Kriging method is employed to perform the reliability analysis in this chapter.

5.5.2. KRIGING META-MODELS

Kriging (also known as Gaussian process modeling) is a stochastic algorithm built based on the assumption that the model output $f(x)$ is an outcome of a Gaussian process (Lataniotis, et al. 2019). A Kriging meta-model can be described as (Santner et al., 2003):

$$f^K(x) = \beta^T \lambda(x) + \sigma^2 Z(x,\omega) \tag{5.23}$$

where $\beta^T\lambda(x)$ is the trend or mean value of the Gaussian process, in which $\{\beta_j, j=1, \ldots, P\}$ is known as regression coefficient and $\{\lambda_j, j=1, \ldots, P\}$ is the basis function. In addition, σ^2 is the variance of the Gaussian process and $Z(x,\omega)$ is a stationary Gaussian process with zero mean and unit variance. Model $f^K(x)$, given the input vector $\mathbf{X}=\{x_1, \ldots, x_n\}$, generates the corresponding output response vector $\mathbf{Y}=\{y_1=f(x_1), \ldots, y_n=f(x_n)\}^T$, the Kriging meta-model then predicts the response based on the assumption that the original model and Kriging model have a joint Gaussian distribution. Further details regarding Kriging meta-models can be found in Santner et al., (2003) and Lataniotis, et al. (2019).

5.5.3. POLYNOMIAL CHAOS KRIGING MONTE CARLO SIMULATION (PCK-MCS)

Polynomial Chaos Kriging (PCK) simulates the original model response using a combination of global and local approximations. In this method, the global approximation is predicted using polynomial chaos expansion (PCE) trends while the local approximation is performed using Gaussian process. This combinational model leads to more efficient and more accurate meta-model construction than using PCE or ordinary kriging meta-models alone (Schöbi and Sudret 2014). A PC-kriging model can be built based on the ordinary kriging meta-model in the following format (Schöbi et al., 2016):

$$\hat{f}^{(PCK)}(x) = \sum_{\tau \in T} \beta_\tau \psi_\tau(x) + \sigma^2 Z(x,\omega) \tag{5.24}$$

where $\sum_{\tau \in T} \beta_\tau \psi_\tau(x)$ is the trend, $\{\beta_\tau, \boldsymbol{\tau} = \tau_1, \ldots, \tau_n\}$ is the regression coefficients, $\{\psi_\tau(x), \boldsymbol{\tau} = \tau_1, \ldots, \tau_n\}$ is the corresponding orthogonal polynomial. In addition, based on the assumption that input variables are independent, the multivariate polynomials can be expressed as the tensor products of univariate polynomials (Schöbi et al., 2016):

$$\psi_\tau = \prod_{i=1}^{M} \psi_{\tau_i}^{(i)}(x_i) \tag{5.25}$$

where $\psi_{\tau_i}^{(i)}(x_i)$ is univariate polynomial with degree of τ_i for the i^{th} variable.

Guided sampling algorithms such as Sobol'' sequence sampling (Sobol' and Levitan, 1999), Latin Hypercube sampling (McKay et al., 1979), and Halton sequence sampling (Halton, 1964) can be used to select an optimal set of samples for generating initial experimental design vector (i.e., input set **X**)**.** Sobol' The corresponding response of the original model $\mathbf{Y}=f(\mathbf{X})$ is then computed based on the initial experimental design samples. Next, a PC-Kriging meta-model is developed using the generated **X** and **Y**. The candidate samples are selected and introduced as the next sample set **X***. The selected sample is fed to the original model to generate the response **Y***. The **X** and **Y** datasets are then enriched using the generated **X*** and **Y***. The enriched **X** and **Y** are used to further calibrate the meta-model. This process is iteratively repeated until the meta-model prediction reaches the desired level of accuracy. Finally, the resulting calibrated meta-model is used to produce response values and estimate the resistance function based on a large set of candidate samples $\mathbf{S}=\{\boldsymbol{x}_1, \ldots, \boldsymbol{x}_n\}$.

5.5.4. PERFORMANCE FUNCTION, PROBABILITY OF FAILURE, AND RELIABILITY

This This chapter focuses on evaluating the reliability of combination connections. The reliability of the connections with respect to the AISC formulation for welded-bolted slip critical

connections will also be investigated. The AISC specification (AISC, 2017) estimates the load carrying capacity of combination connections as:

$$R_n = n_b n_s \mu D_u h_f T_b + n_w (0.6 F_{EXX})(0.707 wl) \tag{5.26}$$

where n_b is number of bolts, n_s is number of slip planes, μ is the friction coefficient, D_u is bolt pretension coefficient, h_f is factor for fillers, T_b is the pretention load of bolts, n_w is the number of weld lines, F_{EXX} is ultimate strength of weld, w is the weld size, and l is the weld length.

In addition, AISC specification (AISC, 2017) considers load and resistance factors to account for uncertainties associated load estimations and resistance formulations, respectively. The general form of load and resistance factor design (LRFD) is presented as (Ravindra and Galambos, 1978):

$$\phi R_n \geq \sum_{k=1}^{i} \gamma_k S_{km} \tag{5.27}$$

where ϕ is the resistance factor, R_n is the nominal resistance, γ_k and S_{km} are the load factors and mean load effects. In addition, based on AISC (2017) recommendations, in presence of dead and live loads, the following load combination should be considered:

$$\phi R_n \geq (1.2\overline{D} + 1.6\overline{L}) \tag{5.28}$$

where $\overline{D}$ is load effect due to mean dead load and $\overline{L}$ is the mean of the maximum lifetime live load. In order to evaluate the reliability of the AISC (2017) formulations, the effects of load and resistance factors should be considered. However, since the connections may be used in different structural designs and be subjected to different loading conditions, estimating the loads applying on the connections is challenging task. Accordingly, given different live to dead load ratios, the AISC (2017) resistance formulation can be used to estimate the applied loads in terms of dead loads in the following form:

$$\overline{D} < \left(\frac{\phi R_n}{1.2 + 1.6\left(\frac{\overline{L}}{\overline{D}} \right)} \right) \tag{5.29}$$

The mean total load effects acting on the connection ($\overline{L}_T$) can be presented as:

$$\overline{L}_T = \overline{D} + \overline{L} \tag{5.30}$$

Given the uncertainties associated with dead and live load effects acting on the connection, the total load effect can be then generated as:

$$L_T = \lambda_D \overline{D} + \lambda_L \overline{L} \tag{5.31}$$

where λ_D and λ_L are dead and live load uncertainty factors, respectively.

The following performance function can be then defined to quantify the reliability of investigated connection:

$$G(\mathbf{X}) = R(\mathbf{X}) - L_T \tag{5.32}$$

where $G(\mathbf{X})$ is the performance function, $R(\mathbf{X})$ is the resistance calculated using trained meta-model and given the vector of random variables ($\mathbf{X}$). L_T is the total load effects calculated using Equation 5.31. PCK-MCS method is then employed to compute the probability of exceedance and reliability index of the slip-critical connections as:

$$P_e = P[G(\mathbf{X}) < 0] \tag{5.33}$$

$$\beta = \phi^{-1}\left[1 - P_e\right] \tag{5.34}$$

where P_e is the probability of exceedance, $G_i(\mathbf{X})$ is the performance function associated with each random sample set (i), β is the reliability index, and ϕ^{-1} is the inverse cumulative distribution function (inverse CDF) of the standard normal distribution.

5.6. INTEGRATED SENSITIVITY AND RELIABILITY ASSESSMENT FRAMEWORK

Figure 5.1 shows the layout of the proposed framework for performing reliability analysis. The presented framework starts with adopting available experimental test results and manufacturer reports to evaluate the uncertainties associated with material properties and construction variability. The required input parameters for developing a finite element model including pretensioning forces, ultimate weld strength, Yong's modulus of weld materials, slip-dependent friction coefficient, weld length, and weld thickness are then adopted and the uncertainty associated with each of them is evaluated. A finite element model based on the measured input parameters during experimental testing is then developed. The created FE model is calibrated and validated with respect to the experimental test results. The calibrated FE model is used to perform LRA-based sensitivity analysis given the marginal distribution of the input parameters. The computed Sobol' indices are next used to rank the effect of investigated random parameters on the resistance function response. The uncertainties associated with random variables with small Sobol' indices are ignored to reduce the complexity and computational cost associated with training the surrogate model. Next, the selected random variables are uniformly distributed and used to train a PCK surrogate model. The actual distributions of the random parameters are then used to test the accuracy of the trained surrogate model. Finally, the performance function is then defined as explained in equation 5.27. Monte Carlo simulation is conducted using the selected random variables, and the trained Kriging model. Finally, equations 5.28 and 5.29 are used to calculate probability of exceedance and reliability indices.

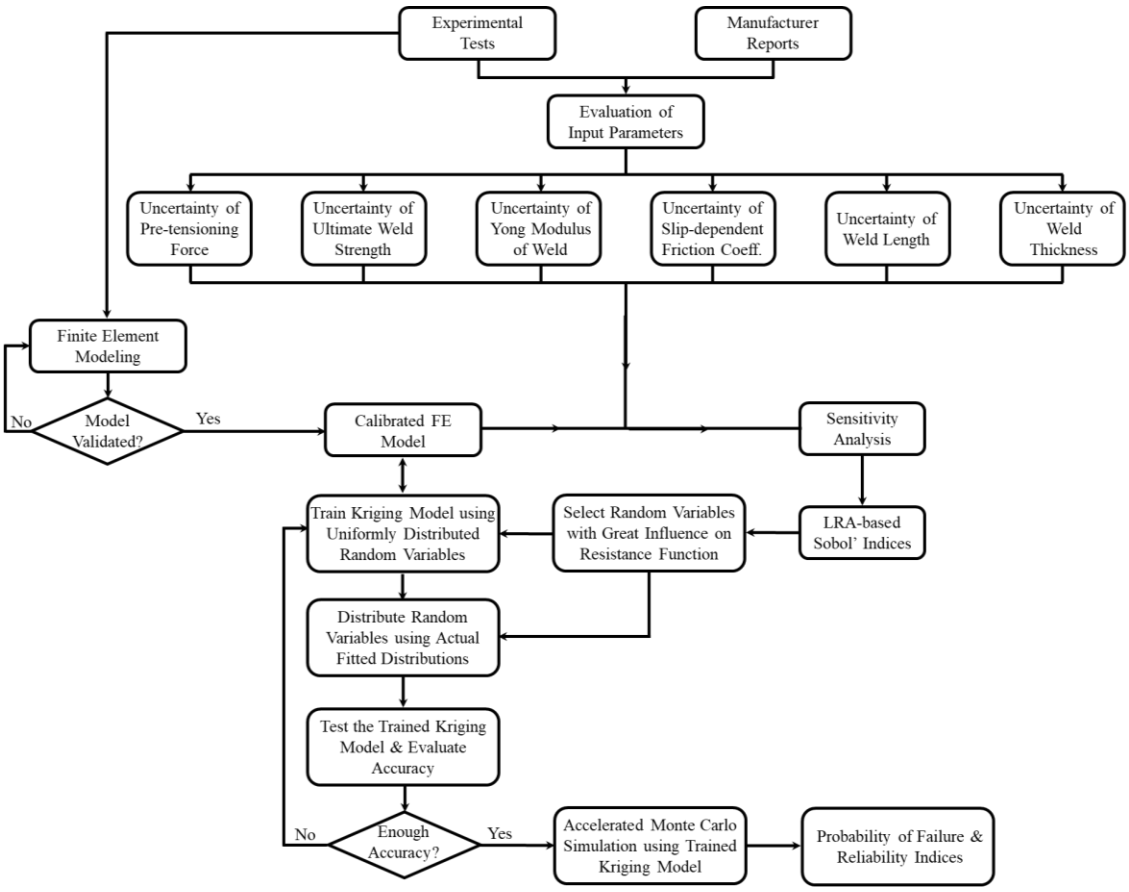

Figure 5.1. layout of the proposed framework for quantifying the reliability of bolted-welded connections

5.7. CASE STUDY

Two configurations of 2×2 axial double lap connections fabricated and tested in Waite (2019) are selected for investigation in this chapter. One configuration is constructed using plates with Class A faying surface condition while the other utilizes blast cleaned (i.e., Class B) faying surface. The specimens consist of three parts, the tested connection, the anchorage zone, and the connection grip. A schematic layout of the specimens is presented in Figure 5.2a. The selected bolted-welded configurations contain four A325 bolts with 19 mm (¾ in.) diameter. Two 22 mm (7/8 in.) thick splice plates and a center plate with 38 mm (1.5 in.) thickness are used to fabricate both configurations. A set of three identical specimens for each configuration were fabricated and tested in Bert Cooper Engineering Laboratory in Oklahoma State University. The configured Class A specimens contained four 76 mm (3 in.) long and 8 mm (5/16 in.) thick weld lines, while

the configured Class B specimens contained four 89 mm (3.5 in.) long and 8 mm (5/16 in.) thick weld lines. Figure 5.2b show the dimensions and configurations of investigated Class A and B connections, respectively. The tests were conducted under monotonically increasing with displacement control procedure. Further details regarding the experimental procedure and specimen design can be found in Waite (2019). The results of these experiments will be used to validate the numerical results presented in the finite element section of this chapter.

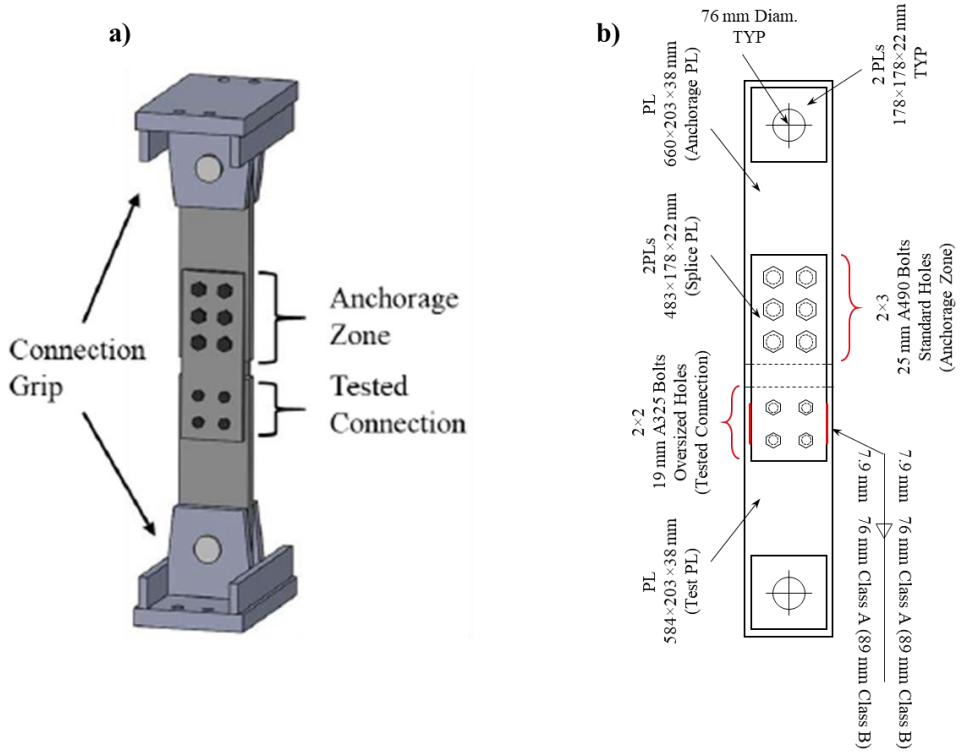

Figure 5.2. (a)Schematic layout of the tested specimen (b) configurations of the tested Class A and Class B specimens

5.7.1. RANDOM VARIABLES

To properly assess the probabilistic behavior of the connection, the following parameters are considered as random variables: Pretensioning loads, friction surface coefficient, weld length, weld size, weld strength, and modulus of elasticity of weld material. The weld size (i.e., leg size) and weld length of a total of 424 weld lines were recorded during the experimental testing program conducted by Waite (2019). The weld size was specified to be 8 mm (5/16 in) thick for

all of the specimens while weld length varies among the specimens. However, due to welding variability, the measured weld sizes and weld lengths for individual weld lines were slightly different than the specified values. Accordingly, the experimental weld size measurements are used to find the statistical properties of the collected weld sizes and lengths. Figure 5.3a shows the histogram and the best fit Probability Density Function (PDF) of the measured weld size. The result of chi-square goodness-of-fit test at 5% significance level conducted by MATLAB (MathWorks 2019) shows that the data follows a normal distribution with mean of 7.04 mm (0.277 in.) and standard deviation of 0.76 mm (0.03 in.). Due to the unequal weld lengths specified for different specimens, the measured weld length associated with each specimen is normalized with respect to its corresponding specified value and a normalized construction variability is defined. Figure 5.3b shows the PDF of the normalized weld length variability and its fitted distribution. It is found that the normalized weld length variability follows a normal distribution with mean of 1.051 and standard deviation of 0.047. Note statistical properties of construction variability herein are also in line with values suggested by Gaspar et al. (2009).

The uncertainty associated with weld strength is evaluated based on more than 700 weld strength test results collected by Kwan et al. (2010). Analysis of the provided data shows that the mean and coefficient of variation of the measured-to-nominal ratio of the ultimate tensile strength are 1.127 with 0.082, respectively. In addition, it is assumed that Yong's modulus of weld material follows a normal distribution with mean and standard deviation of 200 GPa (29,000 ksi) and 14 GPa (2,030 ksi), respectively (Hess et al., 2002).

Grondin et al. (2007) collected the results of more than 1,400 slip resistance tests and reported the slip coefficient for steel connections with Class A and Class B faying surfaces. A review of their collected database indicates that the friction coefficient for Class A follows a lognormal distribution with mean and standard deviation of 0.352 and 0.085, respectively, while the Class B data follows a normal distribution with mean and standard deviation of 0.545 and 0.113,

respectively. Figure 5.4a and b show the PDF of experimental friction coefficient data collected by Grondin et al. (2007) and the best fit distribution confirmed by chi-square goodness-of-fit test at 5% significance level using MATLAB (MathWorks 2019) for Class A and B surfaces, respectively.

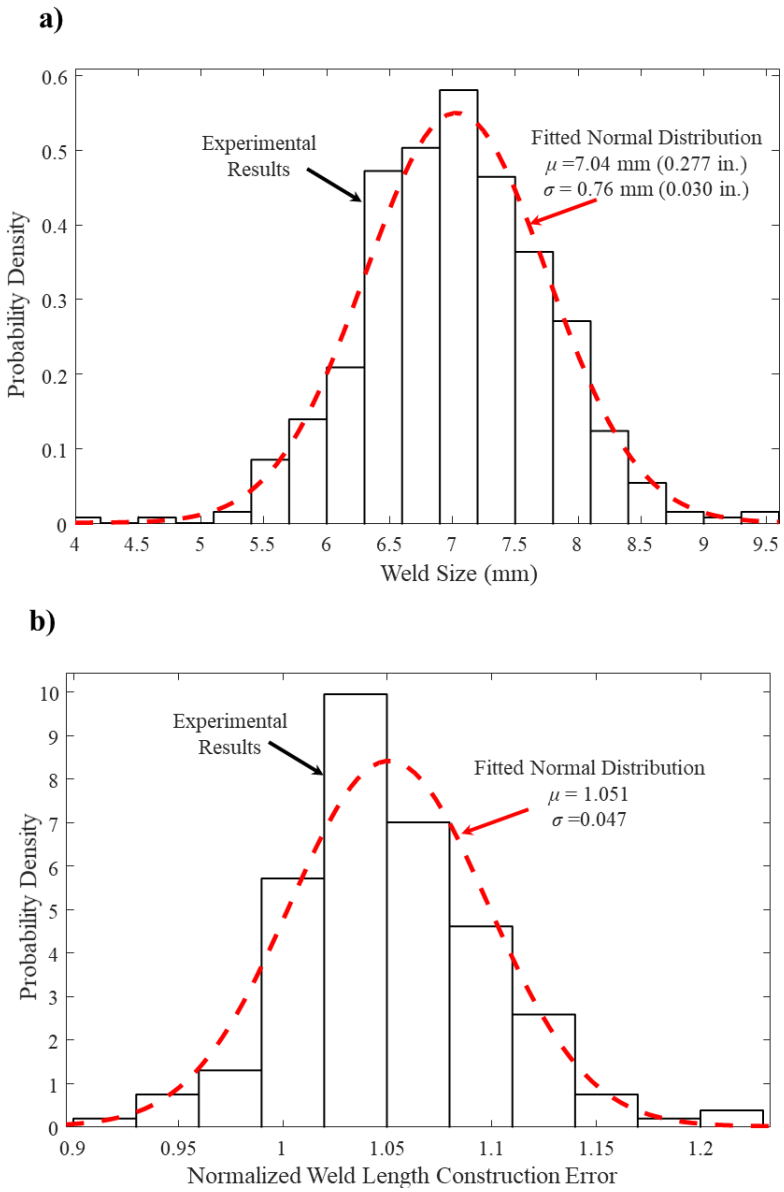

Figure 5.3. Histogram and the best fit PDF of (a) the measured weld size (b) the normalized weld length variability

Finally, Figure 5.5 shows the histogram of the experimentally recorded pretensioning force adopted from (Waite 2019) and its best fit distribution. The conducted chi-square goodness-of-fit

test at 5% significance level conducted using MATLAB (MathWorks 2019) shows that normal distribution with mean of 174.8 kN (39.3 kip) and standard deviation of 21.09 kN (4.74 kip) provides the best fit for pretensioning force data. The ratio of the adopted mean value to the minimum pretension for ASTM A325 bolts is equal to 1.4. It should be noted that this value is in line with the Research Council on Structural Connections (RCSC, 2004) recommendations. In case of turn of nut tightening method, RCSC (2004) proposes that pretensioning load may be distributed normally with the mean pretension about 1.35 times the specified minimum pretension for ASTM A325 bolts. Finally, Table 5.1 presents the statistical properties of the adopted random variables.

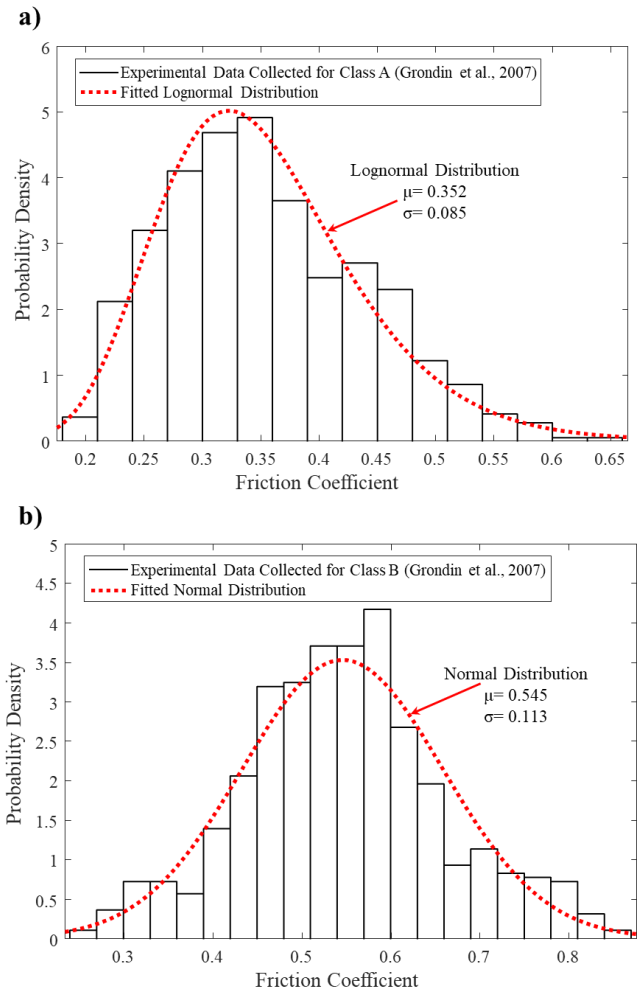

Figure 5.4. PDF of experimental friction coefficient data collected by Grondin et al. (2007) and the best fit distribution for (a) Class A connections (b) Class B connections

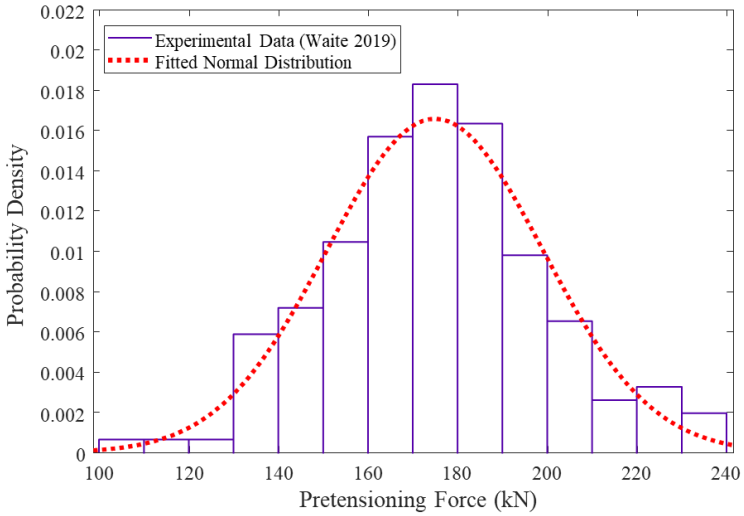

Figure 5.5. Histogram of the experimentally recorded pretensioning force adopted from (Waite 2019) and its best fit distribution

5.7.2. FINITE ELEMENT MODELING

A three-dimensional Finite Element (FE) model is developed in ABAQUS (2018) environment to simulate the behavior of the investigated connections under the applied loads. Steel plates, steel bolt, and welds are modeled as elastic perfectly-plastic materials. ABAQUS Explicit solver was used to predict the connection behavior. Surface-to-surface contact is used to model the contact and sliding between the plates considering the developed slip-dependent friction curves. In addition, to simulate the contact between the connected plates, pretensioning force is applied to the bolts. The tangential contact between the bolt holes and bolt shanks is considered frictionless. Tie constraint is used for connecting the welds elements to the plates. This constraint eliminates the degrees of freedom on the slave nodes (i.e., plate nodes) by tying them to the nodes on the master surface (i.e., weld nodes).

Hexahedral solid elements with 8 nodes (ABAQUS C3D8R element) is used to mesh the weld and plate while bolts are meshed using 4-node tetrahedral elements (ABAQUS C3D4 element). All parts except the contact regions are meshed using 0.3 seed size. Seed size of 0.1 is defined for the contact regions (i.e., around the holes and the weld region) to overcome any convergence

difficulties and prevent unrealistic excessive stress concentrations. Loads and Boundary conditions of the model are defined in accordance with those in experimental test setup. Loading is defined in two steps. First, the bolts' pretension force is defined by applying pressure force on the annular area of the bolt heads. Second, to avoid element distortion and diversion, a slow-rate displacement of 0.5-mm/min (0.02 in/min) is applied at the tip of the center plate while pinned supports are applied to the end of splice plates. Figure 5.6 shows the modeled connection, location of applied displacement, fixed end supports, and pretensioning surface.

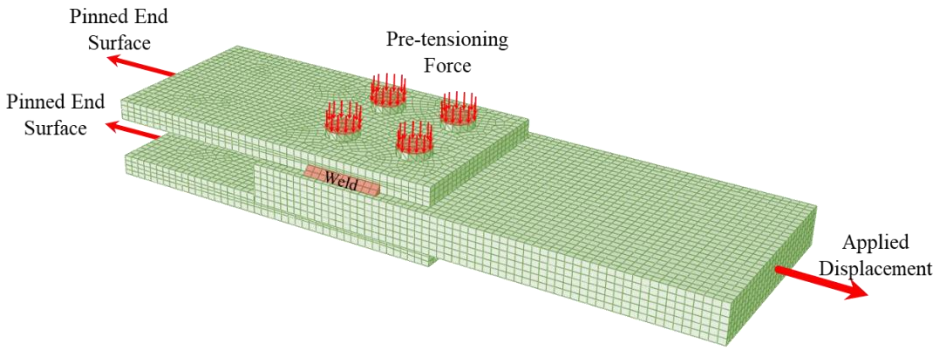

Figure 5.6. The modeled connection, location of applied displacement, fixed end supports, and pretensioning surface

Waite (2019) tested six bolted only 2×2 connections with A325 bolts to investigate the slip behavior of the bolted only connections with Class A faying surface. In addition, five more connections with identical geometry and A325 bolts were tested for investigate the slip behavior of connections with Class B faying surface. Given the total pretensioning force and slip-force curves recorded during the experiments, slip-dependent friction coefficient curves for connections with Class A and B are generated. The slip-dependent friction coefficient is estimated based on Equation 5.26, where nb is equal to 4, ns is equal to 2, Du is assumed 1 since the actual pretensioning force is available, and hf is assumed 1.0 since no filler plate was used. The total friction force (Fs¬¬) can be described as the product of friction coefficient (μ), number of bolts (nb), number of slip planes (ns), and pretensioning force (Tb). Accordingly, the slip-force curves of six and five bolted only specimens associated with Class A and B faying surfaces, respectively,

recorded by Waite (2019) are used to generate slip-dependent friction coefficient (μsd) curves (i.e., μsd =Fs/(nb.ns.Tb)). The mean of the generated curves associated with each faying surface category (i.e., Class A and B) is then used to develop baselines that represent the general shape of slip-dependent friction coefficient curves. These baseline curves are then adjusted with respect to the variability in friction coefficient tests available in the literature. Figure 5.7 shows the individual and mean slip-dependent friction coefficient curves for Class A faying surfaces generated based on Waite (2019) test results.

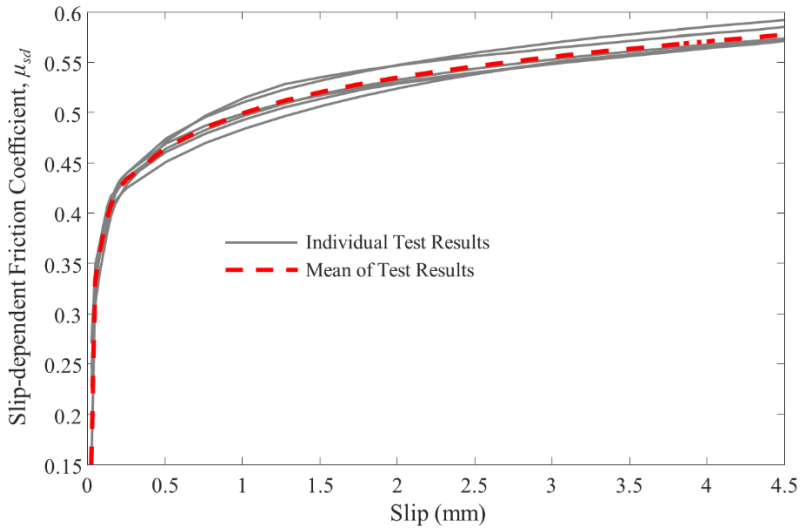

Figure 5.7. The individual and mean slip-dependent friction coefficient curves for Class A faying surfaces generated based on Waite (2019) test results

Given the mean value of input parameters recorded during the experimental tests, a FE model representing the investigated connection is built in ABAQUS (2018) environment. Figure 5.8a and b compare the force-slip curves of the FE analysis and three experimental tests associated with Class A and Class B specimens, respectively, conducted by Waite (2019).

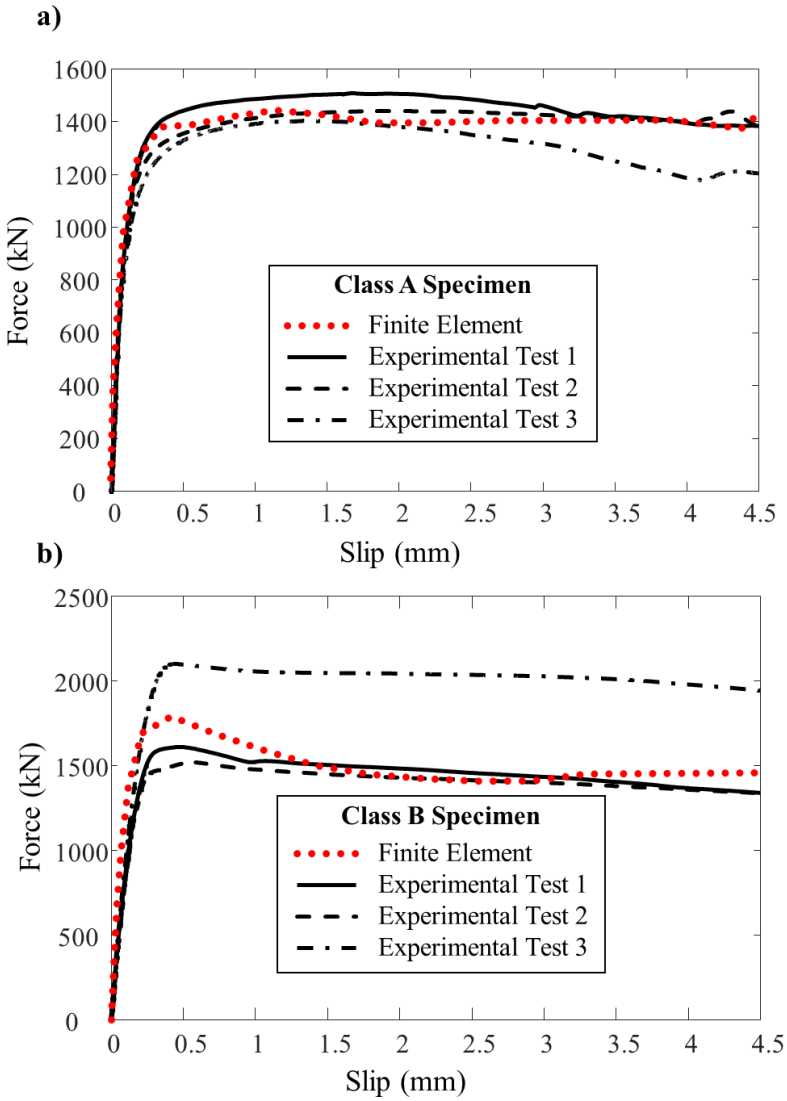

Figure 5.8. Comparison of force-slip curves of the FE analysis and three experimental tests associated conducted by Waite (2019) for (a) Class A and (b) Class B specimens

The figure shows that the developed FE model is capable of providing results with a reasonable accuracy. The slip resistance of the investigated connections is defined as the maximum load recorded before 0.5 mm (0.02 in.) of deformation. For both Class A and Class B connections, the slip resistance derived from the FE model matches the mean of the experimental results of with less than 3% error. To confirm the validity of the adopted FE modeling methodology, several other slip critical connections with various specifications from the Waite (2019) experiments have been also simulated using the adopted finite element methodology. The comparison of the experimental results with their FE counterparts also supports the accuracy of the proposed finite

element modeling approach with error values smaller than 5%. However, to account for uncertainties associated with FE modeling, a bias factor following a lognormal distribution with mean and standard deviation of 1.03 and 0.0152, respectively, is defined. Figure 5.9 shows the lognormal probability plot corresponding to the FE modeling prediction error in comparison to mean of experimental results conducted by Waite (2019). The statistical properties of the bias factor are derived based on the comparison of mean experimental results and FE modeling.

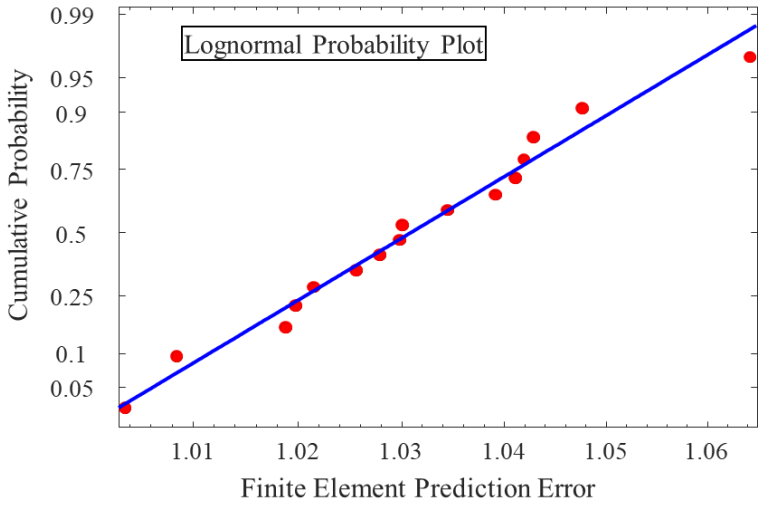

Figure 5.9. The lognormal probability plot corresponding to the FE modeling prediction error in comparison to mean of experimental results conducted by Waite (2019)

5.7.3. SENSITIVITY ANALYSIS

The validated FE model is integrated with LRA to compute partial and total Sobol' sensitivity indices using Equations 5.17 and 5.18, respectively. UQ-Lab (Marelli et al., 2014) MATLAB toolbox is employed to perform the sensitivity analysis on the Class A connection type. The analysis is performed using 1,000 synthetic experimental design samples. The pretensioning force, friction coefficient, modulus of elasticity, ultimate strength of weld material, weld length, and weld size are considered as input parameters. The statistical properties of the considered random variables are defined in accordance with the Table 5.1.

Table 5.1. Statistical properties of the adopted random parameters

Parameter	Distribution	Mean	Standard Deviation	Reference
Weld Length Construction Variability (measured/nominal ratio)	Normal	1.051	0.047	Waite (2019)
Weld Size	Normal	7.04 mm (0.277 in)	0.76 mm (0.030 in)	Waite (2019)
Friction Coefficient (Calss A)	Lognormal	0.352	0.085	Grondin et al. (2007)
Friction Coefficient (Calss B)	Normal	0.545	0.113	Grondin et al. (2007)
Pretensioning Force	Normal	174.82 kN (39.30 kips)	21.09 kN (4.74 kips)	Waite (2019)
Weld Strength Factor (measured/nominal ratio)	Normal	1.127	0.092	Kwan et al. (2010)
Yong Modulus of Weld Material	Normal	200 GPa (29,000 ksi)	14 GPa (2,030 ksi)	Hess et al. (2002)
Dead Load Uncertainty Factor	Normal	1.05	0.105	Melchers & Beck (2018)
Live Load Uncertainty Factor	Gumbel	1.0	0.25	Melchers & Beck (2018)
FE Bias Factor (FE/experimental)	Lognormal	1.03	0.0152	Derived
PCK Bias Factor (Class A)	Normal	1.00045	0.0109	Derived
PCK Bias Factor (Class B)	Normal	0.99957	0.0133	Derived

The response of the system is defined as the maximum FE predicted load corresponding to displacements smaller than 0.5 mm (0.02 in). A MATLAB script is prepared to create the input file required to construct the FE model, execute it, and collect the results given the input samples selected for construction of the sensitivity evaluation model. A LRA-based meta-model is generated and used for calculating the Sobol' indices. A convergence test is conducted to ensure that the number experimental design samples is adequate. Figure 5.10 depicts the calculated total Sobol' indices versus number of samples. As shown, the fluctuation of the calculated Sobol' indices are stabilized and limited to 0.02 after using more than 500 samples. This can imply that the number of sample size (i.e., 1,000) is adequate to accurately predict the sensitivity of the investigated connection.

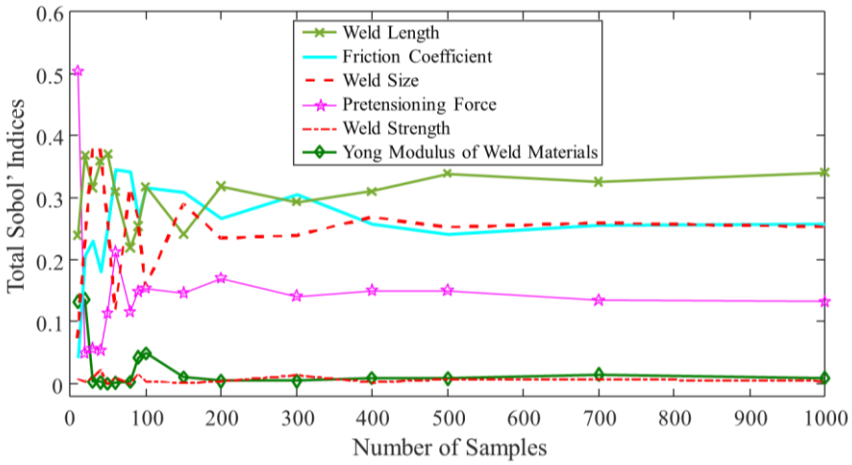

Figure 5.10. The calculated total Sobol' indices versus number of samples

Table 5.2 presents the computed total Sobol' indices using the 1,000 FE model evaluations. As shown, the system response is mostly sensitive with respect to the weld length, weld size, friction coefficient, and pretensioning force. On the other hand, the Yong modulus and strength of the of the weld material seem to have a minimal contribution to the response Sobol'given their low total sensitivity index of 0.0097 and 0.0047, respectively. Weld length has the largest contribution to the model response with the corresponding Sobol' index of 0.3410, weld size and friction coefficients are equally important with indices of 0.2529 and 0.2578, respectively, while pretensioning has the lower index of 0.1331. The computed indices show that the variability associated with the modulus of elasticity and ultimate strength of the weld material has a negligible effect on the system response. Accordingly, the pretensioning force, friction coefficient factor, weld length, and weld size are considered as effective random variables for performing the reliability analysis while the other parameters are assumed deterministic.

Table 5.2. Computed Sobol indices using 1,000 experimental design samples

Parameter	**Total Sobol' Indices**
Weld Length	0.3410
Weld Size	0.2529
Friction Coefficient (Class A)	0.2578
Pretensioning Force	0.1331
Weld Strength	0.0047
Yong Modulus of Weld Material	0.0097

5.7.4. RELIABILITY ANALYSIS

After evaluating the Sobol' indices and selecting the influential input parameters that have a significant effect on the connection response, the FE model is integrated into the PCK-MCS reliability quantification approach. A polynomial chaos kriging model, given by Equations 5.24, is trained to perform accelerated Monte Carlo simulation. The statistical characteristic of the selected random parameters (i.e., pretensioning force, friction coefficient factor, weld length, and weld size) are used to generate a training database for the surrogate model. The defined distributions are used to find the maximum and minimum values of the random variables. In order to prevent biasness with respect to predefined distributions, the derived ranges are used to train the PCK surrogate model by uniformly distributing the random variables. Sobol' sequence experimental design sampling technique (Sobol' and Levitan, 1999) is used to sample from these distributions and train the surrogate model. The model is trained using 3,000 synthetic experimental design points.

The accuracy of the trained model is then evaluated using a testing dataset. The testing dataset, consisting of 500 samples (i.e., 250 samples for each of the faying surface classes) drawn from the actual distributions of the data (see Table 5.1), is used to evaluate the accuracy of the trained model. Figure 5.11a and b compare the finite element results and the PCK prediction for the investigated Class A and B connections, respectively. As shown, the PCK meta-model is capable of providing results with high accuracy with coefficient of determination (R2) values of 0.966 and 0.971 for Class A and Class B connections, respectively. In order to address the modeling uncertainty in the analysis, bias factor between the PCK predictions and FE results is used to generate a distribution accounting for the error associated with the PCK prediction. The probability density function of the collected error and the fitted normal distribution associated with the results of Class A and B connections are plotted in Figures 5.12a and b, respectively. As shown, the bias factor associated with Class A connections follows a normal distribution with

mean of 1.00045 and standard deviation of 0.01090. The computed bias factor for Class B connections also shows a normal distribution with mean of 0.99957 and standard deviation of 0.01330.

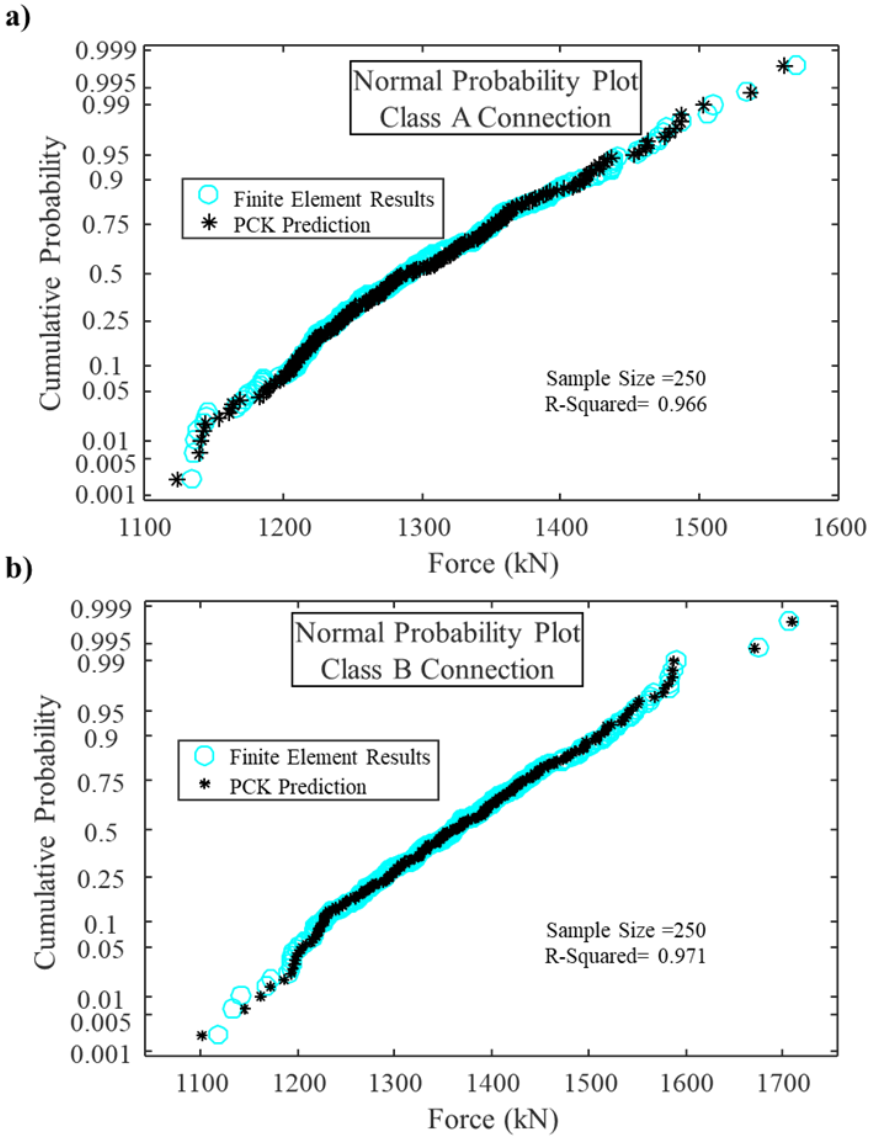

Figure 5.11. Comparison of the finite element results and the PCK prediction for the investigated (a) Class A and (b) Class B connections

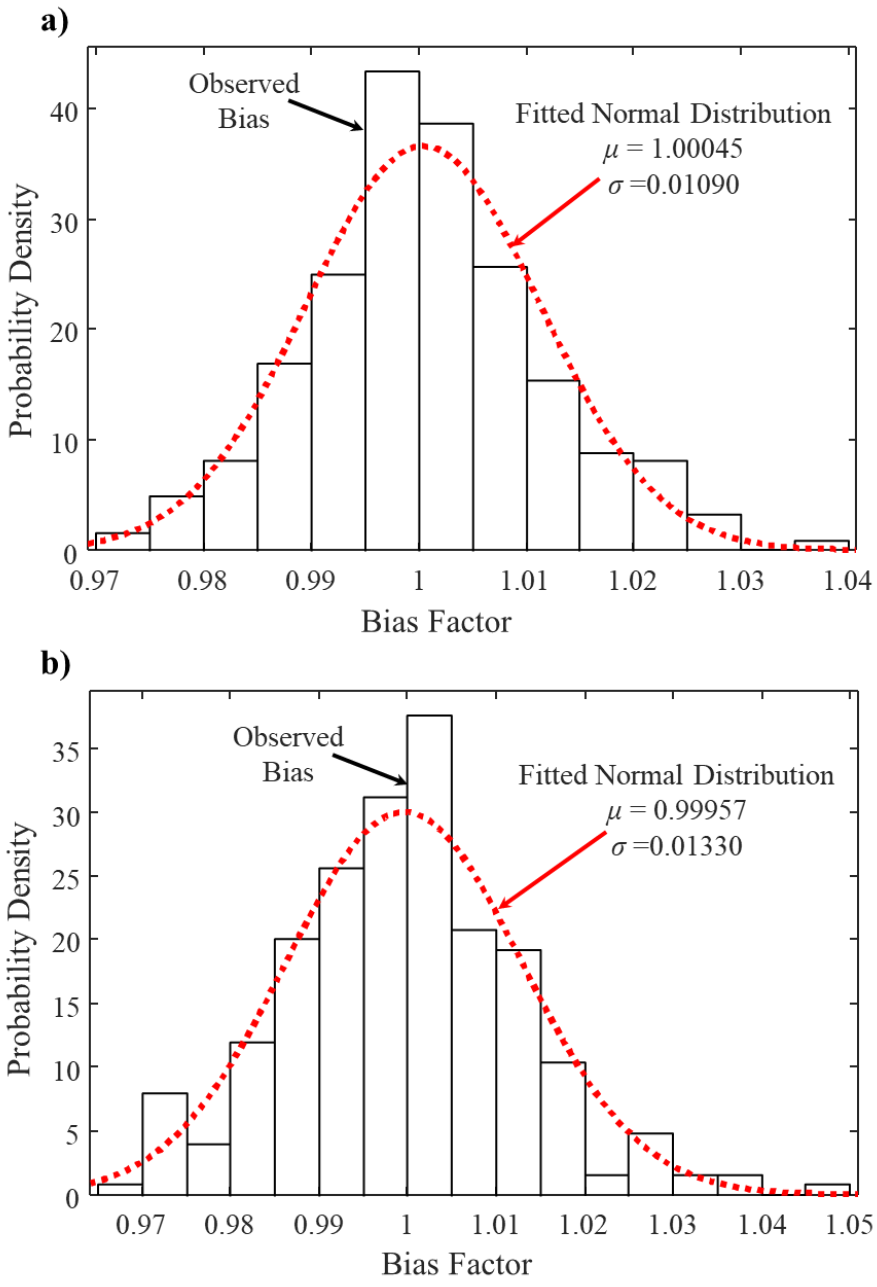

Figure 5.12. PDF of the collected error and the fitted normal distribution associated with the results of (a) Class A and (b) Class B connections

Next, the statistical properties of the considered random parameters associated with the investigated Class A and Class B connections (see Table 5.1) are used to perform accelerated Monte Carlo simulation by employing the trained PCK model. The performance function is defined in accordance with equations 5.32. The load effects are defined based on equations 5.29

to 5.31. Four lines of weld (i.e., nw=4) with nominal specified weld size of 8 mm (5/16 in) with lengths of 76 mm for Class A and 89 mm for Class B examples are used. Ultimate strength of weld is defined as 483 MPa (70 ksi). Four 19 mm (¾ in) pretensioned bolts with AISC recommended minimum pretensioned values of 124.5 kN (28 kips) and bolt pretention coefficient of 1.13 are used (i.e, Du =1.13, nb=4, and Tb=124.5 kN). Two slip planes with no fillers in accordance with AISC recommended friction coefficient of 0.3 for Class A and 0.5 for Class B surfaces are considered (i.e., hf =1, ns=2 and, and μ=0.3 or 0.5 for Class A or B). Finally, the probability of failure and reliability index are found using equations 5.33 and 5.34, respectively. Four million random samples are used to perform the reliability analysis. The sufficiency of the sample population is evaluated through a convergence test. Figure 5.13 a and b show the convergence plot for probability of failure corresponding to connections with Class A and Class B faying surface, respectively. As shown, in both cases, the fluctuation of the calculated probability of failure is limited to relatively small value of 5e-6 when the sample population is larger than 3 million.

The performed analysis on the investigated Class A connection indicated that for different live to dead load ratios ranging from 0.5 to 5, the exceedance probability can vary in range of 5e-7 to 2.7e-5 while reliability indices ranging from 4.9 to 4, respectively. In addition, the investigated Class B connection resulted in exceedance probability of 5e-7 to 4.27e-7 and reliability indices of 4.9 to 3.9.

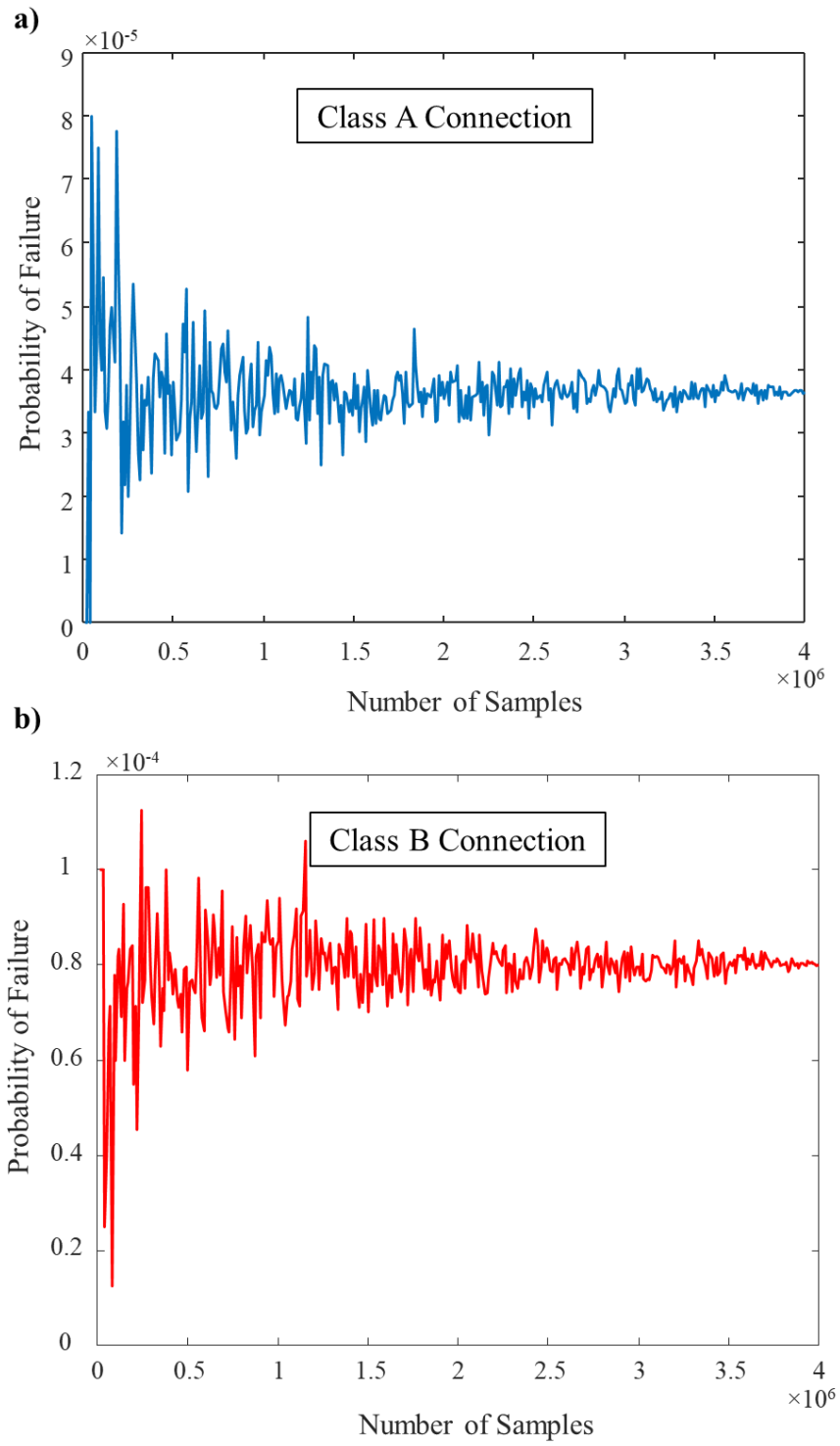

Figure 5.13. Convergence plot for probability of failure corresponding to connections with (a) Class A and (b) Class B connections

5.7.5. TIME DEPENDENT RELIABILITY OF CLASS A AND B CONNECTIONS

The loss of pretension of the bolts under cyclic loading and along the time may results in lack of clamping force and occurrence of slip at forces lower than designed loads. Consequently, this can also affect the long-term reliability of the connections. Accordingly, the effect of pretension loss should be considered in long-term reliability of the investigated connections. In this regard, Heistermann (2011) investigated the long-term behavior of pretensioned bolts in slip-critical connections. Analysis of their provided data shows that the long-term pretension loss (P_{loss}) can be predicted as follows:

$$P_{loss} = \frac{F_{LT}}{F_0} = \left[1 - \frac{(0.7497\ln(T) + 1.4190)}{100}\right] \tag{35}$$

where F_{LT} is the long term pretension force, F_0 is the initial pretension force applied on the bolts, and T is the time in seconds. Figure 5.14 shows the calculated pretension loss percentage during a 20-years time-span. As shown in the figure, loss rate is faster during the first few hours of the bolt tightening while a slower rate occurs afterwards.

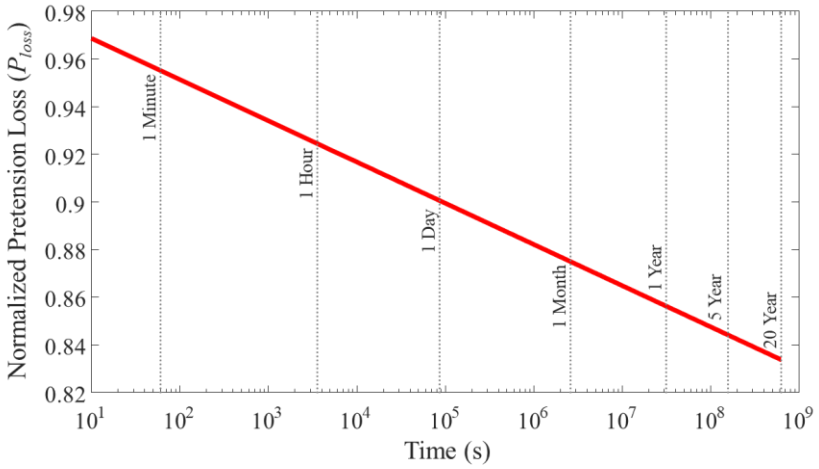

Figure 5.14. Calculated pretension loss percentage during a 20-years time-span

In order to evaluate the long-term reliability of the investigated connections, the effects of pretension losses are considered next. The proposed reliability analysis approach is employed to

perform the time-dependent reliability assessment. The pretensioning losses along the service life are computed in accordance with Equation 5.30 and used to modify the pretension force. The modified forces are then used to compute the time-variant reliability of the steel connections. Note that the pretensioning forces adopted from Waite (2019) are collected two hours after tightening the bolts, meaning that the losses during the first two hours are already taken into account in the measurements and adopted random variables. Accordingly, the predicted effect of pretension losses during the first two hours are not considered in the analysis. Figure 5.15a and b show the time-dependent reliability indices for the investigated Class A and Class B connections, respectively. As shown, The long-term reliability of the Class A connections after 20 years and for different live to dead load ratios ranges from 4.9 to 3.97. In addition, the long-term reliability of the Class B connections after 20 years and ranges from 4.9 to 3.81. In both cases, the maximum variability of reliability due to pretension loss during the 20-years period is limited to 5%. However, the variability in reliability due to different live to dead load ratios can reach to 22%. This can imply the superior effect of live to dead load ratio on reliability of the steel connections.

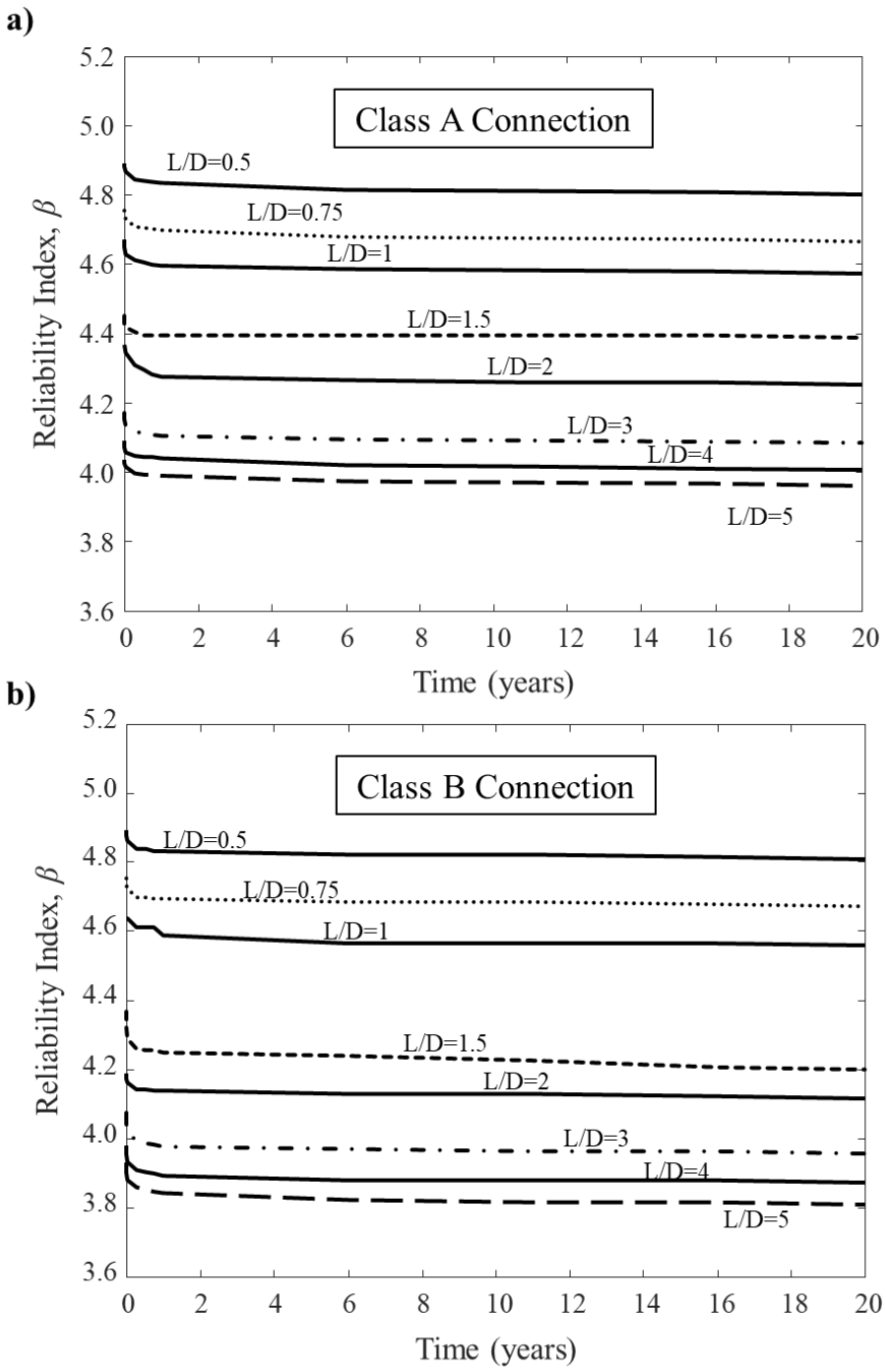

Figure 5.15. Calculated time-dependent reliability indices for (a) Class A and (b) Class B connections

5.8. CONCLUSIONS

The presented chapter aimed to propose an efficient integrated framework to evaluate the reliability of combination connections using experimental test results, finite element modeling,

and meta-modeling simulation methods. The experimental data was used to quantify the uncertainties associated with different parameters that affect the load carrying capacity of combination connections and calibrate a finite element model. The validated FE model was then integrated with Low-rank Tensor Approximation method to quantify variance-based sensitivity measures and rank the effect of different random variables on the load carrying capacity of welded-bolted connections. Variables with the small sensitivity measures were then ignored, the remaining variables that greatly affect the capacity response along with the validated FE model were used to perform reliability analysis by means of Accelerated Polynomial Chaos Kriging Monte Carlo Simulation. Finally, the proposed approach was applied on 2 by 2 combination bolted-welded connection with Class A and B Faying surfaces. The following conclusions were drawn:

- The results of the sensitivity analysis showed that the load carrying response of the investigated Class A connection mainly depended on weld length, weld size, friction coefficient, and pretensioning force. The Yong modulus and strength of the of the weld material seemed to have a minimal effect on the load capacity of the connection at slip limit of 0.5mm (0.02 in).
- Long-term reliability of the Class A connections after 20 years and for different live to dead load ratios of 0.5 to 5 was computed to be ranging from 4.9 to 3.97. In addition, the long-term reliability of the Class B connections after 20 years was found to be in range of 4.9 to 3.81.
- In both cases of connection with Class A and Class B faying surfaces, the maximum variability of reliability due to pretension loss during the 20-years period was limited to 5%, while the effect of live to dead load ratio on reliability of the steel connections was found to reach 22%.

CHAPTER VI

CONCLUSIONS AND RECOMMENDATIONS FOR FUTURE WORK

6.1. CONCLUSIONS

This dissertation presented probabilistic approaches that employ machine learning and surrogate modeling techniques in damage detection and performance assessment of civil infrastructure. The presented research can help in predicting the structural behavior under the effect of natural hazards while considering future climate variability and the potential deterioration due to aging. The developed approaches were formulated to consider the various sources of uncertainty associated with capacity and load effects. Surrogate modeling techniques are used to accelerate complex mechanistic simulations that can be highly expensive from a computational perspective. Based on the presented research, the following conclusions are drawn:

- The application of machine learning in infrastructure management has a great potential to improve the current state of art in risk and reliability assessment, fragility analysis, and damage identification. The superior response approximation accuracy and the reasonable computational cost are among the main advantages of using machine learning. However, analysis should be conducted to establish the optimum network configuration that maximizes prediction accuracy and prevents overfitting.

- Integrating deep neural networks into the flood fragility estimation can lead to a significant reduction in the computational cost. For example, the analysis conducted in Chapter III saved approximately 58,000 hours of finite element simulations.
- Traditional methods for streamflow prediction based on historic data can provide an inaccurate estimation of the bridge failure risk under flood and flood-induced scour. The approach proposed in chapter II, provides rational means for predicting future risk while properly accounting for uncertainties associated with future climate and flood conditions.
- The employed neural network architecture was able to predict the streamflow with a sufficient accuracy. The comparison of the streamflow prediction results obtained in Chapter II and III showed that the deep learning approach outperformed the IHACRES model and decreased the prediction error by 10%.
- Results of the bridge performance assessment showed that scour propagation within the investigated soil conditions can significantly reduce the bridge reliability against future floods. The scour prediction process depends on the streamflow at the bridge location, which can be significantly altered with the future variability in climate conditions. This highlights the importance of considering climate change when designing appropriate scour countermeasures to reduce the failure probability.
- The feedforward ANNs that were employed in the damage detection and localization approach in Chapter IV enabled detecting and localizing damage in the prestressed girder without requiring detailed loading information.
- The adopted ANNs were capable of establishing a relationship between strain readings recorded at various sensors along the tested girder. The predication accuracy was highlighted by low mean error and standard deviation. Additionally, the identified damage zones were consistent with the observations made during the experimental testing.

- Kriging meta models helped in developing an efficient integrated approach for evaluating the reliability of combination connections. Additionally, kriging models also assisted in quantifying the sensitivity of the load carrying capacity of the connection with respect to various input parameters. In both cases, the kriging surrogate models lead to a significant reduction in the computational cost.

6.2.RECOMMENDATIONS FOR FUTURE WORK

- The presented research on Chapter II and III focused on quantifying the risk and fragility of an individual bridge under climate change effects. However, flood events may affect several bridges simultaneously across a transportation network. Accordingly, future efforts should aim at providing methodologies to quantify the effects of climate change on a regional transportation network level.
- The probabilistic performance prediction methods depend to a great extent on the accuracy of the performance prediction model and the descriptors of its probabilistic parameters. However, in some cases (e.g., scour prediction models) the uncertainty of the available models is very high. In this case, updating the model parameters based on monitoring data can help to calibrate the models and achieve more realistic results for the specific case study.
- The proposed framework for quantifying the risk and fragility of bridges can be used as a starting point for developing bridge management and decision-making approaches. As an example, the proposed risk quantification approach can be extended to develop a framework that would be capable of providing optimal maintenance plans that result in a reduced life-cycle cost.
- The presented damage detection approach was validated for flexural damage in fully prestressed simply supported beams. However, more research is still needed to quantify the effect of loading location, temperature gradients, boundary conditions, and shrinkage and creep strains on the proposed approach. Future efforts are required to implement the

presented damage identification and localization approach for long-term performance monitoring of bridges under field conditions.

- The research presented in Chapter V focused on quantifying the reliability of double shear splice connections. Future research is still needed to quantify the reliability of other connection configurations.

REFERENCES

AASHTO (American Association of State Highway and Transportation Officials). (2010). "Bridge design specifications (LRFD)." *5th Ed*., Washington, DC.

AASHTO (American Association of State Highway and Transportation Officials). (2014). "Bridge design specifications (LRFD)." 6*th Ed*., Washington, DC.

AASHTO (American Association of State Highway and Transportation Officials). (2017). "*Bridge design specifications (LRFD)*." 8th Ed., Washington, DC.

Abadi, M., Barham, P., Chen, J., Chen, Z., Davis, A., Dean, J., ... & Kudlur, M. (2016). "Tensorflow: a system for large-scale machine learning." *In OSDI Vol. 16* (pp. 265-283)

ABAQUS. (2018). *Abaqus/CAE 6.14 user's guide*. Providence, RI: Dassault Systèmes Simulia Corp, France.

Abdel-Jaber, H., & Glisic, B. (2015). Analysis of the status of pre-release cracks in prestressed concrete structures using long-gauge sensors. *Smart Materials and Structures*, *24*(2), 025038.

Abdel-Jaber, H., & Glisic, B. (2019). Monitoring of long-term prestress losses in prestressed concrete structures using fiber optic sensors. *Structural Health Monitoring*, *18*(1), 254-269.

Ahammed, M., & Melchers, R. E. (1997). Probabilistic analysis of underground pipelines subject to combined stresses and corrosion. *Engineering structures*, *19*(12), 988-994.

AISC. (2017). *Steel Construction Manual, 15th Edition*. American Institute of Steel Construction Chicago, IL.

Akiyama, M., Frangopol, D. M., Arai, M., & Koshimura, S. (2012). "Probabilistic assessment of structural performance of bridges under tsunami hazard." *In Structures Congress 2012* (pp. 1919-1928).

Alipour, A., & Shafei, B. (2012). "Performance assessment of highway bridges under earthquake and scour effects." *In Proceedings of the 15th world conference on earthquake engineering*, Lisbon, Portugal. 24-28.

American Petroleum Institute (API) (1987). "*Recommended Practice for Planning, Designing and Constructing Fixed Offshore Platforms*." API Recommended Practice 2A(RP-2A), Washington D.C, 17th edition.

Anastasopoulos, D., De Smedt, M., Vandewalle, L., De Roeck, G., & Reynders, E. P. (2018). Damage identification using modal strains identified from operational fiber-optic Bragg grating data. *Structural Health Monitoring*, *17*(6), 1441-1459.

Anderson, C. J., Claman, D., & Mantilla, R. (2015). "Iowa's Bridge and Highway Climate Change and Extreme Weather Vulnerability Assessment Pilot." *Federal Highway Administration, HEPN-707.* Ames, IA.

Ang, A. H. S., & Tang, W. H. (2007). *Probability concepts in engineering planning and design: Emphasis on application to civil and environmental engineering.* Wiley & Sons.

Arnell, N. W., & Gosling, S. N. (2016). "The impacts of climate change on river flood risk at the global scale." *Climatic Change*, *134*(3), 387-401.

Arneson, L.A., Zevenbergen, L.W., Lagasse, P.F., & Clopper, P.E. (2012). "Evaluating scour at bridges." *Hydraulic Engineering Circular No. 18: Federal Highway Administration, HIF-12-003*. Washington, DC.

ASTM (1949), *High-Strength Bolts for Structural Steel Joints,* American Society for Testing and Materials, Philadelphia, PA.

Ataei, N., & Padgett, J. E. (2012). "Probabilistic modeling of bridge deck unseating during hurricane events." *Journal of Bridge Engineering*, *18*(4), 275-286.

Balomenos, G. P., & Padgett, J. E. (2018). "Fragility analysis of pile-supported wharves and piers exposed to storm surge and waves." *Journal of Waterway, Port, Coastal, and Ocean Engineering*, *144*(2), 04017046.

Banerjee, S., & Ganesh Prasad, G. (2013). "Seismic risk assessment of reinforced concrete bridges in flood-prone regions." *Structure and Infrastructure Engineering*, *9*(9), 952-968.

Batho, C., & Bateman, E. H. (1934). *Investigations on Bolts and Bolted Joints*, Second Report of the Steel Structures Research Committee, H.M Stationary Office, London.

Bickel, S., Brückner, M., & Scheffer, T. (2009). Discriminative learning under covariate shift. *Journal of Machine Learning Research*, *10*(Sep), 2137-2155.

Bolduc, L., Gardoni, P., & Briaud, J.-L. (2008). "Probability of exceedance estimates for scour depth around bridge piers." *Journal of Geotechnical and Geoenvironmental Engineering*, *134*(2), 175–184.

Bowman, M.D., & Quinn, B.P. (1994). Examination of fillet weld strength. *Engineering Journal, AISC, 31*(3), 98-108.

Brekke, L., Thrasher, B. L., Maurer, E. P., & Pruitt, T. (2013). "Downscaled CMIP3 and CMIP5 climate and hydrology projections: Release of downscaled CMIP5 climate projections, comparison with preceding information, and summary of user needs." *US Department of the Interior, Bureau of Reclamation, Technical Services Center*, Denver, Colorado.

Breusers, H. N. C. (1965), "Scour around drilling platforms." *Bulletin, Hydraulic Research 1964 and 1965, IAHR,* Vol.19.

Briaud, J. L. (2008). "Case histories in soil and rock erosion: Woodrow Wilson bridge, Brazos River Meander, Normandy Cliffs, and New Orleans Levees." *Journal of Geotechnical and Geoenvironmental Engineering*, *134*(10), 1425-1447.

Briaud, J. L., Brandimarte, L., Wang, J., & D'Odorico, P. (2007). "Probability of scour depth exceedance owing to hydrologic uncertainty." *Georisk: Assessment and Management of Risk for Engineered Systems and Geohazards*, *1*(2), 77-88.

Briaud, J. L., Chen, H. C., Kwak, K. W., Han, S. W., & Ting, F. C. K. (2001). "Multiflood and multilayer method for scour rate prediction at bridge piers." *Journal of Geotechnical and Geoenvironmental Engineering, 127*(2), 114-125.

Briaud, J. L., Gardoni, P., & Yao, C. (2013). "Statistical, risk, and reliability analyses of bridge scour." *Journal of Geotechnical and Geoenvironmental Engineering*, *140*(2), 04013011.

Briaud, J. L., Ting, F. C. K., Chen, H. C., Gudavalli, R., Kwak, k., Philogene, B., Han, S. W., Perugu, S., Wei, G., Nurtjahyo, P., Cao, Y, & Li, Y. (1999b). "SRICOS: Prediction of scour rate at bridge piers." *Res. Rep. Prepared for Texas Dept. of Transp,* Austin, Tx.

Briaud, J. L., Ting, F. C., Chen, H. C., Gudavalli, R., Perugu, S., & Wei, G. (1999a). "SRICOS: Prediction of scour rate in cohesive soils at bridge piers." *Journal of Geotechnical and Geoenvironmental Engineering*, *125*(4), 237-246.

Broding, W. C., Diederich, F. W., & Parker, P. S. (1964). "Structural optimization and design based on a reliability design criterion." *Journal of Spacecraft and Rockets, 1*(1), 56-61.

Brown, D. A., & Reese, L. C. (1988). "Behavior of a large-scale pile group subjected to cyclic lateral loading." *TEXAS UNIV AT AUSTIN GEOTECHNICAL ENGINEERING CENTER.*

Buratti, N., Ferracuti, B., & Savoia, M. (2010). "Response surface with random factors for seismic fragility of reinforced concrete frames." *Structural Safety, 32*(1), 42-51.

Butler, L. J., Gibbons, N., He, P., Middleton, C., & Elshafie, M. Z. (2016). Evaluating the early-age behaviour of full-scale prestressed concrete beams using distributed and discrete fibre optic sensors. *Construction and Building Materials*, *126*, 894-912.

Callele, L. J., Grondin, G. Y., & Driver, R. G. (2005). *Strength and behaviour of multi-orientation fillet weld connections*. University of Alberta, Department of Civil and Environmental Engineering.

Camp, J., Abkowitz, M., Hornberger, G., Benneyworth, L., & Banks, J. C. (2013). "Climate change and freight-transportation infrastructure: Current challenges for adaptation." *Journal of Infrastructure Systems*, *19*(4), 363-370

Carcano, E. C., Bartolini, P., Muselli, M., & Piroddi, L. (2008). "Jordan recurrent neural network versus IHACRES in modelling daily streamflows." *Journal of hydrology*, *362*(3), 291-307.

Chan, C. L., & Low, B. K. (2012). "Probabilistic analysis of laterally loaded piles using response surface and neural network approaches." *Computers and Geotechnics*, *43*, 101-110.

Chevreuil, M., Lebrun, R., Nouy, A., & Rai, P. (2015). A least-squares method for sparse low rank approximation of multivariate functions. *SIAM/ASA Journal on Uncertainty Quantification*, *3*(1), 897-921.

Chung, W., & Kang, D. (2008). Full-scale test of a concrete box girder using FBG sensing system. *Engineering Structures*, *30*(3), 643-652.

Coiffier, J. (2011). *Fundamentals of numerical weather prediction*. Cambridge University Press, New York.

Cook, W., Barr, P.J., & Halling, M.W. (2015). "Bridge failure rate." *Journal of Performance of Constructed Facilities*, *29*(3), 04014080.

Croke, B. F. W., & Jakeman, A. J. (2008). "Use of the IHACRES rainfall-runoff model in arid and semi arid regions." *Hydrological modelling in arid and semi-arid areas*, 41-48.

Croke, B. F. W., Andrews, F., Spate, J., & Cuddy, S. M. (2005). "IHACRES user guide. Technical Report 2005/19." *Second Edition. iCAM, School of Resources, Environment and Society, The Australian National University*, Canberra, Australia.

Cuomo, G., Shams, G., Jonkman, S., & Van Gelder, P. (2008). "Hydrodynamic loadings of buildings in floods." *Coastal Engineering*, 3745.

Danner, C., & Fuller, J., (2015). "Texas and Oklahoma begin cleaning up after devastating floods." <http://nymag.com/daily/intelligencer/2015/05/floods-devastate-texas-and-oklahoma.html> (Dec. 15, 2017)

David, C. H., Famiglietti, J. S., Yang, Z. L., Habets, F., & Maidment, D. R. (2016). "A decade of RAPID—Reflections on the development of an open source geoscience code." *Earth and Space Science*, *3*(5), 226-244.

Decker, J. B., Rollins, K. M., & Ellsworth, J. C. (2008). "Corrosion rate evaluation and prediction for piles based on long-term field performance." *Journal of geotechnical and geoenvironmental engineering*, *134*(3), 341-351.

Decò, A., & Frangopol, D. M. (2011). "Risk assessment of highway bridges under multiple hazards." *Journal of Risk Research*, *14*(9), 1057-1089.

Deng, K., Grondin, G. Y., & Driver, R. G. (2003). *Effect of loading angle on the behavior of fillet welds*. Department of Civil and Environmental Engineering, University of Alberta.

Dieter, G. (2000). "*Engineering design: A materials and processing approach (3rd ed., McGraw-Hill series in mechanical engineering).*" Boston: McGraw-Hill.

Dikanski, H., Imam, B., & Hagen-Zanker, A. (2018). "Effects of uncertain asset stock data on the assessment of climate change risks: A case study of bridge scour in the UK." *Structural Safety*, *71*, 1-12.

Ding, L., (2019). "Corrosion Behavior of H-Pile Steel in Different Soils" *All Dissertations*. 2334.
https://tigerprints.clemson.edu/all_dissertations/2334

Dong, Y., & Frangopol, D. M. (2016). "Probabilistic time-dependent multihazard life-cycle assessment and resilience of bridges considering climate change." *Journal of Performance of Constructed Facilities*, *30*(5), 04016034.

Douglas, E., Jacobs, J., Hayhoe, K., Silka, L., Daniel, J., Collins, M., ... & Mallick, R. (2017). "Progress and Challenges in Incorporating Climate Change Information into Transportation Research and Design." *Journal of Infrastructure Systems*, *23*(4), 04017018.

Dunnavant, T. W., & O'Neill, M. W. (1986). "Evaluation of design-oriented methods for analysis of vertical pile groups subjected to lateral load." In *Proc. of Int. Conf. On Num. Meths. in Offshore0 Pilling, Nantes. France* (pp. 303-316).

Dunphy, J. R., Meltz, G., Lamm, F. P., & Morey, W. W. (1990). Multifunction, distributed optical fiber sensor for composite cure and response monitoring. In *Fiber optic smart structures and skins III* (Vol. 1370, pp. 116-118). International Society for Optics and Photonics.

Echard, B., Gayton, N., & Lemaire, M. (2011). AK-MCS: an active learning reliability method combining Kriging and Monte Carlo simulation. *Structural Safety*, *33*(2), 145-154.

ElGawady, M. A., Abdulazeez, M. M., Ramadan, A., Sherstha, B., Gheni, A., Gomaa, E., Darwish, Y., & ElGawady, M. (2019). "*Behavior and Repair of Corroded Steel H-Piles Phase I (Axial Behavior)"* (No. 25-1121-0005-133-1). Mid-America Transportation Center.

EN 1993-1-1. 2005. "*Eurocode 3: Design of steel structures - Part 1-1": General rules and rules for buildings*.

Ettouney, M. M., & Alampalli, S. (2011). "Infrastructure Health in Civil Engineering: Applications and Management." *CRC Press, Taylor and Francis Boca Raton,* Florida.

Ezeldin, A. S., & Sharara, L. M. (2006). Neural networks for estimating the productivity of concreting activities. *Journal of construction engineering and management*, *132*(6), 650-656.

FAZ Technology (2019).<http://www.faztechnology.com> (Accessed June July 10, 2019).

Fechter, J. (2015). "TXDoT: Two bridges completely wrecked in Central Texas floods, others damaged." <http://www.mysanantonio.com/news/local/article/TXDoT-Two-bridges-wrecked-in-the-Central-Texas-6294892.php#photo-8045574> (Dec. 15, 2017)

Federal Emergency Management Agency (FEMA) (2011). "*Coastal construction manual: Principles and Practices of Planning, Siting, Designing, Constructing, and Maintaining Residential Buildings in Coastal Areas* (4th *edition*)*"* FEMA P55, Washington, D.C.

Fellenius B.H. (1991). "Pile Foundations. In: Fang BY. (eds) Foundation Engineering Handbook." Springer, Boston, MA.

Ferrario, E., Pedroni, N., Zio, E., & Lopez-Caballero, F. (2017). "Bootstrapped Artificial Neural Networks for the seismic analysis of structural systems." *Structural Safety*, *67*, 70-84.

FHWA (Federal Highway Administration). (2016). "National bridge inventory (NBI) dataset." Retrieved from: https://www.fhwa.dot.gov/bridge/nbi/ascii2016.cfm

Fisher, J. W., & Struik J. H. A., (1974). *Guide to Design Criteria for Bolted and Riveted Connections*, Wiley, New York.

Fisher, J.W., Ravindra, M.K., Kulak, G.L., & Galambos, T.V. (1978). Load and Resistance Factor Design Criteria for Connectors. *Journal of the Structural Division*, *104*(9), 1427-1441.

Frost, A. J., Charles, S. P., Timbal, B., Chiew, F. H., Mehrotra, R., Nguyen, K. C., ... & Fernandez, E. (2011). "A comparison of multi-site daily rainfall downscaling techniques under Australian conditions." *Journal of Hydrology*, *408*(1-2), 1-18.

Galambos, T. V. (2004). "Reliability of the member stability criteria in the 2005 AISC Specification." *International Journal of Steel Structures*, *4*(4), 223-230.

Ganesh Prasad, G., & Banerjee, S. (2013). "The impact of flood-induced scour on seismic fragility characteristics of bridges." *Journal of Earthquake Engineering*, *17*(6), 803-828.

Gaspar, B., Garbatov, Y., & Guedes Soares, C. (2009). Effect of uncertain weld shape on the structural hot-spot stress distribution. *Analysis and Design of Marine Structures. Taylor & Francis Group, London, UK*, 267-278.

Gehl, P., & D'Ayala, D. (2016). "Development of Bayesian networks for the multi-hazard fragility assessment of bridge systems." *Structural Safety*, *60*, 37-46.

Geokon (2019). < https://www.geokon.com/> (Accessed June July 10, 2019).

Gidaris, I., Padgett, J. E., Barbosa, A. R., Chen, S., Cox, D., Webb, B., & Cerato, A. (2017). "Multiple-hazard fragility and restoration models of highway bridges for regional risk and resilience assessment in the United States: state-of-the-art review." *Journal of structural engineering*, *143*(3), 04016188.

Godfrey, H.J., & Mount, E.H. (1940). Pilot Tests on Covered Electrode Welds, *Welding Journal, Vol. 19* (1940), Reprint No. 48 (40-2).

Gomes, W.dS. J. (2019). Structural Reliability Analysis Using Adaptive Artificial Neural Networks." ASCE-ASME J Risk and Uncert in Engrg Sys Part B Mech Engrg, 5(4).

Govindasamy, A.V., Briaud, J., Chen, H., Delphia, J., Elsbury, K., Gardoni, P., Herrman, G., Kim, D., Mathewson, C., McClelland, M., & Olivera, F. (2008). "Simplified method for estimating scour at bridges," *GeoCongress 2008, Geosustainability and Geohazard* Mitigation, 178, 385-393.

Gres, S., Ulriksen, M. D., Döhler, M., Johansen, R. J., Andersen, P., Damkilde, L., & Nielsen, S. A. (2017). "Statistical methods for damage detection applied to civil structures." *Procedia engineering*, *199*, 1919-1924.

Grondin, G. Y., Jin, M., & Georg, J. (2007). . Structural Engineering Report No. 270. University of Alberta, Department of Civil & Environmental Engineering, Edmonton, Alberta, CA.

Ha, S., Kim, K., Kim, K., Jeong, H., & Kim, H. (2017). "Reliability Approach in Economic Assessment of Adapting Infrastructure to Climate Change." *Journal of Management in Engineering*, *33*(5), 04017022.

Hagan, M. T., & Menhaj, M. B. (1994). Training feedforward networks with the Marquardt algorithm. *IEEE transactions on Neural Networks*, *5*(6), 989-993.

Haldar, S., & Basu, D. (2014). "Resistance factors for laterally loaded piles in clay." In *Geo-Congress 2014: Geo-characterization and Modeling for Sustainability* (pp. 3333-3342).

Halton, J. H. (1964). Algorithm 247: Radical-inverse quasi-random point sequence. *Communications of the ACM*, *7*(12), 701-702.

Hannigan, P. J., Rausche, F., Likins, G. E., Robinson, B. R., & Becker, M. L. (2016). "*Geotechnical Engineering Circular No. 12–Volume II Design and Construction of Driven Pile Foundations."* (No. FHWA-NHI-16-010).

Hawkins, E., & Sutton, R. (2009). "The potential to narrow uncertainty in regional climate predictions." *Bulletin of the American Meteorological Society*, *90*(8), 1095-1107.

Hazus (2018). "Hazus Flood Model User Guidance". Federal Emergency Management Agency, Washington, DC.

Heistermann, C. (2011). *Behaviour of pretensioned bolts in friction connections: towards the use of higher strength steels in wind towers* (Doctoral dissertation, Luleå tekniska universitet).

Hess, P. E., Bruchman, D., Assakkaf, I. A., & Ayyub, B. M. (2002). Uncertainties in material and geometric strength and load variables. *Naval Engineers Journal*, *114*(2), 139-166.

Hidalgo, H. G., & Alfaro, E. J. (2015). "Skill of CMIP5 climate models in reproducing 20th century basic climate features in Central America." *International Journal of Climatology*, *35*(12), 3397-3421.

Higgins, T.R & Preece, F.R., (1969). Proposed Working Stresses for Fillet Welds in Building Construction. *Engineering Journal, AISC, 6*(1).

Holtz, N.M. & Kulak, G.L., (1970). *High-strength bolts and welds in load-sharing systems*, Structural Engineering Report No. 8. Department of Civil Engineering, Nova Scotia Technical College, Halifax, Nova Scotia.

Hosmer Jr, D. W., Lemeshow, S., & Sturdivant, R. X. (2013). "*Applied logistic regression* (Vol. 398)." John Wiley & Sons, New York.

Humphrey, G. B., Gibbs, M. S., Dandy, G. C., & Maier, H. R. (2016). "A hybrid approach to monthly streamflow forecasting: integrating hydrological model outputs into a Bayesian artificial neural network." *Journal of Hydrology*, *540*, 623-640.

Hung, C.-C., & Yau, W.-G. (2014). "Behavior of scoured bridge piers subjected to flood-induced loads." *Engineering Structures*, *80*, 241-250.

Idriss, R. L., Kodindouma, M. B., Kersey, A. D., & Davis, M. A. (1998). Multiplexed Bragg grating optical fiber sensors for damage evaluation in highway bridges. *Smart Materials and Structures*, *7*(2), 209.

Inaudi, D., & Vurpillot, S. (1999). Monitoring of concrete bridges with long-gage fiber optic sensors. *Journal of intelligent material systems and structures*, *10*(4), 280-292.

Jarosch, K.H. & Bowman, M.D. (1986). Tension butt joints with bolts and welds. *Engineering Journal, AISC, 23*(1), 25-35.

JCSS. (2001). *"Probabilistic model code."* Joint Committee on Structural Safety.

Jia, Y., Shelhamer, E., Donahue, J., Karayev, S., Long, J., Girshick, R., ... & Darrell, T. (2014). "Caffe: Convolutional architecture for fast feature embedding." *In Proceedings of the 22nd ACM international conference on Multimedia* (pp. 675-678). ACM.

Jin, S. S., & Jung, H. J. (2018). Vibration-based damage detection using online learning algorithm for output-only structural health monitoring. *Structural Health Monitoring*, *17*(4), 727-746.

Johnson, P. A., Clopper, P. E., Zevenbergen, L. W., & Lagasse, P. F. (2015). "Quantifying uncertainty and reliability in bridge scour estimations." *Journal of Hydraulic Engineering*, *141*(7), 04015013.

Kadar, I., Nagy, L., (2017). "The examination of different soil parameters' coefficient of variation values and types of distributions." *Proceedings of the 6th International Young Geotechnical Engineers' Conference (iYGEC6).*

Kallias, A. N., & Imam, B. (2016). "Probabilistic assessment of local scour in bridge piers under changing environmental conditions." *Structure and Infrastructure Engineering*, *12*(9), 1228-1241.

Kang, L. H., Kim, D. K., & Han, J. H. (2007). Estimation of dynamic structural displacements using fiber Bragg grating strain sensors. *Journal of sound and vibration*, *305*(3), 534-542.

Karpathy, A., & Fei-Fei, L. (2015). "Deep visual-semantic alignments for generating image descriptions." *In Proceedings of the IEEE conference on computer vision and pattern recognition* (pp. 3128-3137).

Khandel, O. & Soliman, M., (2021). An Integrated Framework for Assessment of Time-Variant Flood Fragility Using Deep Learning Neural Networks. *Journal of infrastructure systems, ASCE*. *27*(1): 04020045. https://doi.org/10.1061/(ASCE)IS.1943-555X.0000587.

Khandel, O., & Soliman, M. (2018). Maintenance Optimization for Deteriorating Bridges under Uncertainty. In *Structures Congress 2018: Bridges, Transportation Structures, and Nonbuilding Structures* (pp. 242-251). Reston, VA: American Society of Civil Engineers.

Khandel, O., & Soliman, M. (2019a). Integrated Framework for Quantifying the Effect of Climate Change on the Risk of Bridge Failure Due to Floods and Flood-Induced Scour. *Journal of Bridge Engineering, ASCE. 24*(9), 04019090. https://doi.org/10.1061/(ASCE)BE.1943-5592.0001473.

Khandel, O., and Soliman, M. (2019b). A Multi-Hazard Probabilistic Framework for Quantifying Bridge Failure Risk Considering Climate Change. In *MATEC Web of Conferences* (Vol. 271, p. 01006). EDP Sciences.

Khandel, O., Soliman, M., Floyd, R., & Murray, C. D., (2019c). Application of Fiber Optic Sensors for Damage Detection and Performance Monitoring of Prestressed Concrete Bridge Girders. SHMII-9 – *9th International Conference on Structural Health Monitoring of Intelligent Infrastructure*. St. Louis, Missouri, USA, August 4-7, 2019.

Khandel, O., Soliman, M., Floyd, R., & Murray, C. D., (2020). Performance Assessment of Prestressed Concrete Bridge Girders using Fiber Optic Sensors and Artificial Neural Networks, *Structure and Infrastructure Engineering*. https://doi.org/10.1080/15732479.2020.1759658.

Khandel. O. & Soliman, M. (2019d). Deep Learning Based Framework for Long-term Management of Bridges Considering Climate Change Effects. *2019 IABSE Congress,* New York City, NY, USA, September 4-6, 2019.

Khelifa, A., Garrow, L. A., Higgins, M. J., & Meyer, M. D. (2013). "Impacts of climate change on scour-vulnerable bridges: Assessment based on HYRISK." *Journal of Infrastructure Systems*, *19*(2), 138-146.

Kim, H., Sim, S. H., Lee, J., Lee, Y. J., & Kim, J. M. (2017). "Flood fragility analysis for bridges with multiple failure modes." *Advances in Mechanical Engineering*, *9*(3), 1687814017696415.

Kingma, D. P., & Ba, J. (2014). "Adam: A method for stochastic optimization." *arXiv preprint arXiv:1412.6980*.

Konakli, K., & Sudret, B. (2016a). Global sensitivity analysis using low-rank tensor approximations. *Reliability Engineering & System Safety*, *156*, 64-83.

Konakli, K., & Sudret, B. (2016b). Polynomial meta-models with canonical low-rank approximations: Numerical insights and comparison to sparse polynomial chaos expansions. *Journal of Computational Physics*, *321*, 1144-1169.

Konakli, K., Mylonas, C., Marelli, S. and Sudret, B. (2019) *UQLAB user manual – Canonical low-rank approximations*, Report UQLab-V1.2-108, Chair of Risk, Safety & Uncertainty Quantification, ETH Zurich, Zurich, Switzerland.

Kroetz, H. M., Tessari, R. K., & Beck, A. T. (2017). "Performance of global metamodeling techniques in solution of structural reliability problems." *Advances in Engineering Software*, 114, 394-404.

Kucera, V., & Mattsson, E. (1987). "Atmospheric corrosion." *Corrosion mechanisms*, *28*, 211-284.

Kulak, G. L., Fisher, J. W., & Struik, J. H. (2001). *Guide to Design Criteria for Bolted and Riveted Joints Second Edition*, American Institute of Steel Construction Chicago, IL.

Kwan, Y. K., Gomez, I. R., Grondin, G. Y., & Kanvinde, A. M. (2010). Strength of welded joints under combined shear and out-of-plane bending. *Canadian Journal of Civil Engineering*, *37*(2), 250-261.

Laprise, R. (2008). "Regional climate modelling." *Journal of Computational Physics*, *227*(7), 3641-3666.

Lataniotis, C., Marelli, S., & Sudret, B. (2019). UQLab user manual–Kriging (Gaussian process modelling). *Report UQLab-V0*, 9-105.

Levenberg, K. (1944). A method for the solution of certain non-linear problems in least squares. *Quarterly of applied mathematics*, *2*(2), 164-168.

Li, C., Grondin, G. Y., & Driver, R. G. (2007). Reliability analysis of concentrically loaded fillet welds. University of Alberta, Department of Civil and Environmental Engineering.

Li, D. Q., Jiang, S. H., Wu, S. B., Zhou, C. B., & Zhang, L. M. (2013). "Modeling multivariate distributions using Monte Carlo simulation for structural reliability analysis with complex performance function." *Proceedings of the Institution of Mechanical Engineers, Part O: Journal of risk and reliability*, *227*(2), 109-118.

Liang, X., Lettenmaier, D. P., Wood, E. F., & Burges, S. J. (1994). "A simple hydrologically based model of land surface water and energy fluxes for general circulation models." *Journal of Geophysical Research: Atmospheres*, *99*(D7), 14415-14428.

Liaw, A., & Wiener, M. (2002). "Classification and regression by randomForest." *R news*, *2*(3), 18-22.

Lin, Y. B., Chang, K. C., Chern, J. C., & Wang, L. A. (2004). The health monitoring of a prestressed concrete beam by using fiber Bragg grating sensors. *Smart Materials and Structures*, *13*(4), 712.

Maaskant, R., Alavie, T., Measures, R. M., Tadros, G., Rizkalla, S. H., & Guha-Thakurta, A. (1997). Fiber-optic Bragg grating sensors for bridge monitoring. *Cement and Concrete Composites*, *19*(1), 21-33.

Maloney, E. D., Camargo, S. J., Chang, E., Colle, B., Fu, R., Geil, K. L., Hu, Q., Jiang, X., Johnson, N. & Karnauskas, K. B. (2014). "North American climate in cmip5 experiments: part iii: assessment of twenty-first-century projections." *Journal of Climate*, *27*(6), 2230-2270.

Mann, N. R., Singpurwalla, N. D., & Schafer, R. E. (1974). "*Methods for statistical analysis of reliability and life data*." John Wiley, New York.

Manuel, T.J., & Kulak, G.L. (2000). Strength of joints that combine bolts and welds. *Journal of Structural Engineering*, *126*(3), 279-287.

Marelli, S., & Sudret, B. (2014) UQLab: A framework for uncertainty quantification in Matlab, Proc. 2nd Int. Conf. on Vulnerability, *Risk Analysis and Management* (ICVRAM2014), Liverpool, United Kingdom, 2554-2563.

Marelli, S., Lamas, C., Konakli, K., Mylonas, C., Wiederkehr, P., & Sudret, B. (2019a) *UQLAB user manual – Sensitivity analysis*, Report UQLab-V1.2-106, Chair of Risk, Safety & Uncertainty Quantification, ETH Zurich, Zurich, Switzerland.

Marelli, S., Schöbi, R., & Sudret, B. (2019b) UQLAB user manual – Structural reliability (Rare event estimation), Report UQLab-V1.2-107, Chair of Risk, Safety & Uncertainty Quantification, ETH Zurich, Zurich, Switzerland.

Marquardt, D. W. (1963). An algorithm for least-squares estimation of nonlinear parameters. *Journal of the society for Industrial and Applied Mathematics*, *11*(2), 431-441.

MathWorks (2019). MATLAB: The Language of technical computing. (Accessed June 15, 2019). https://www.mathworks.com/help/matlab

MathWorks, M. A. T. L. A. B. (2016). "*SIMULINK for technical computing.*" Available on http://www. mathworks. com.

Mattson, S. G., & Pandit, S. M. (2006). Statistical moments of autoregressive model residuals for damage localisation. *Mechanical Systems and Signal Processing*, *20*(3), 627-645.

Maurer, E. P., & Hidalgo, H. G. (2008). "Utility of daily vs. monthly large-scale climate data: an intercomparison of two statistical downscaling methods." *Hydrology and Earth System Science*, *12*, 551-563.

Maurer, E. P., Hidalgo, H. G., Das, T., Dettinger, M. D., & Cayan, D. R. (2010). "The utility of daily large-scale climate data in the assessment of climate change impacts

on daily streamflow in California." *Hydrology and Earth System Science, 14*, 1125-1138.

Mazzoni, S., McKenna, F., Scott, M. H., & Fenves, G. L. (2006). "*OpenSees command language manual*." Pacific Earthquake Engineering Research (PEER) Center, 264.

McKay, M. D., Beckman, R. J., & Conover, W. J. (1979). Comparison of three methods for selecting values of input variables in the analysis of output from a computer code. *Technometrics, 21*(2), 239-245.

McPherson, R., (2016). "Impacts of Climate change on Flows in the Red River Basin," *SCCSC, South Centeral Climate Science Center,* Norman, OK .

Mehta, A. (2019). A Complete Guide to Types of Neural Networks. https://www.digitalvidya.com/blog/types-of-neural-networks/ . (Accessed June July 25, 2019)

Melchers, R. E., & Beck, A. T. (2018). "*Structural reliability analysis and prediction*. 3rd edition", John Wiley & Sons.

Mondoro, A., Frangopol, D. M., & Liu, L. (2018). "Multi-criteria robust optimization framework for bridge adaptation under climate change." *Structural Safety, 74*, 14-23.

Montana, D. J., & Davis, L. (1989, August). Training Feedforward Neural Networks Using Genetic Algorithms. In *IJCAI* (Vol. 89, pp. 762-767).

Morey, W. W., Meltz, G., & Glenn, W. H. (1990). Fiber optic Bragg grating sensors. In *Fiber Optic and Laser Sensors VII* (Vol. 1169, pp. 98-107). International Society for Optics and Photonics.

Mosher, R.L. (1984). "*Load transfer criteria for numerical analysis of axial loaded piles in sand*." U.S. Army Engineering and Waterways Experimental Station, Automatic Data Processing Center, Vicksburg, Miss.

Moss, R. H., Edmonds, J. A., Hibbard, K. A., Manning, M. R., Rose, S. K., Van Vuuren, D. P., ... & Meehl, G. A. (2010). "The next generation of scenarios for climate change research and assessment." *Nature*, *463*(7282), 747.

MTS (2019). <https://www.mts.com> (Accessed June July 10, 2019).

Muis, S., Güneralp, B., Jongman, B., Aerts, J. C., & Ward, P. J. (2015). "Flood risk and adaptation strategies under climate change and urban expansion: A probabilistic analysis using global data." *Science of the Total Environment, 538*, 445-457.

Neumann, J. E., Price, J., Chinowsky, P., Wright, L., Ludwig, L., Streeter, R., ... & Martinich, J. (2015). "Climate change risks to US infrastructure: impacts on roads,

bridges, coastal development, and urban drainage." *Climatic Change*, *131*(1), 97-109.

Ng, K. F., Driver, R. G., Grondin, & G. Y., & (2002). *Behaviour of transverse fillet welds*. University of Alberta, Department of Civil and Environmental Engineering.

NOAA (National Oceanic and Atmospheric Administration) (2015). "Nuisance flooding, an increasing problem as coastal sea levels rise" <http://www.noaanews.noaa.gov/stories2014/20140728_nuisanceflooding.html> (Nov. 10, 2017)

NOAA (National Oceanic and Atmospheric Administration) (2017). <http://www.noaa.gov/> (Nov. 10, 2017)

NOAA (National Oceanic and Atmospheric Administration) (2018). <http://www.noaa.gov/> (Nov. 10, 2018)

Ohsaki, Y. (1982). "Corrosion of steel piles driven in soil deposits." *Soils and foundations*, *22*(3), 57-76.

O'Neill, M. W. (1983). "Group action in offshore piles." *In Geotechnical practice in offshore engineering* (pp. 25-64). American Society of Civil Engineers.

Park, J., & Towashiraporn, P. (2014). "Rapid seismic damage assessment of railway bridges using the response-surface statistical model." *Structural Safety*, *47*, 1-12.

Pathiraja, S., Marshall, L., Sharma, A., & Moradkhani, H. (2016). "Hydrologic modeling in dynamic catchments: A data assimilation approach." *Water Resources Research*, *52*(5), 3350-3372.

Prasad, Y. V., & Chari, T. R. (1999). "Lateral capacity of model rigid piles in cohesionless soils." *Soils and Foundations*, *39*(2), 21-29.

Prohaska, J. D., Snitzer, E., Chen, B., Maher, M. H., Nawy, E. G., & Morey, W. W. (1993). Fiber optic Bragg grating strain sensor in large-scale concrete structures. In *Fiber Optic Smart Structures and Skins V* (Vol. 1798, pp. 286-294). International Society for Optics and Photonics.

Quinn, B.P. (1991). *The effect of profile and root geometry on the strength of fillet welds*, M.Sc. Thesis. Department of Civil Engineering, Purdue University, West Lafayette, IN.

Rampasek, L., & Goldenberg, A. (2016). "Tensorflow: Biology's gateway to deep learning?" *Cell systems*, *2*(1), 12-14.

Ravindra, M. K., & Galambos, T. V. (1978). Load and resistance factor design for steel. *Journal of the Structural Division*, *104*(9), 1337-1353.

RCRBSJ (1951). *Specifications for Assembly of Structural Joints Using High-Strength Bolts*, Research Council on Riveted and Bolted Structural Joints, Chicago, IL.

RCSC Committee. (2004). Specification for structural joints using ASTM A325 or A490 Bolts. *AISC Inc., Chicago, Illinois, USA.*

Reese, C. L., Wang, T. S., Arrellaga, A. J., Hendrix, J., Vasquez, L. (2016). "*A group for the analysis of a group of piles subjected to vertical and lateral loading (User's Manual).*" Ensoft, Austin, TX.

Reese, L. C., & Van Impe, W. F. (2010). "Single piles and pile groups under lateral loading." *CRC Press, Taylor & Francis Group*, New York.

Reiff, A. J., Sanayei, M., & Vogel, R. M. (2016). Statistical bridge damage detection using girder distribution factors. *Engineering Structures*, *109*, 139-151.

Samadi, S. Z., Sagareswar, G., & Tajiki, M. (2010). "Comparison of general circulation models: methodology for selecting the best GCM in Kermanshah Synoptic Station, Iran." *International Journal of Global Warming*, *2*(4), 347-365.

Santner, T. J., Williams, B. J., Notz, W., & Williams, B. J. (2003). *The design and analysis of computer experiments* (Vol. 1). New York: Springer.

Santos, J. P., Crémona, C., Orcesi, A. D., & Silveira, P. (2013). Multivariate statistical analysis for early damage detection. *Engineering Structures*, *56*, 273-285

Schlosser, F., and Bastick, M. (1991). "Reinforced Earth." *Foundation engineering handbook*, H.-Y. Fang, ed., Van Nostrand Reinhold, New York, 778–786.

Schöbi, R., & Sudret, B. (2014). PC-Kriging: a new metamodelling method combining Polynomial Chaos Expansions and Kriging. In *Proc. 2nd Int. Symposium on Uncertainty Quantification and Stochastic Modeling, Rouen, France*.

Schöbi, R., Sudret, B., & Marelli, S. (2016). Rare event estimation using polynomial-chaos kriging. *ASCE-ASME Journal of Risk and Uncertainty in Engineering Systems, Part A: Civil Engineering*, *3*(2), D4016002.

Schweikert, A., Chinowsky, P., Kwiatkowski, K., Johnson, A., Shilling, E., Strzepek, K., & Strzepek, N. (2014). "Road infrastructure and climate change: Impacts and adaptations for South Africa." *Journal of Infrastructure Systems*, *21*(3), 04014046.

Sheffield, J., Barrett, A. P., Colle, B., Nelun Fernando, D., Fu, R., Geil, K. L., Hu, Q., Kinter, J., Kumar, S. & Langenbrunner, B. (2013a). "North American climate in CMIP5 experiments. Part I: evaluation of historical simulations of continental and regional climatology." *Journal of Climate*, *26*(23), 9209-9245.

Sheffield, J., Camargo, S. J., Fu, R., Hu, Q., Jiang, X., Johnson, N., Karnauskas, K. B., Kim, S. T., Kinter, J. & Kumar, S. (2013b). "North American climate in CMIP5

experiments. Part II: evaluation of historical simulations of intraseasonal to decadal variability." *Journal of Climate, 26*(23), 9247-9290.

Shen, C. (2018). "A transdisciplinary review of deep learning research and its relevance for water resources scientists." *Water Resources Research, 54*(11), 8558-8593.

Shi, Y., Wang, L., Wang, Y., Ma, J., & Bai, R., (2011a). Proposed design method of combined connections with bolts and longitudinal welds. *Applied Mechanics and Materials*, 94-96, 923-928.

Shi, Y., Wang, L., Wang, Y., Ma, J., & Bai, R., (2011b). Finite element analysis of the combined connection with bolts and welds. *Applied Mechanics and Materials*, 94-96, 316-321.

Shooman, M. L. (1968). "*Probabilistic reliability: an engineering approach*," McGraw-Hill, New York.

Shrestha, B., Cochrane, T. A., Caruso, B. S., Arias, M. E., & Piman, T. (2016a). "Uncertainty in flow and sediment projections due to future climate scenarios for the 3S Rivers in the Mekong Basin." *Journal of Hydrology, 540*, 1088-1104.

Shrestha, S., Bach, T. V., & Pandey, V. P. (2016b). "Climate change impacts on groundwater resources in Mekong Delta under representative concentration pathways (RCPs) scenarios." *Environmental Science & Policy, 61*, 1-13.

Singh, T., Pal, M., & Arora, V. K. (2019). "Modeling oblique load carrying capacity of batter pile groups using neural network, random forest regression and M5 model tree." *Frontiers of Structural and Civil Engineering, 13*(3), 674-685.

Smith, A., Lott, N., Houston, T., Shein, K., Crouch, J., & Enloe, J. (2017). "US billion-dollar weather & climate disasters: 1980-2017." *NOAA National Centers for Environmental Information.* https://www.ncdc.noaa.gov/billions/events.pdf.

Sobol', I. M. (2001). Global sensitivity indices for nonlinear mathematical models and their Monte Carlo estimates. *Mathematics and computers in simulation, 55*(1-3), 271-280.

Sobol'', I. M. and Levitan, Y. L. (1999). A pseudorandom number generator for personal computers. *Computers & Mathematics with Applications, 37*(4-5):33–40.

Solomon, S. (Ed.). (2007). "Climate change 2007-the physical science basis: Working group I contribution to the fourth assessment report of the IPCC (Vol. 4)." *Cambridge University Press*, New York.

Song, L. K., Bai, G. C., Fei, C. W., & Wen, J. (2018). "Reliability-based fatigue life prediction for complex structure with time-varying surrogate modeling." *Advances in Materials Science and Engineering, 2018*.

Stein, S. M., Young, G. K., Trent, R. E., & Pearson, D. R. (1999). "Prioritizing scour vulnerable bridges using risk." *Journal of Infrastructure Systems*, *5*(3), 95-101.

Steinhardt, O., Möhler, K., & Valtinat, G. (1969). Versuche zur anwendung vorgespannter schrauben im stahlbau. IV. Teil. *Berichte des deutschen Ausschusses für Stahlbau*, (25).

Stocker, T., Qin, D., Plattner, G., Tignor, M., Allen, S., Boschung, J., Nauels, A., Xia, Y., Bex, B. & Midgley, B. (2013). "IPCC, The physical science basis. Contribution of working group I to the fifth assessment report of the intergovernmental panel on climate change." *Cambridge University Press*, New York.

Sudret, B. (2007). "Uncertainty propagation and sensitivity analysis in mechanical models–contributions to structural reliability and stochastic spectral methods." *Habilitationa diriger des recherches, Université Blaise Pascal*, Clermont-Ferrand, France.

Sudret, B. (2008). Global sensitivity analysis using polynomial chaos expansions. *Reliability engineering & system safety*, *93*(7), 964-979.

Sun, W., Zheng, B., & Qian, W. (2016). "Computer aided lung cancer diagnosis with deep learning algorithms." *In Medical imaging 2016: computer-aided diagnosis* (Vol. 9785, p. 97850Z). International Society for Optics and Photonics.

Taylor, K. E., Stouffer, R. J., & Meehl, G. A. (2012). "An overview of CMIP5 and the experiment design." *Bulletin of the American Meteorological Society*, *93*(4), 485-498.

Tian, Y., Pei, K., Jana, S., & Ray, B. (2018). "Deeptest: Automated testing of deep-neural-network-driven autonomous cars." *In Proceedings of the 40th international conference on software engineering* (pp. 303-314). ACM.

Turner, D. (2016). "*Fragility assessment of bridge superstructures under hydrodynamic forces"* (Masters Thesis, Colorado State University).

USGS (United State Geological Survey) (2017). "National Water Information Service," <https://waterdata.usgs.gov/nwis> (Oct. 10, 2017).

USGS (United State Geological Survey) (2018). United State Geological Survey, "National Water Information Service," <https://waterdata.usgs.gov/nwis> (Oct. 1, 2018).

Uva, G., Porco, F., Fiore, A., & Porco, G. (2014). Structural monitoring using fiber optic sensors of a pre-stressed concrete viaduct during construction phases. *Case Studies in Nondestructive Testing and Evaluation*, *2*, 27-37.

Vijayvergiya, V.N. (1977). "Load-movement characteristics of piles." *Proc., Ports 77 Conf.*, ASCE, New York.

Waeytens, J., Rosić, B., Charbonnel, P. E., Merliot, E., Siegert, D., Chapeleau, X., ... & Cottineau, L. M. (2016). Model updating techniques for damage detection in concrete beam using optical fiber strain measurement device. *Engineering Structures*, *129*, 2-10.

Waite, C. D., (2019). *Understanding the Behavior of Double Shear Axial Lap Steel Connections Made in Combination of Slip- Critical Bolts and Longitudinal Fillet Welds*, Masters Thesis, Oklahoma State University, Stillwater, OK.

Wallner, M., & Haberlandt, U. (2015). "Non-stationary hydrological model parameters: a framework based on SOM-B." *Hydrological Processes, 29*(14), 3145-3161.

Wang, N. *(2010). "Reliability-based condition assessment of existing highway bridges"* (Doctoral dissertation, Georgia Institute of Technology).

Wang, S. S., Zhao, L., Yoon, J. H., Klotzbach, P., & Gillies, R. R. (2018). "Quantitative attribution of climate effects on Hurricane Harvey's extreme rainfall in Texas." *Environmental Research Letters*, *13*(5), 054014.

Wang, Z., Dueñas-Osorio, L., & Padgett, J. E. (2014a). "Influence of scour effects on the seismic response of reinforced concrete bridges." *Engineering structures*, *76*, 202-214.

Wang, Z., Padgett, J.E., & Dueñas-Osorio, L. (2014b). "Risk-consistent calibration of load factors for the design of reinforced concrete bridges under the combined effects of earthquake and scour hazards." *Engineering Structures*, *79*, 86-95.

Wang, Z., Pedroni, N., Zentner, I., & Zio, E. (2018). "Seismic fragility analysis with artificial neural networks: Application to nuclear power plant equipment." *Engineering Structures, 162*, 213-225.

Webb, G. T., Vardanega, P. J., Hoult, N. A., Fidler, P. R. A., Bennett, P. J., & Middleton, C. R. (2017). Analysis of fiber-optic strain-monitoring data from a prestressed concrete bridge. *Journal of Bridge Engineering*, *22*(5), 05017002.

Weigel, A. P., Knutti, R., Liniger, M. A., & Appenzeller, C. (2010). "Risks of model weighting in multimodel climate projections." *Journal of Climate*, *23*(15), 4175-4191.

Weinstein, J. C., Sanayei, M., & Brenner, B. R. (2018). Bridge Damage Identification Using Artificial Neural Networks. *Journal of Bridge Engineering*, *23*(11), 04018084.

Westra, S., Thyer, M., Leonard, M., Kavetski, D., & Lambert, M. (2014). "A strategy for diagnosing and interpreting hydrological model nonstationarity." *Water Resources Research*, *50*(6), 5090-5113.

Wilson, W. M., & Thomas, F. P. (1938). *Fatigue Tests of Riveted Joints*, University of Illinois Engineering Experiment Station. Bulletin 302.

Winsemius, H. C., Aerts, J. C., van Beek, L. P., Bierkens, M. F., Bouwman, A., Jongman, B., ... & Ward, P. J. (2016). "Global drivers of future river flood risk." *Nature Climate Change*, *6*(4), 381.

Xue, Y., Janjic, Z., Dudhia, J., Vasic, R., & De Sales, F. (2014). "A review on regional dynamical downscaling in intraseasonal to seasonal simulation/prediction and major factors that affect downscaling ability." *Atmospheric research*, *147*, 68-85.

Ye, W., Bates, B. C., Viney, N. R., Sivapalan, M., & Jakeman, A. J. (1997). "Performance of conceptual rainfall-runoff models in low-yielding ephemeral catchments." *Water Resources Research*, *33*(1), 153-166.

Yilmaz, T., Banerjee, S., & Johnson, P. A. (2018). "Uncertainty in risk of highway bridges assessed for integrated seismic and flood hazards." *Structure and Infrastructure Engineering*, *14*(9), 1182-1196.Yilmaz, T., Banerjee, S., & Johnson, P.A. (2016). "Performance of two real-life California bridges under regional natural hazards." *Journal of Bridge Engineering*, *21*(3), 04015063.

Yip, S., Ferro, C. A., Stephenson, D. B., & Hawkins, E. (2011). "A simple, coherent framework for partitioning uncertainty in climate predictions." *Journal of Climate*, *24*(17), 4634-4643.

Zagona, E. A., Fulp, T. J., Shane, R., Magee, T., & Goranflo, H. M. (2001). "RiverWare: A generalized tool for complex reservoir system modeling." *JAWRA Journal of the American Water Resources Association*, *37*(4), 913-929.

Zhang, W., Gao, J., Shi, B., Cui, H., & Zhu, H. (2006). Health monitoring of rehabilitated concrete bridges using distributed optical fiber sensing. *Computer-Aided Civil and Infrastructure Engineering*, *21*(6), 411-424.

Zhang, Z., Klein, P., & Friedrich, K. (2002). "Dynamic mechanical properties of PTFE based short carbon fibre reinforced composites: experiment and artificial neural network prediction." *Composites Science and Technology*, *62*(7-8), 1001-1009.

Zhu, B., & Frangopol, D. M. (2016a). "Time-dependent risk assessment of bridges based on cumulative-time failure probability." *Journal of Bridge Engineering*, *21*(12), 06016009.

Zhu, B., & Frangopol, D. M. (2016b). "Time-variant risk assessment of bridges with partially and fully closed lanes due to traffic loading and scour." *Journal of Bridge Engineering*, *21*(6), 04016021.

VITA

Omid Khandel

Candidate for the Degree of

Doctor of Philosophy

Dissertation: APPLICATION OF SURROGATE MODELING METHODS IN SIMULATION-BASED RELIABILITY AND PERFORMANCE ASSESSMENT OF CIVIL STRUCTURES

Major Field: Civil Engineering

Biographical:

Education:

Completed the requirements for the Doctor of Philosophy in Civil Engineering at Oklahoma State University, Stillwater, Oklahoma in December, 2020.

Completed the requirements for the Master of Science in Civil Engineering at The University of Toledo, Toledo, OH in 2016.

Completed the requirements for the Bachelor of Science in Civil Engineering at Razi University, Kermanshah, Iran in 2014.